CHARACTERIZATION AND FLUID FLOW PROPERTIES OF FROZEN ROCK SYSTEMS OF UMIAT OIL FIELD, ALASKA

By

Vasil Godabrelidze

RECOMMENDED:

Advisory Committee Chair

Chair, Department of Petroleum Engineering

APPROVED:

Dean, College of Engineering and Mines

Dean of the Graduate School

Dec 14, 2010

Date

CHARACTERIZATION AND FLUID FLOW PROPERTIES OF FROZEN ROCK SYSTEMS OF UMIAT OIL FIELD, ALASKA

A

THESIS

Presented to the Faculty

of the University of Alaska Fairbanks

in Partial Fulfillment of the Requirements

for the Degree of

MASTER OF SCIENCE

By

Vasil Godabrelidze, M.S.

Fairbanks, Alaska

December 2010

Abstract

The Umiat field, located in northwestern Alaska between the Brooks Range and the Arctic Ocean, potentially contains the largest accumulation of oil in Naval Petroleum Reserve No.4. Most of the oil is found within the permafrost zone. The main oil-producing zones in the Umiat field are marine sandstones in the Grandstand Formation of the Cretaceous Nanushuk group. Although the temperatures are close to freezing, the oil in the Umiat field remains unfrozen due to its very high API gravity. However, this results in a very unique pore space containing frozen water and oil, posing a particular challenge to characterization and measurement of fluid flow properties necessary for production.

The unsteady-state gas-oil relative permeability measurement experiments were conducted in order to obtain critical information about the properties of two-phase fluid flow through the Umiat porous medium. Fluid flow experiments at 22^0C and -10^0C on representative core samples from the Umiat field showed 61% average decline in oil relative permeability as a result of freezing irreducible water. Capillary pressure measurement experiments were also carried out on selected core samples with an intention of characterizing their pore size distribution. Subsequently obtained data indicates fairly wide range of pore size for Umiat cores.

Table of Contents

Page

List of Figures

Page

Page

Page

Page

Page

List of Tables

Page

List of Appendices

Page

Disclaimer

Acknowledgements

I would like to thank my advisory committee Abhijit Dandekar, Chair, Shirish Patil, Joanna Mongrain, Mikhail Kanevskiy and Yuri Shur for reviewing this work and giving me their critical comments for improving its quality. I am extremely grateful to my advisor, Dr. Abhijit Dandekar, for all his useful technical suggestions while I was conducting the experimental research.

I would also like to thank Melody Hughes, office manager of the Petroleum Engineering Department, for helping me to complete all the administrative requirements.

I would like to thank Petroleum Development Laboratory of UAF together with the following individuals for their timely technical support: Paul Brown, Joel Bailey, Paul Stefan and Jack Schmidt.

I am grateful to Dr. Cathy Hanks and all the members of the joint project between Renaissance Alaska, LLC and UAF, with whom I had many interesting discussions.

I would like to thank Kenneth Papp, the director of the Geologic Material Center (GMC) in Eagle River and the US DOE for providing the much-needed core samples and the financial assistance respectively. This thesis is based upon work supported by the DOE under Award Number DE-FC26-08NT0005641. I also thank Grant Shimer for sampling the Umiat cores.

Finally deep thanks to my family and friends for their encouragement over the course of my degree program.

Chapter 1 Introduction

1.1 Previous Research History and Problem Statement

In the early 1900s, field geologists from the United States Geological Survey (USGS) explored the National Petroleum Reserve of Alaska (NPR-A), a roadless area located 200 miles north of the Arctic Circle (Gates and Caraway, 1960-A; Baptist, 1960). The geologists discovered several good shows of oil that prompted the establishment of the Naval Petroleum Reserve No.4 (NPR4) in 1923. The area remained largely untouched until the conclusion of the Second World War.

From 1944 through 1953 the Department of Navy, Office of Naval Petroleum and Oil Shale Reserves organized an exploration program to evaluate the oil resources of NPR4 and surrounding area (Gates and Caraway, 1960-B; Baptist 1959). The largest oil accumulation discovered by this program was in the Umiat field. The field has an area of 37000 square miles and lies close to the eastern boundary of the reserve, 180 miles southeast of point Barrow. The axis of the Umiat anticline trends from east to west. The structure, having the closure of more than 800 feet, is about 10 miles long and 3 miles wide. The geographic location of the Umiat oil field is shown in Figure 1.

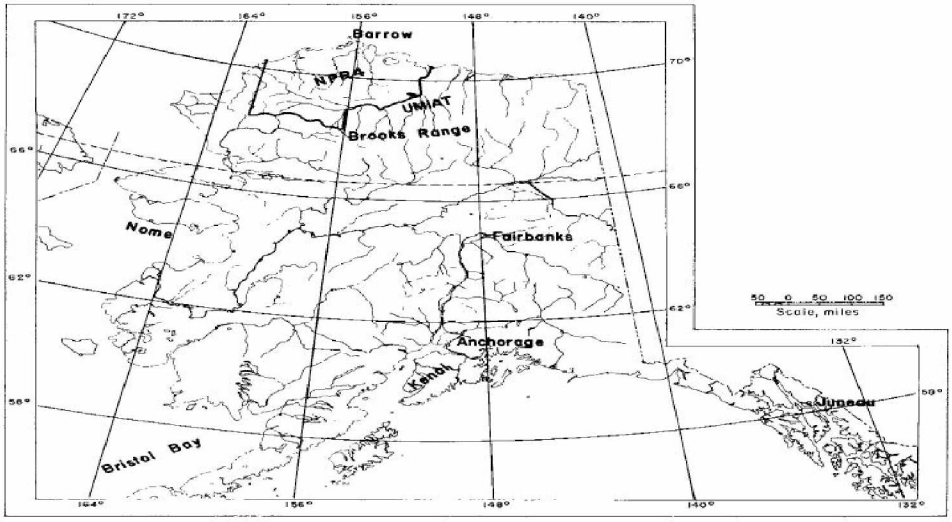

Figure 1: Umiat Field Location (Gates and Caraway, 1960-B)

The initial estimates of recoverable reserves range from 30 to over 100 million bbl (Gaffney, Cline & Associates, 2006; Baptist 1959). The field lies entirely within the continuous permafrost region. The depth to the bottom of the permafrost ranges from 770 to 1055 feet. The oil was found at a depth of 275 to 1100 feet and therefore most of the oil is in the permanently-frozen zone. For this reason, the field is considered unconventional. The oil is 36^0-37^0 API with a 5^0F pour point, which allows it to flow even in a permafrost environment.

The main oil-producing zones in the Umiat field are marine sandstones in the Grandstand Formation of the Cretaceous Nanushuk Group (Baptist, 1960). The upper sandstone is usually 50 to 75 feet thick and is separated from the lower one by 300 feet of gray shale. The thickness of the lower sandstone is much greater but only the top 100 feet has good reservoir quality. The range of reservoir pressures is about 50 psi in the upper sand and about 350 psi in the lower one. Most of the primary production will be based on solution gas drive mechanism.

Out of eleven wells drilled by the U.S. Department of the Navy, six wells produced oil in varying amounts (Gates and Caraway, 1960-A). Location of Umiat wells is shown in Figure 2. It was observed that the wells drilled with either cable tools using brine or rotary tools using oil or oil-based mud produced significantly more oil than those drilled with a rotary rig using water-based mud. For example, well #2 and well #5 are located at about the same elevation on the structure. Yet despite the short distance (200 feet) between these wells, well #2, which was drilled with rotary rig using water-based mud, was abandoned as a dry hole, while well #5, which was drilled with cable tools, pumped 400 BOPD which was the maximum capacity of the pump and could be even less than the capacity of the well. Although the producing gas oil ratio was not determined during these production tests, it was reported that only a small quantity of gas was produced (Baptist, 1960). This gives us solid ground to assume that the reservoir is undersaturated or its pressure is exactly the same as bubble point pressure.

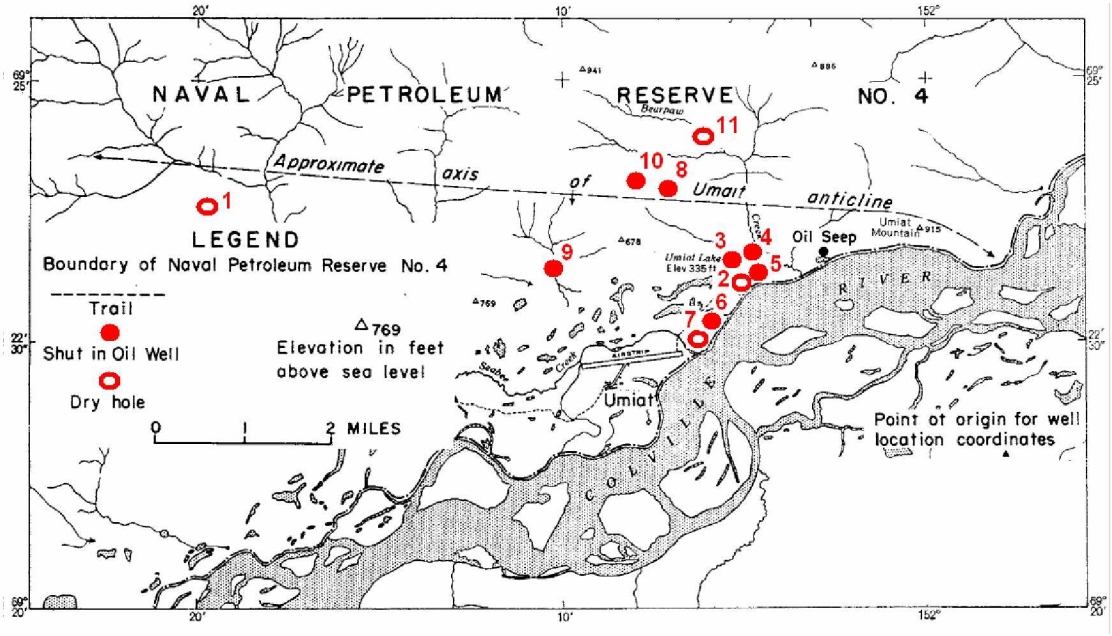

Figure 2: Location of Umiat Wells (Modified from Gates and Caraway, 1960-A)

Because of the extraordinary reservoir conditions and the difficulties encountered in drilling and completing the wells, the Federal Bureau of Mines was asked to carry out laboratory tests of the reservoir sand (Baptist, 1960). The goal of the research was to determine the cause of well plugging and to estimate oil recovery from frozen reservoir rocks under solution gas drive mechanism. For this purpose, experiments were carried out on core samples to determine their clay content and their susceptibility to water damage, and also to find out the effect of freezing of connate water on oil recovery and on relative permeability. The latter test is of most interest for this thesis work and the results obtained by the Federal Bureau of Mines will be discussed in more detail.

Initially it was assumed that the oil-producing sands are extremely water sensitive because of the swelling clays' presence in the sands (Baptist, 1959). Thirty-six sandstone samples were examined by X-ray diffraction methods. No swelling clays were found and the tests confirmed that the reservoir sands have only low to moderate water sensitivity. After analyzing these results, the reason for well plugging was explained in the following

way: circulating water-based mud thawed the wellbore surrounding area and invaded the sand. As a result, water saturation increased in the formation. The water froze soon after the circulation of the warm mud was stopped and it formed a barrier that was impermeable to oil.

In order to determine the depth of permafrost, temperature measurements were made in wells 4, 6, 9 and 11 (Gates and Caraway, 1960-A). Thermistor cables did not reach the base of the permafrost in any of these wells; however, observed uniform temperature gradients from below 100 feet to the bottom of the cable allowed the depth to the base of the permafrost to be estimated. Generally the temperature decreases from the surface to a depth of 70 to 100 feet, and at this depth the minimum temperature is about 20^0F. Below 100 feet the temperature increases according to the geothermal gradient, which was determined to be 1.56^0F/100ft for wells 4 and 6 and 1.33^0F/100ft for well 9. Figure 3 and 4 show the temperature profile of the Umiat wells #6 and #11 respectively.

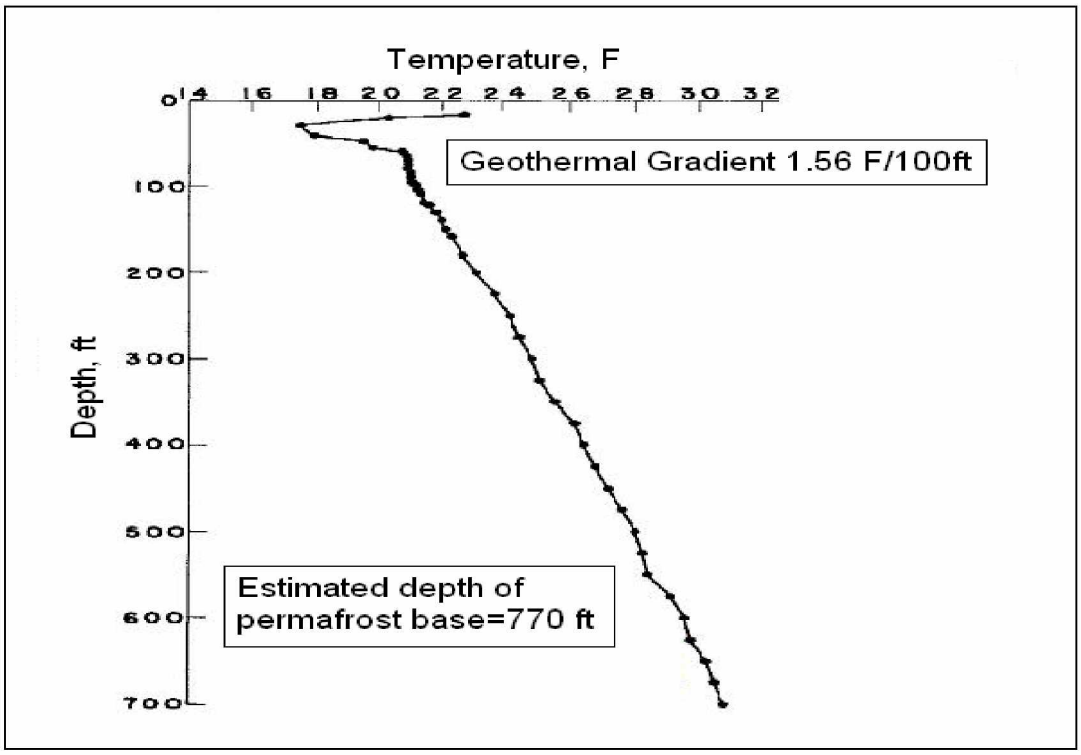

Figure 3: Temperature Profile for Umiat Well 6 (Gates and Caraway, 1960-A)

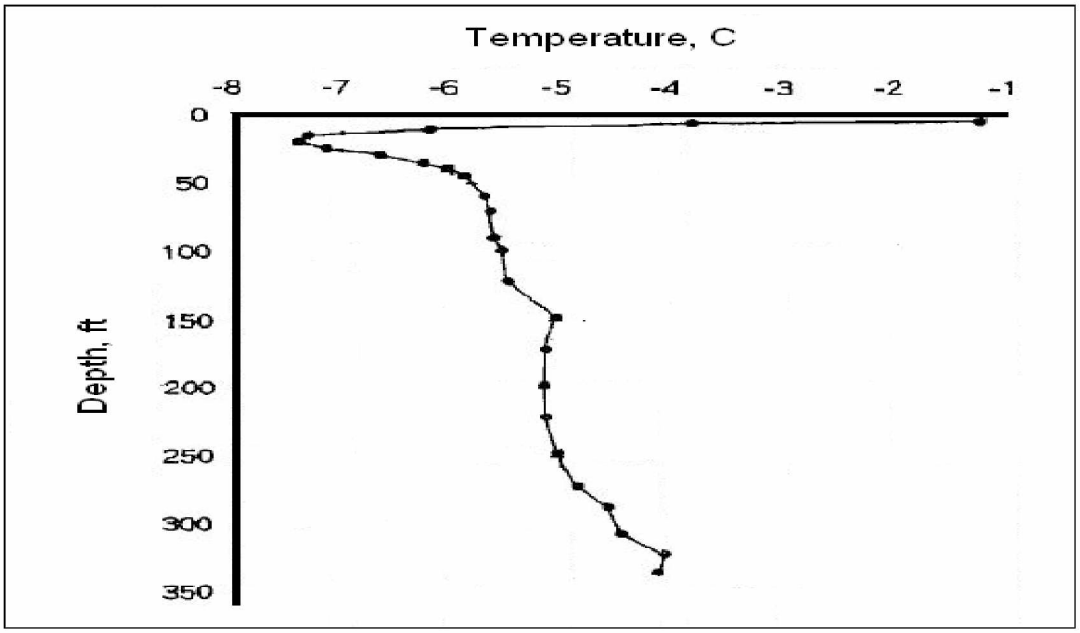

Figure 4: Temperature Profile for Umiat Well 11 on August 1, 1954 (Collins, 1958)

As we see the temperature profile for Umiat well #11 does not indicate the smooth contour characteristic of similar profile for well #6. Presently there is no satisfactory interpretation of this irregularity (Collins, 1958).

The estimated depths to the base of the permafrost in the four wells surveyed are shown in Table 1.

Table 1: Summary of Permafrost Data (Baptist, 1960)

Well number.....	4	6	9	11
Surface elevation.....feet	483	337	424	481
Depth to top of lower sand.....do.	745	1,055	866	2,805
Elevation of top of lower sand, below sea level....do.	262	718	442	2,324
Depth to base of permafrost.....do.	890	770	1,055	770
Elevation of base of permafrost below sea level.....do.	407	433	631	289

To research the reduction of oil permeability and oil recovery due to freezing of interstitial water, a set of experiments was run both at room conditions (75^0F) and simulated permafrost conditions (26^0F) (Baptist, 1960). Experiments were also made on six radial samples to obtain a qualitative index of oil recovery by solution gas expansion and additional oil recovery by gas drive, as well as the effect of freezing on these two recovery processes. The average recovery by solution gas expansion for the four samples tested at 75^0F was 40%, while the same index for the same four samples tested at 26^0F was only about 29%. The average irreducible water saturation for these four samples was about 41%. All these results are summarized in table 2.

Table 2: Oil Recovery Experiments at 75^0F and 26^0F (Baptist, 1960)

Well and sand	Depth, feet	Porosity percent	Air permeability, millidarcys	Initial saturations, percent pore volume		Solution-gas expansion				Gas drive			
						Recovery, initial oil, percent		Residual oil, percent pore volume		Recovery, initial oil, percent		Residual oil, percent pore volume	
				Brine	Oil	26°	75°	26°	75°	26°	75°	26°	75°
Umiat 2, lower	796	16.5	196	37	63	34	48	42	33	21	20	28	20
	797	15.1	49	44	56	27	29	41	39	7	9	36	34
	805	14.6	92	41	59	17	-	49	-	28	-	33	-
Umiat 3, upper	259	18.2	128	42	58	36	-	38	-	34	-	19	-
	352	17.7	134	38	62	31	50	43	34	26	23	27	16
	355	16.3	52	44	56	25	33	42	38	19	34	32	19

To further investigate the effects of freezing of interstitial water, the relative permeability of two samples to oil was tested at room temperature (70^0F) and then below the freezing point of the water (26^0F) (Baptist, 1960). Permeabilities of the samples at 70^0F and 26^0F are 30md and 23md for the first sample (23.3% reduction) and 19md and 13md for the second sample (31.5% reduction). Thus the average reduction in effective oil permeability due to freezing of irreducible water is about 27%.

Although Umiat contains valuable light oil, the field's remote location, far away from the Prudhoe Bay infrastructure and the Trans-Alaska Oil Pipeline, has precluded the

development of the field for many years (Bailey, 2009). In 2004, as oil prices started to climb from $30s into the $40s, Renaissance Alaska, LLC saw Umiat as one of several Alaska opportunities. Based on 2008 3-D seismic survey and new assessment of field reserves, Renaissance thinks that modern production technology, such as horizontal wells, will grow the field's economically recoverable oil reserve up to 250 million bbl. That is much higher than an old USGS assessment which assumed the use of vertical wells only.

Considering the decline in the production of conventional oil resources from Alaska North Slope, the development of unconventional oil fields such as Umiat becomes attractive. Development of the Umiat oil field could prove to be a useful addition to the inventory of producing fields in northern Alaska. For this purpose it is necessary to build a good reservoir model in order to test different production methods and predict the field's future performance using various reservoir simulators. This objective dictated the problem that had to be addressed in this experimental research. Particularly, the problem implies obtaining critical information about the rock and fluid properties of the reservoir by means of conducting the core flooding experiments and studying two-phase fluid flow properties both at room temperature and in simulated permafrost conditions.

In order to get economically viable oil flow rates while producing hydrocarbons from Umiat field, it will be necessary to artificially support the reservoir energy because the natural energy of the reservoir is fairly low due to low reservoir pressures. For this purpose, injection of cold gas is being considered as one of the EOR techniques (Joshi Technologies International Inc., 2008). Moreover, as Baptist (1960) stated in his work, primary recovery will be based on solution-gas drive mechanism. All of this implies two phase, gas-oil flow through the Umiat porous media and hence obtained relative permeability data becomes imperative as a means to predict reservoir behavior.

1.2 **Objectives**

To promote economically viable resource extraction from the Umiat field, it is necessary to build an adequate reservoir model and test the possible production methods. In order to perform this task, we need to get critical information about the rock and fluid properties of the reservoir. These goals defined the objectives of the thesis work as follows:

- Review the existing Umiat rock and fluid data obtained by USGS during the initial drilling program.
- Collect the existing conventional core samples and prepare the core plugs.
- Develop the experimental procedures.
- Design and build experimental setup.
- Conduct the core flooding experiments and study two-phase fluid flow properties through lab-scale tests, both at room temperature and in simulated permafrost conditions.
- Conduct the capillary pressure measurement experiments on selected core samples and characterize the pore size distribution of Umiat cores.
- Describe the implications of obtained data from Umiat field development point of view.

Chapter 2 Background and Literature Review

2.1 Permafrost

Permafrost can be defined as a soil or other surficial deposit or even bedrock that has remained frozen (colder than 0^0C) for a period of two or more years (Andersland and Ladanyi, 2004; Muller, 1947). We distinguish between continuous permafrost, which is found everywhere in a region, and discontinuous permafrost, which is intermittent. Both the thickness and the distribution of the permafrost is directly related to the ground's thermal regime, which in turn is affected by precipitation, vegetative cover, hydrology, human and natural disturbances and so on. Figure 5 depicts the permafrost distribution in the Arctic.

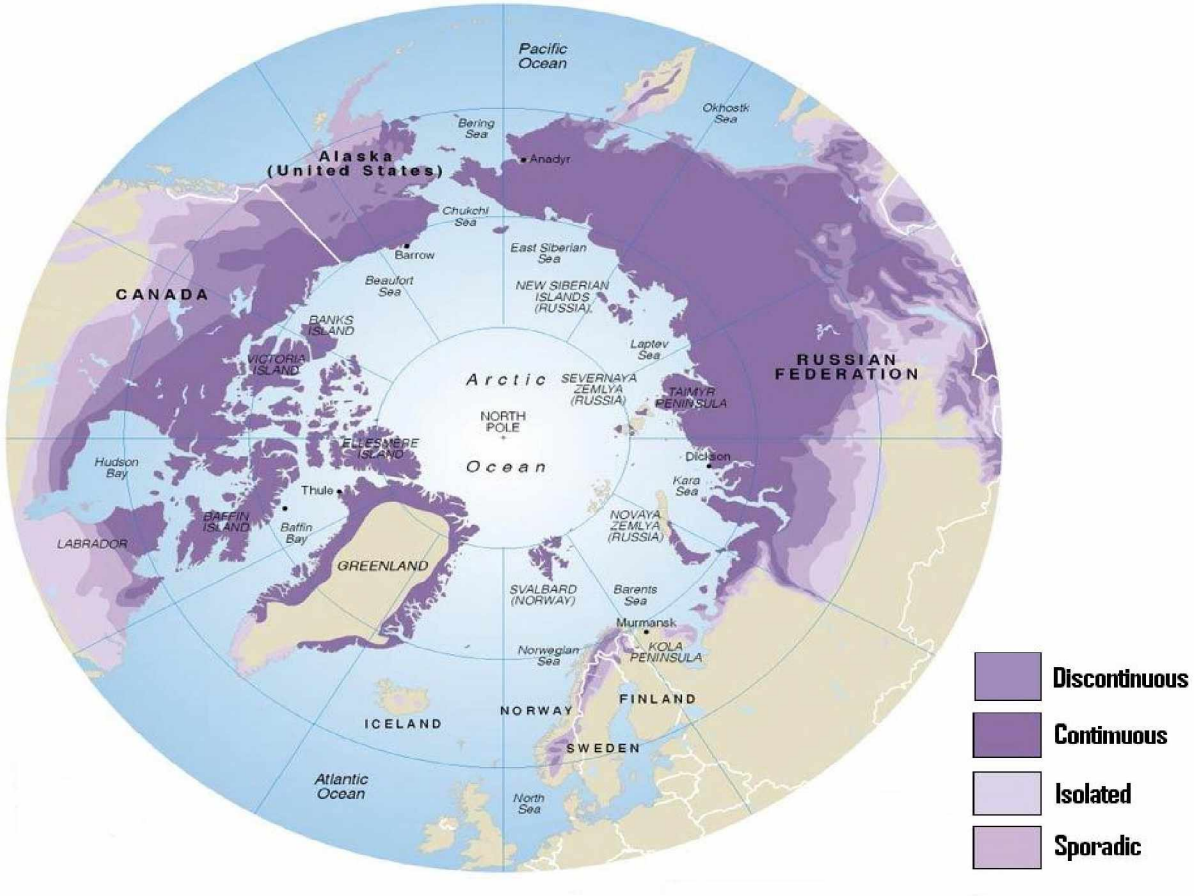

Figure 5: Permafrost Distribution in the Northern Hemisphere (International Permafrost Association, 1998)

Permafrost prevails throughout most of Alaska and its depth ranges from few inches at the southern margin to about 630 m at Prudhoe Bay. (Osterkamp et al., 1985) The Active Layer is the layer that undergoes an annual freeze-thaw cycle. In permafrost regions it is defined by the maximum depth of thaw. For the Umiat area the active layer depths usually vary from 35 to 80 cm (M. Kanevskiy, personal communication). Figure 6 represents the cross section of the permafrost.

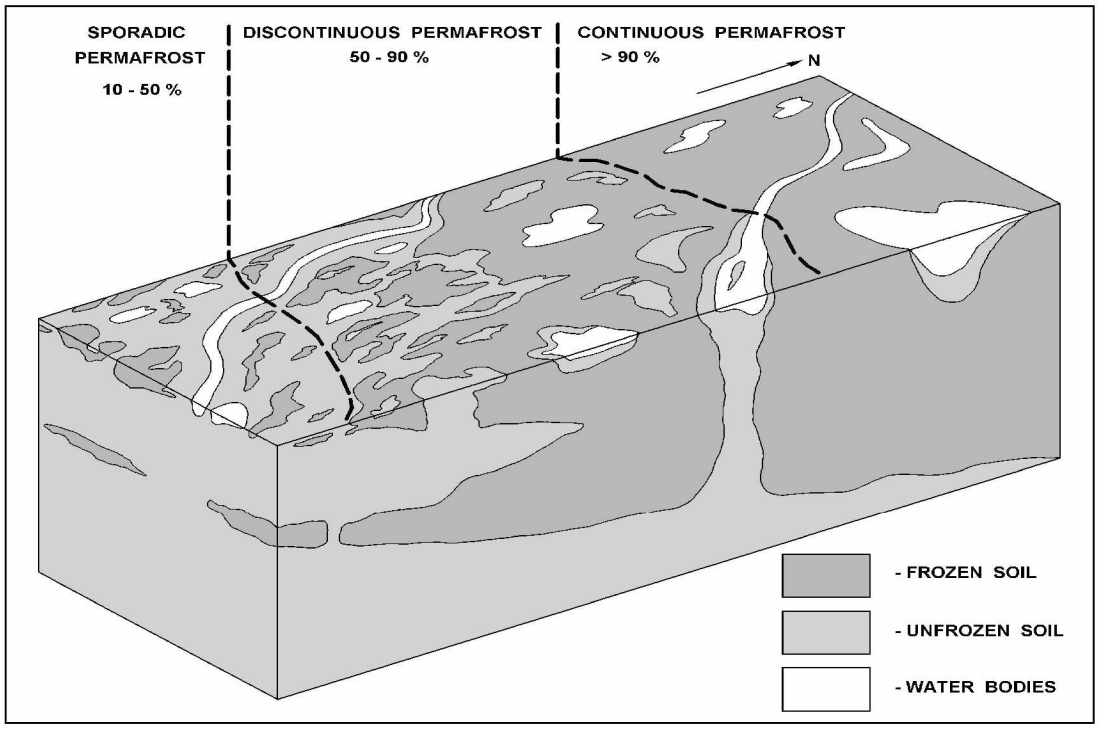

Figure 6: Cross Section of the Permafrost (Y. Shur and M. Kanevskiy, personal communication)

Permafrost appears over about 14% of the Earth's land surface. Since the mechanical properties of the soil change with freezing, in some areas the soil is frozen artificially for various engineering applications. Knowledge of these variations of physical properties is primary for the development of engineering in cold regions. The goal of this research is to study the effect of freezing interstitial water on relative oil permeability reduction.

2.2 Unfrozen Water Content

Some of the water residing in porous media, such as soil, remains unfrozen until the temperature is lowered appreciably below 0^0C (Andersland and Ladanyi, 2004). Freezing of water in pores of soil begins at approximately 0^0C. Ice initially forms in relatively large voids and then water freezes inside progressively smaller pores as the temperature falls until all pore water is frozen at -70^0C (Tsytovich, 1975). Consequently there is no single freezing point for water inside a porous media. The amount of unfrozen water primarily depends on temperature of the soil, grain size, pressure, and solute in water. At present, there are very few soils for which sufficient high-quality data on unfrozen water exist. These data are mainly derived using the different experimental methods that have been developed to measure the amount of unfrozen water in frozen soil, including isothermal calorimetry (Anderson and Tice, 1972), differential scanning calorimetry (Handa et al., 1992), nuclear magnetic resonance (NMR) methods (Tice et al., 1978) and time domain reflectometry (Spaans and Baker, 1995).

Different theories have been put forward to explain the complex phenomenon of unfrozen water in frozen soils (Smith and Low, 1996). One theory claims that the stresses existing in the soil water system are responsible. Another one, in contrast, explains it as a result of capillary effects. Nevertheless, based on experimental results, it is clear that the water-to-ice ratio is higher at any temperature for soils with small grain sizes. This ratio decreases as the temperature decreases. The amount of unfrozen water in soils also increases with increasing salinity of the water. Moreover, as the freezing of soil progresses, the salts are excluded from the formed ice, increasing the salt concentration of unfrozen water and lowering its freezing point. Based on experiments, it also has been shown that the amount of unfrozen water depends on whether the soil is freezing or thawing, and in the latter case it further depends on the lowest temperature reached during freezing (Williams, 1964).

In order to characterize the amount of unfrozen water in soil numerically, we first define the soil moisture content as follows: The soil moisture content (W) is expressed as the mass of water in the soil divided by the mass of dry soil (Andersland and Ladanyi, 2004). Typical soil moisture contents are listed in Table 3.

Table 3: Soil Moisture Contents (Andersland and Ladanyi, 2004)

Soil Type	Moisture Content (%)
Sand and Gravel	2-15
Silt	5-40
Clay	10-50
Peat	>50

The empirical equation used to plot unfrozen water content curves for non-saline soils has the following form:

$$W_u = \alpha \cdot |T|^{-\beta} \quad (1)$$

Where $|T|$ is an absolute value of measured soil temperature in degree Celsius and α and β are unfrozen water content parameters (Andersland and Ladanyi, 2004). Typical values of α and β are α=4.8, β=0.326 for Fairbanks silt and α=2.1, β=0.408 for West Lebanon gravel. Figure 7 shows unfrozen water content as a function of temperature for Fairbanks silt and West Lebanon gravel.

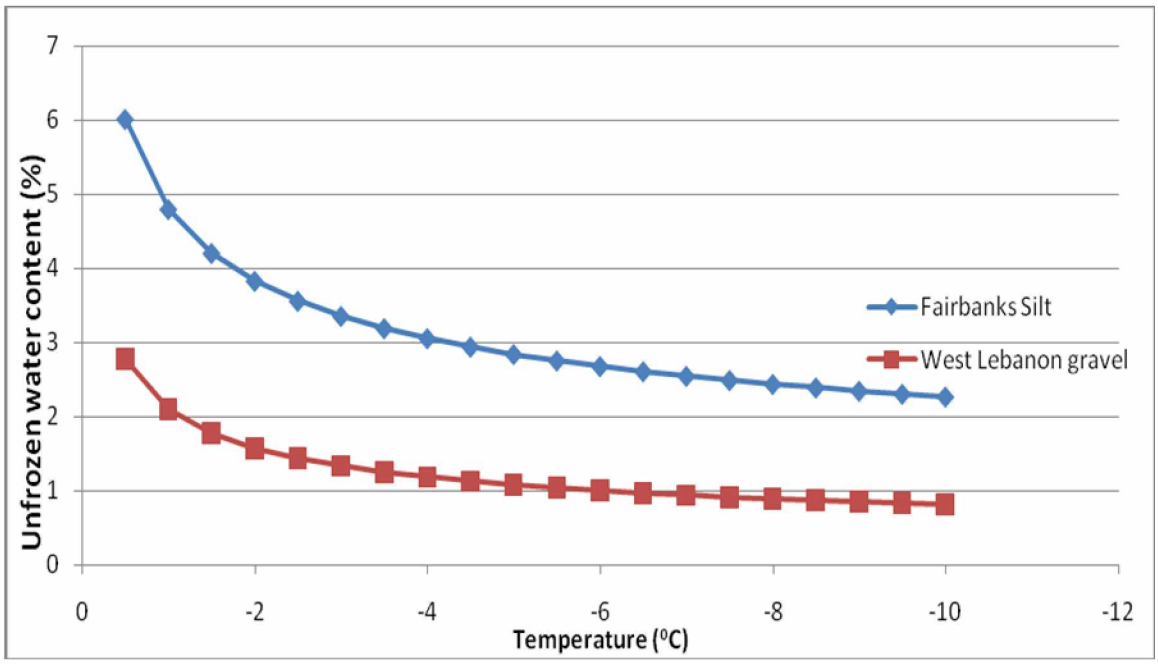

Figure 7: Unfrozen Water Content as a Function of Temperature (Andersland and Ladanyi, 2004)

Obviously the amount of ice, and therefore the unfrozen water content inside the Umiat porous media, is one of the factors responsible for oil relative permeability reduction. Consequently, it is very important to establish the relationship between these two values as well as the correspondence of unfrozen water content to the temperature variation within the Umiat reservoir.

2.3 Absolute and Relative Permeabilities

Absolute permeability is one of the key properties of a rock. By definition absolute permeability is the property of a rock that measures its ability to transmit fluids (Dandekar, 2006). Understanding the permeability characteristics of a reservoir rock helps the reservoir engineers to effectively design oil displacement processes.

Mathematically, permeability was first defined by Henry Darcy in 1856 in the following way: (Darcy, 1856)

$$K = -\frac{q \cdot \mu \cdot L}{A \cdot \Delta P} \qquad (2)$$

Where K=Permeability, Darcy

q=Flow rate through the porous medium, cm^3/sec

μ=Viscosity of the flowing fluid, cp

L=Length of the porous medium, cm

A=Cross-sectional area across which the flow occurs, cm^2

ΔP=Pressure drop across the porous medium, atm

So we say that a porous medium has a permeability of one Darcy when a single-phase fluid having a viscosity of one centipoise completely saturates the porous medium and flows through it at a rate of 1 cm^3/sec with pressure differential of 1 atm through a cross-sectional area of 1 cm^2 and a length equal to 1 cm (Dandekar, 2006).

Darcy's law is applied when the porous medium is 100% saturated with a single-phase fluid. However, in most cases the reservoir rock systems are saturated with 2 or more fluids. In order to describe the multi-phase fluid flow characteristics, engineers defined the concept of relative permeability.

In the case of any two mobile and immiscible fluid phases flowing through a porous medium, we can define any of the following two-phase relative permeabilities: (Tarek, 2001)

Gas-oil

Gas-water

Oil-water

Relative permeability is a dimensionless value and mathematically it is expressed as:

$$K_{rg} = \frac{K_{eg}}{K}, \qquad K_{ro} = \frac{K_{eo}}{K}, \qquad K_{rw} = \frac{K_{ew}}{K} \qquad (3)$$

Where K_{rg}, K_{ro} and K_{rw} are the relative permeabilities of gas, oil, and water, respectively, and K_{eg}, K_{eo} and K_{ew} are the effective permeabilities of gas, oil, and water phases, respectively, at a specified saturation of that phase. From this definition it follows that

when reporting the relative permeability of a particular fluid, it is necessary to specify the saturation of that fluid.

Typically the relative permeability data are presented in the form of relative permeability curves. Figure 8 represents a typical gas-oil relative permeability curve.

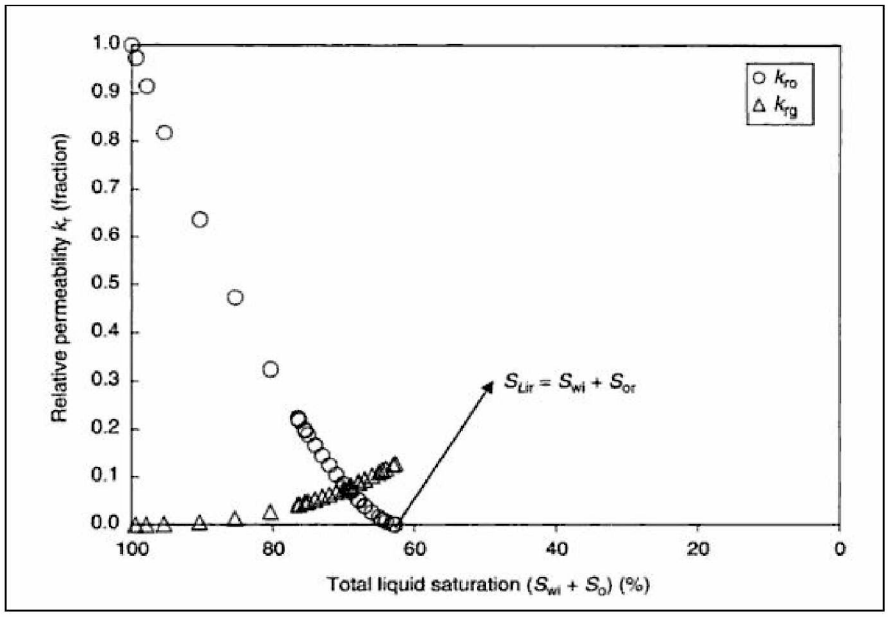

Figure 8: A Typical Gas-Oil Relative Permeability Curve (Dandekar, 2006)

In the case of gas-oil relative permeability, the curves always represent the drainage process because the non-wetting phase (gas) is displacing the wetting phase (oil) (Oil is the wetting phase relative to the gas) (Dandekar, 2006). Constructing these drainage gas-oil relative permeability curves is very important for hydrocarbon recovery processes if the primary production is based on solution gas drive mechanism, as it is one of the methods under consideration in the case of Umiat.

2.4. **Oil Recovery from Frozen Reservoir Rocks**

For the last few decades petroleum operations have increased significantly in the Arctic frontier regions (Goodman, 1978). Production of hydrocarbons in severe Arctic environments is associated with many interesting challenges and the operators face unique problems caused by a cold climate and permanently frozen ground. Permafrost behavior associated with thawing and freezing is one of the most important factors affecting well design in most Arctic locations. Petroleum operations such as drilling, completion and production of oil will result in permafrost thawing unless some mechanisms are used to prevent heat flow away from the wellbore. For example, it was estimated that at Prudhoe Bay and Mackenzie Delta permafrost thaws about three feet around the wellbore due to drilling and about 50 feet due to 20 years of production with uninsulated wells.

Thawing of permafrost leads to ground subsidence and additional loads on the wellhead and wellbore system (Goodman, 1978). Another common problem that comes into the picture while producing oil in the Arctic is external freezeback. This involves the refreeze of thawed permafrost or water-based fluids outside the casing when a well is shut in during or after drilling or after a short production period. It has been observed that compaction due to thaw is not mechanically reversible during freezeback, and as a consequence inward radial loads, known as freezeback pressures, are generated around the wellbore. This pressure can reach significant levels because, as it was observed at Prudhoe Bay, permafrost does not fracture or creep to eliminate freezeback pressure.

Engineers have developed different thermal protection systems in order to reduce permafrost thaw around Arctic wellbores (Goodman, 1978). The use of gelled packer fluid in casing annuli is one mechanism to limit thaw. Figure 9 shows 20 year thaw profiles for Prudhoe Bay Well with various thermal protection methods.

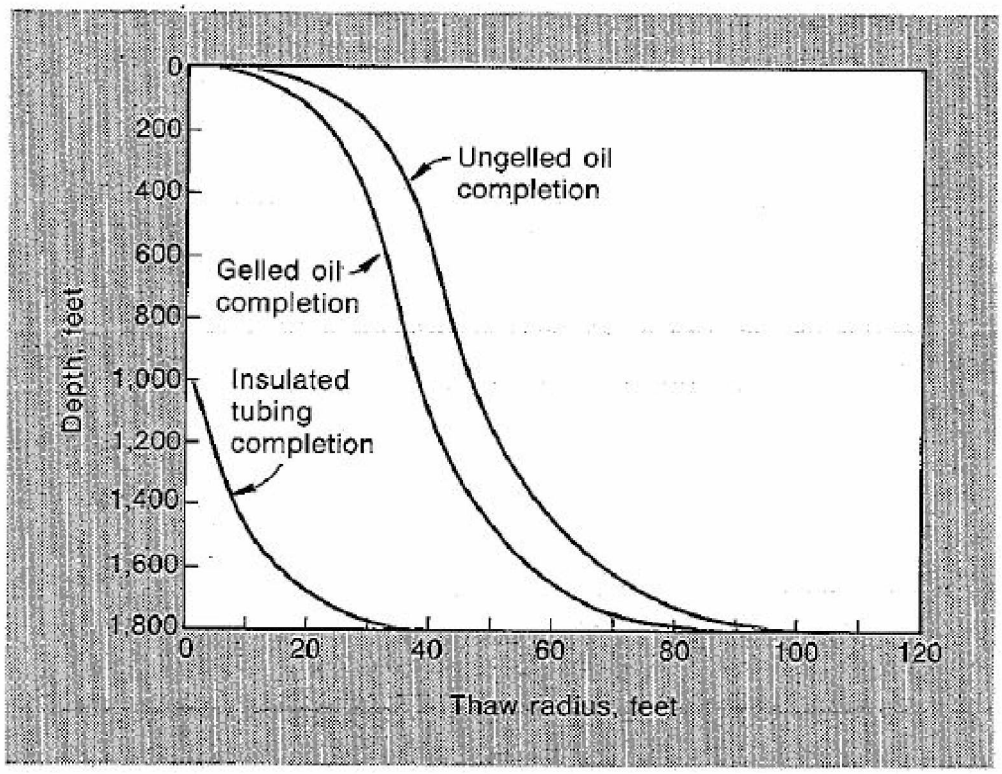

Figure 9: Twenty Year Thaw Profiles for Prudhoe Bay Well with Various Thermal Protection Methods (Goodman, 1978)

The figure shows that use of gelled oil packer in contrast with ungelled oil fluid reduced thaw by about 20% (Goodman, 1978). A novel feature of the gelled oil-based fluid is that the gelling agents will not dissolve in oil at temperatures less than 50^0F but at higher temperatures the oil-based system gels to grease-like consistency. This is very convenient for Arctic applications because the system can be prepared at surface temperature and easily pumped into casing annuli. Then it will be heated to producing temperatures and consequently it will gel and gain the desired insulating properties. Another approach to the above-mentioned problem implies the use of double-walled insulated tubing and casings. Figure 10 shows double-walled insulated casing string.

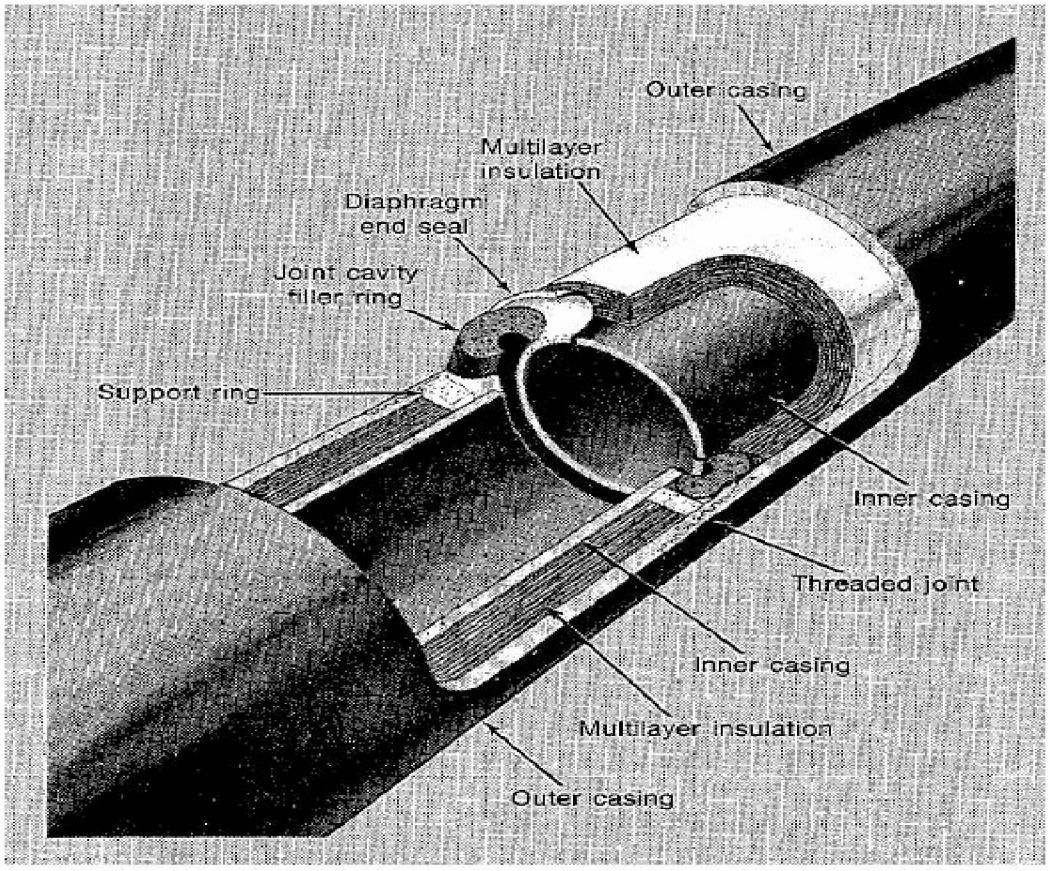

Figure 10: Double-Walled Insulated Casing String (Goodman, 1978)

Absolute prevention of thaw of permafrost requires not only insulation but also refrigeration (Goodman, 1978). This is done by circulating coolant through coils or using heat pipes. At present, heat pipes have not been installed near the wells but they are extensively used along the Trans-Alaska Pipeline in order to provide stability for pipe supports in permafrost.

Another challenging phenomenon found while drilling in Arctic locations is gas hydrates, or ice crystals in which gas molecules are trapped (Goodman, 1978). Naturally, gas hydrates are found in deep marine sediments as well as in permafrost formations. Imperial Oil, Ltd reported significant amounts of gas liberated as a result of the decomposition of hydrates while drilling through hydrate-bearing zones in the Mackenzie Delta area.

Increasing mud weight is not effective in controlling mud gasification, and unless proper precautions are taken mud becomes highly gasified and engineers face well control problems. Generally, while drilling through hydrate zones, engineers use mud cooled to the hydrate equilibrium temperature.

Upon dissociation, hydrates are capable of supplying large volumes of gas, primarily methane (Jaiswal, 2004). For this reason, gas hydrates are considered a vast source of potential future energy. For this purpose, gas-water relative permeability experiments for hydrate-saturated cores were conducted in the petroleum engineering department of University of Alaska Fairbanks. As far as challenging conditions for relative permeability measurements are considered, these experiments are probably the closest to gas-oil relative permeability experiments under simulated permafrost conditions. The author of the experimental research constructed the relative permeability curves using an unsteady-state core flooding method and concluded that the gas-water relative permeabilities are essentially affected by the distribution and growth of hydrate within the core sample.

Based on the author's extensive research, out of the many fields that are located in the Arctic region, the Nordvik oil field in Russia is the only field that has ever produced from a reservoir within the permafrost. The rest of the oil fields produce from horizons below permafrost. Geographically the Nordvik field is located on the Yurung-Tumus Peninsula (Lappo, 1946). The maximum depth to the base of permanently frozen ground is 540m. The lowest subsurface temperature, -12.7^0C, was recorded at the depth of 56-60m and it increases upward and down according to geothermal gradient, 1^0C/35m. Oil was first discovered by T.M. Emeliantzev in 1933 during the geological reconnaissance of the region. Two wells, K401 and K402 were drilled at that time and signs of hydrocarbon depositions were found at depths of 105m and 30m respectively. Later in 1944, several more wells were drilled and 104 cores and several oil samples were sent for laboratory analysis. Tests showed that in many areas porosity is up to 30% and mostly it varies between 23-26%. The average permeability is about 62md and the cores with maximum

permeability of 93.4md and 92.3md were cut at depth of 219m and 120m in the wells K462 and K429 respectively. Laboratory analysis also showed that the oil samples taken from the Triassic deposits have 18.6^0API gravity with 29% of light fractions. However, the samples taken from the Permian horizons have higher API gravity in the range of 35.8^0-39.2^0API with 50-56% of light fractions which makes it as one of the high quality oils produced from different oil fields in former Soviet Union. Very low oil flow rates, about 3-5 bpd, from the wells completed within the permafrost was explained as a result of increased oil viscosity due to low temperatures. Moreover, shortly after the start of production, the operator was required to shut in the Nordvik field because of ground subsidence. (Gaffney, Cline & Associates, 2006)

2.5 **Laboratory Methods for Determining Absolute Permeability**

Absolute permeability, as it was defined in section 1.3, is one of the key properties of the rock and it should be estimated with accuracy in order to effectively design oil displacement processes.

Laboratory experiments are carried out on core plugs, small pieces cut from the conventional core samples (Dandekar, 2006). Permeability is generally determined by passing a fluid with known viscosity through a core plug of measured dimensions and then measuring the flow rate and the pressure drop across the plug. Having all these data, we find the absolute permeability using the formula (2). This procedure will generally provide reliable data if the fluid used is incompressible, but if the fluid is compressible, such as a gas, then Darcy's law needs to be modified as follows:

$$Q_{gsc}P_{sc} = q_m P_m \quad (4)$$

Where,

$$q_m = \frac{K \cdot A \cdot (P_1 - P_2)}{\mu_g \cdot L} \quad \text{and} \quad P_m = \frac{P_1 + P_2}{2} \qquad (5)$$

So,

$$Q_{gsc} P_{sc} = \frac{K \cdot A \cdot (P_1 - P_2)}{\mu_g \cdot L} \times \frac{P_1 + P_2}{2} = \frac{K \cdot A \cdot (P_1^2 - P_2^2)}{2 \cdot \mu_g \cdot L} \qquad (6)$$

And hence,

$$K = \frac{2 \cdot Q_{gsc} \cdot P_{sc} \cdot \mu_g \cdot L}{A \cdot (P_1^2 - P_2^2)} \qquad (7)$$

Where,

K=Absolute permeability, Darcy

Q_{gsc}=Gas flow rate at standard conditions, cm^3/sec

P_{sc}=Atmospheric pressure, atm

μ_g =gas viscosity, cp

L=Length of the core plug, cm

A=Cross sectional area, cm^2

P_1=Inlet pressure, atm

P_2=Outlet pressure, atm

P_m=Mean pressure, atm

q_m=Mean gas flow rate, cm^3/sec

Klinkenberg (Klinkenberg, 1941) discovered that measurements of permeability made using gas are always greater than those made using liquid. He explained this phenomenon as a gas "slippage," meaning that the gas exhibits some finite velocity at the sand grain surface, while the liquid has zero velocity at the sand grain surface. This allows gas to flow with a higher rate at a given pressure differential. Klinkenberg also found that as the mean pressure (P_m) increases infinitely, the permeability measured using the gas (K_g) approaches the permeability measured using the liquid (K_L), i.e. the absolute permeability. He expressed this relation in the following way:

$$K_g = K_L + C \times \frac{1}{P_m} = K_L + b \cdot K_L \times \frac{1}{P_m} \qquad (8)$$

Klinkenberg suggested that the constants C and b are dependent on different factors, such as absolute permeability, type of gas and average radius of rock capillaries. So if we take the Klinkenberg effect, formula (8), into account in formula (7), then it is necessary to measure the gas permeability for at least two different mean pressures to get the absolute permeability.

If the rock is not homogeneous or if cutting the core plugs is technically impossible, then the whole core analysis is considered. In this case the device called "probe permeameter" is favored. This apparatus uses the compressed air which is injected into the sample and then monitors the decline in pressure with time. Based on this relationship the enclosed software, PLAB-200 Ver. 2.05, calculates the permeability.

2.6 **Laboratory Methods for Determining Relative Permeabilities**

The following two sections will discuss the most common flow experiments for determining the relative permeabilities:

1. Steady-State (SS)
2. Unsteady-State (USS).

2.6.1 **Steady-State Technique**

The steady-state method was first developed in 1939 by Leverett (Leverett, 1939). Each step of the procedure involves the simultaneous injection of two phases, at a certain volumetric ratio, into the core plug. The injection continues until the pressure drop across the core plug is stabilized and the influent and effluent volumetric ratios are equal. This condition is called a Steady-State condition. Once we reach this condition, the core has to be removed from the core holder. Then, using the mass-balance equation, we find the fluid saturations. At these saturations we can find the effective permeability of each fluid

using Darcy's law. Dividing the effective permeabilities by absolute permeability or by the effective permeability to oil at irreducible water saturation, we get the relative permeabilities. In subsequent steps, we progressively increase the volumetric ratio of injected fluids, and once we reach the steady-state condition we find the new saturations of fluids and their relative permeabilities.

Calculation of relative permeabilities using the steady-state method is very simple, but from a practical point of view, the experiment is very time consuming. This is because at each step we need to wait until achieving the steady-state condition. Also, at each step we need to remove the core from the core holder and this might result in fluid loss, especially if we are measuring gas-oil relative permeabilities.

2.6.2 **Unsteady-State Technique**

For performing the laboratory experiments, the unsteady-state technique is easier than steady-state technique, but it requires much more data processing. This technique was used in this work and it is based on the theory of immiscible displacement. In the case of gas-oil and oil-water relative permeabilities, the displacing phases are gas and water, respectively (Johnson et al, 1959). As far as the experimental procedure is concerned, in both cases the displacement process begins when the water saturation is at irreducible water saturation ($S_w=S_{wi}$) and the oil saturation is equal to $S_o=1-S_{wi}$. After that, the procedure involves recording the cumulative oil production rate as well as the cumulative injection rate of the displacing fluid in terms of the pore volume. The common method, which was also used in this work, for analyzing these data is the Johnson-Bossler-Naumann (JBN) method (Johnson et al, 1959). The theory of immiscible displacement process and JBN method are presented in Appendix A.

2.7 **Capillary Pressure Measurement**

When two immiscible fluids are present in a petroleum reservoir, there exists a discontinuity in pressure at the interface separating these fluids (Tarek, 2001). This pressure difference is called the capillary pressure and it is denoted by P_c. In other words, in order to maintain a porous medium saturated with both wetting and nonwetting fluids, it is necessary to maintain the pressure of the nonwetting fluid at a value of P_c greater than that in the wetting fluid. So,

$$P_c=P_{nw}-P_w \quad (9)$$

Where,

P_{nw}, P_w=Pressure of nonwetting and wetting fluids respectively.

Obviously, the capillary pressure depends on saturation of these fluids. It also depends on the surface and interfacial tensions of the rock and fluids, pore size and geometry, and the wetting characteristics of the system.

One of the most important applications of the capillary pressure concept is to convert the capillary pressure-fluid saturation data into height-saturation data, by which means we can find the water saturation distribution as a function of distance from the free water level in an oil-water system (Tarek, 2001). There is no abrupt change in saturation from 100% water saturation to maximum oil saturation, and this is exactly due to the existence of capillary pressure. Thus, knowing the capillary pressure data is vital for determining the thickness of transition zone.

As far as the laboratory methods are concerned for measuring the capillary pressure data for reservoir rock samples, the mercury injection technique is one of the most popular methods. The method was originally proposed by Purcell in 1949, which was used in this work to obtain capillary pressure data for 3 Umiat core plugs.

The experimental procedure is very simple (Purcell, 1949). A clean and dried core of known pore volume is placed in a mercury pycnometer. Applying the subsequently-

increasing pressure of nitrogen and calculating the volume of mercury that has invaded the core plug, we can construct the drainage capillary pressure-saturation curve for an air-mercury system. In order to convert the capillary pressure data from an air-mercury system to a water-kerosene and kerosene-air system, σ_{am}=487 dynes/cm, σ_{wk}=48 dynes/cm, and σ_{ka}=27 dynes/cm surface and interfacial tension values were used (www.wikipedia.org). A commonly used formula for converting the data (ignoring the contact angles) is as follows:

$$P_{cwk} = P_{cam} \times \frac{\sigma_{wk}}{\sigma_{am}} \quad and \quad P_{cka} = P_{cam} \times \frac{\sigma_{ka}}{\sigma_{am}} \qquad (10)$$

Where,

P_{cwk}, P_{cam}, P_{cka}=Capillary pressure for water-kerosene, air-mercury and kerosene-air systems respectively.

σ_{wk}, σ_{am}, σ_{ka}=Interfacial tension between water-kerosene and surface tensions between air-mercury and kerosene-air respectively.

Chapter 3 Experimental Work

3.1 Experimental Setup

Figure 11 shows the schematic of the experimental setup which was completely designed and assembled by the author of the thesis at the University of Alaska Fairbanks. The major constraint while designing the setup was to provide the flow of three different phases, water, oil and gas through the core samples both at room temperature and at simulated permafrost conditions. As seen from this figure, some of the apparatus is inside the freezing chamber and the rest is outside. Hence, the setup can be conditionally subdivided into inside and outside parts. The apparatus consists of two pumps, four accumulators, a core holder, four pressure gauges, a hydraulic hand pump, an electronic balance, a glass accumulator, a nitrogen gas cylinder, a gas flow meter, a back pressure regulator, a computer and a freezing chamber.

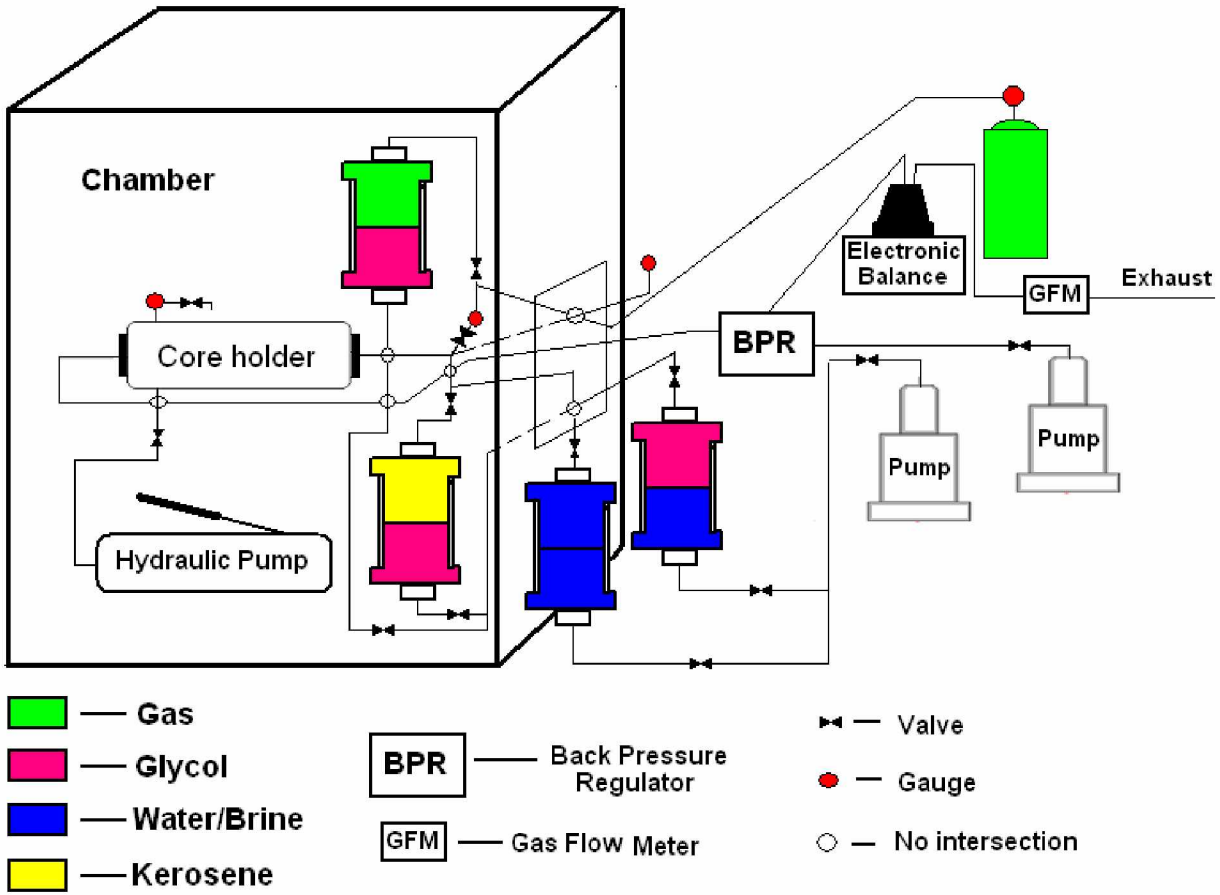

Figure 11 Schematic of the Experimental Setup

Core holder

One Temco RCHR-1.5 series core holder: The core holder, which is located inside the freezing chamber, holds the core sample. It can accommodate cores 1.5 inches in diameter and up to 12 inches long.

Pumps

Two Isco Series pumps 500D and 100DX: The first is used to control the flow of fluids at either constant flow rate or constant pressure. The second is used to maintain the constant pressure at the outlet. Both pumps are installed outside the freezing chamber.

Accumulators

Four cylindrical type accumulators: One is used for brine/deionized water flooding; the second is used for oil (kerosene) flooding, the third is used for gas injection and the fourth is used as an intermediate accumulator full of glycol between the pump and kerosene and gas accumulators. The oil and gas accumulators are inside the freezing chamber and the glycol and water accumulators are outside the chamber. Each accumulator has a piston inside which pushes the fluid towards the outlet of the accumulator. For those accumulators which were placed inside the chamber, glycol was used in order to push the piston and remain unfrozen at low temperatures.

Hydraulic hand pump

One Enerpac P-141 hydraulic hand pump: It is used for pumping the hydraulic oil in the annular space between the rubber sleeve and the metal jacket of the core holder. The purpose of the pump is to simulate the overburden pressure and to make sure that all the fluid goes through the core sample without bypassing it. The hydraulic hand pump is placed inside the freezing chamber.

Pressure gauges

Four pressure gauges: The Heise digital gauge is located at the inlet of the core holder to measure the pressure at one side of the core sample. The second gauge is installed between the hydraulic hand pump and the core holder to measure the confining pressure applied on the sample. The third gauge is installed at the outlet of the gas accumulator to measure the nitrogen pressure during the gas injection process. The fourth gauge is placed on the gas supply cylinder to measure the available gas pressure.

Freezing chamber

One Tenney T30C-2 Freezing chamber: It is used for freezing the core sample at connate water saturation inside the core holder to simulate the reservoir rock in the permafrost region. The chamber has a small insulated window to establish the connection between the inside and outside parts of the experimental setup.

Electronic balance

One AND GF-4000 electronic balance. This model of balance has fairly good accuracy; deviation between the actual and displayed weights is in the range of ±0.002g. It is used to measure the mass of produced oil as a function of time during the gas injection. The balance is connected to the Dell computer for logging the data using preliminary defined time intervals.

Glass accumulator

One enclosed glass accumulator: It is located on the electronic balance to collect the produced oil and separate it from the nitrogen during the gas injection.

Gas flow meter

One Aalborg gas flow meter: It is used to measure the volume and flow rate of injected nitrogen during the gas injection process. GFM transfers the data to the Dell computer for logging with specified time intervals.

Gas cylinder

One nitrogen gas cylinder: It is used for gas supply.

Back pressure regulator

One Temco BP Series back pressure regulator: It is used to apply constant pressure at the outlet of the core holder.

Computer

One Dell computer: Several types of logging software, such as RsCom Ver.2.40 for electronic balance and IOTerminal Ver.1.06 for gas flow meter, were installed on the computer and set to record the values at identical time intervals. At a later period, this data was analyzed with Microsoft Excel to determine the gas-oil relative permeabilities using the JBN method.

Figure 12 and figure 13 depict the details of the experimental setup.

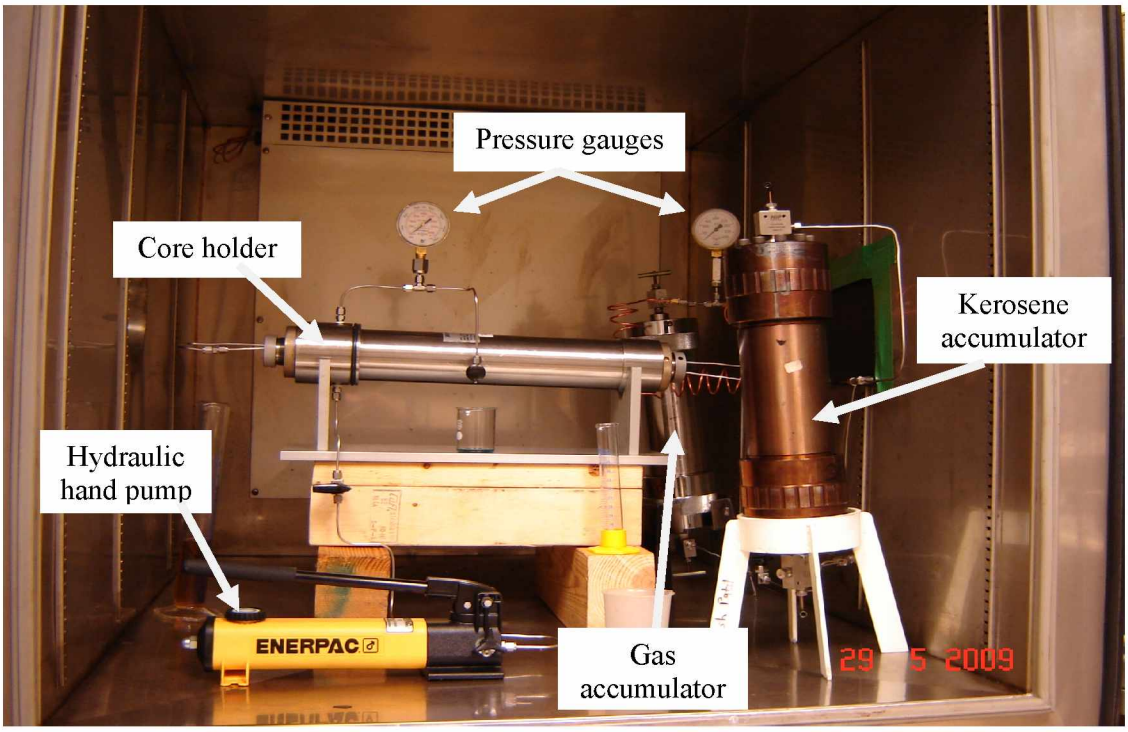

Figure 12: Inside Part of the Experimental Setup

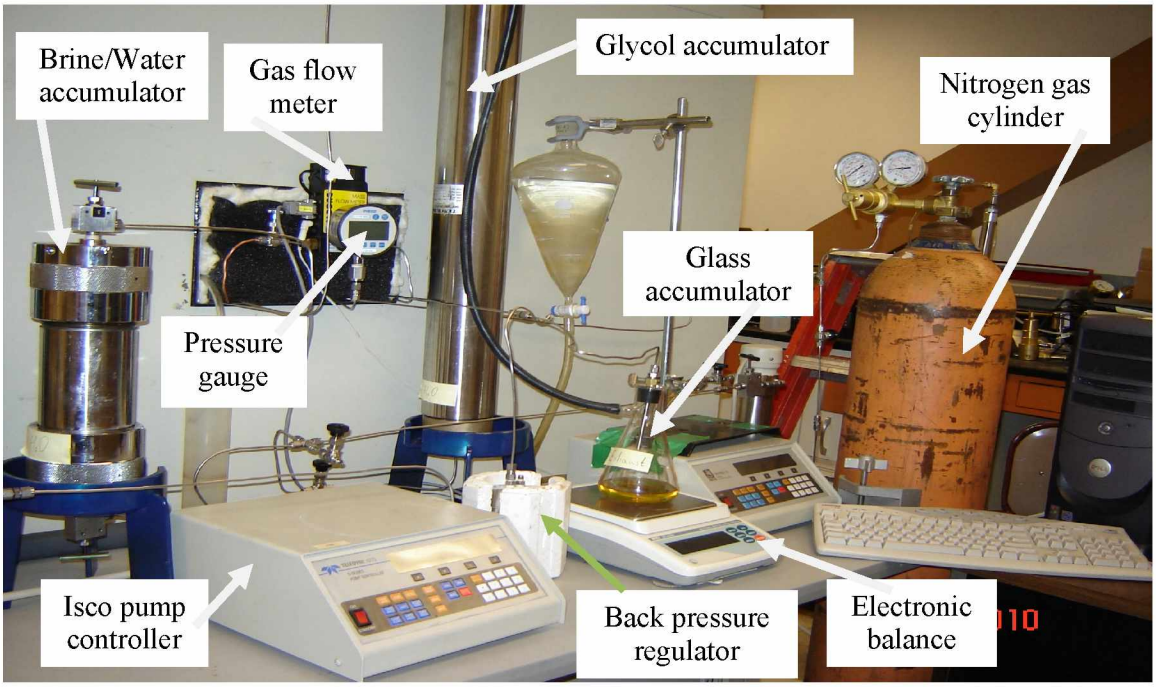

Figure 13: Outside Part of the Experimental Setup

Figure 14 shows the Temco's high pressure mercury injection apparatus.

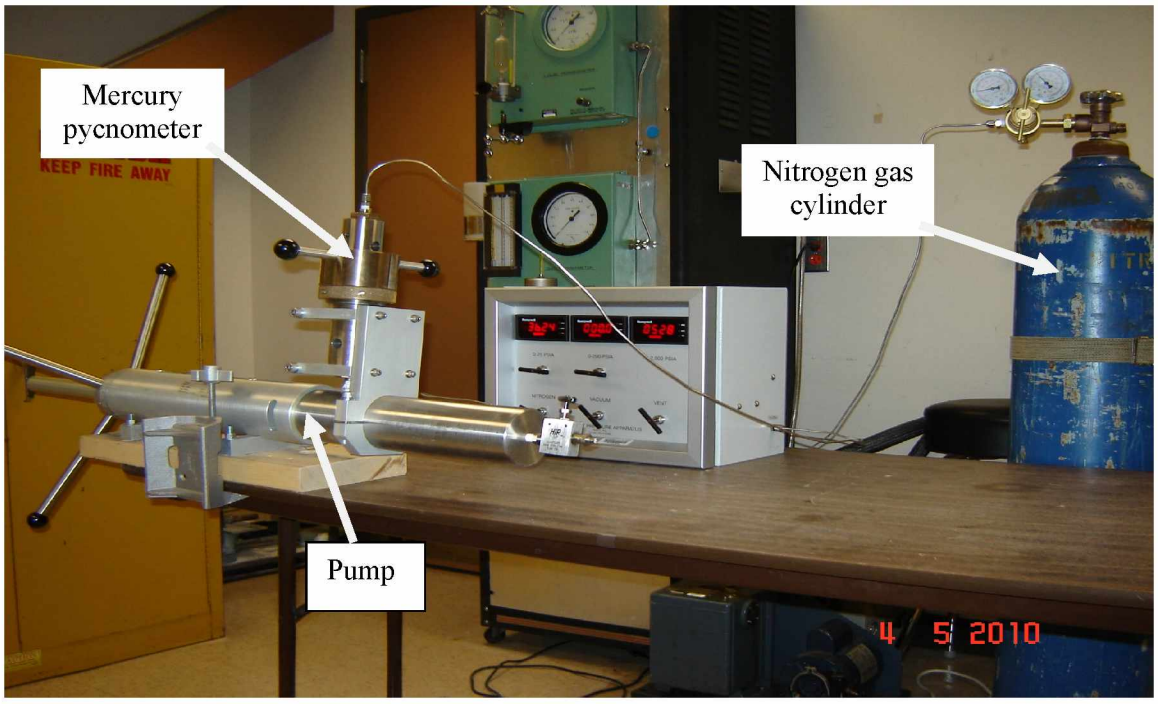

Figure 14: Temco's High Pressure Mercury Injection Apparatus

3.2 **Experimental Procedures for Core Flooding Experiments**

Flow experiments were carried out for six Umiat core plugs, including the following steps: (Dandekar, 2006)

Step 1: Core plug is first cleaned with toluene and then with acetone. Upon cleaning, the core is placed in the oven at 80^0F to dry for 2 days. Dry weight is periodically checked over this time interval to make sure that it has reached some constant value.

Step 2: Dry weight (DW) and the dimensions, d=diameter and L=length, of the core are measured. Bulk volume (BV) of the core is determined by the following formula,

$$BV = \pi \cdot \frac{d^2}{4} \cdot L \quad (11)$$

Step 3: Density of kerosene at 22^0C ($\rho_o = 0.776\,\text{g/cm}^3$) and viscosity both at 22^0C and -10^0C are measured by Anton-Paar density meter and viscometer, μ_o@ 22^0C=1.15 cp and μ_o@ -10^0C=1.78 cp.

Step 4: Core plug is 100% saturated with the corresponding water sample. This is achieved by placing the core in a flask with water and applying vacuum, generally for 2 or 3 days. Wet weight is monitored over this time interval to make sure that it has reached some constant value and the core is fully saturated with water. After saturation, the wet weight (WW) of the core plug is measured and pore volume (PV) and porosity (ϕ) are calculated by the following formulae:

$$PV = \frac{WW - DW}{\rho_w} \qquad and \qquad \phi = \frac{PV}{BV} \times 100\% \quad (12)$$

Where ρ_w is the density of the corresponding water sample.

Step 5: Core is placed inside the core holder, and after the confining pressure is applied, (generally 500 to 600 psi), the core is flooded by the water sample at a constant flow rate q_w=0.3 ml/min. The flow continues until the pressure stabilizes at the

inlet of the core holder. After that, absolute permeability (K_{abs}) of the core plug is determined using Darcy's law, formula (1).

Step 6: Core is flooded with oil (kerosene) at the same flow rate, 0.3 ml/min, until there is no more water production from the outlet and the pressure stabilizes at the inlet of the core holder. At this stage the water saturation inside the core plug is reduced to irreducible water saturation and we can determine the effective permeability of kerosene at irreducible water saturation $K_{eo}@S_{wi}$ using Darcy's equation.

Step 7: Core is taken out of the core holder and its weight (M) is measured. Irreducible water saturation is calculated with the following mass balance equation:

$$S_{wi} = \frac{M - DW - PV \cdot \rho_o}{PV \cdot (\rho_w - \rho_o)} \times 100\% \quad (13)$$

On the other hand, irreducible water saturation is also calculated volumetrically, by subtracting the volume of produced water from the pore volume and dividing by the pore volume,

$$S_{wi} = \frac{PV - Q_{wp}}{PV} \times 100\% \quad (14)$$

Step 8: Core is placed back inside the core holder and gas (nitrogen) injection procedure begins at constant flow rate. Different flow rates in the range of 0.008-2.75cm^3/sec were used for different core plugs. Cumulative oil production, cumulative gas injection, gas flow rate and pressure differential across the core plug are recorded every 2 seconds by the electronic balance and the gas flow meter. The recorded data are transferred to the computer and processed according to the JBN method described in Appendix A. Gas injection process ends at residual oil saturation.

Step 9: Repeat the following steps: 1, 4, 5 and 6. Turn on the chamber and run it at -10^{0}C set point temperature for approximately one day. This is the necessary time frame to establish the constant temperature at the surface of the core holder. Repeat step 6 and calculate $K_{eo}@S_{wi}$(ice).

Step 10: Repeat step 8.

3.3 **Experimental Procedures for Capillary Pressure Measurement Experiments**

Capillary pressure measurement procedure involves the following steps:

Step 1: Calculate and plot volume correction factors at different pressures. For this purpose we advance the piston of the mercury filled pump until the mercury level reaches some reproducible level in the top window of the pycnometer. Record the pump volume as $V_{initial.}$ Open the nitrogen valve and apply subsequently increasing pressures, P_1, P_2, P_3, …, P_n, to the pycnometer. Keeping in mind that maximum pressure rating of the pycnometer is 2000psi, do not exceed this value. Each time the level of mercury will be dropped because of mercury compaction. Advance the piston until the mercury reaches the reproducible level in the top window and record the pump volume before applying new pressure. As a result we will get some increasing sequence of pump volume readings, V_1, V_2, V_3, …, V_n. Now for each applied pressure value P_i, we calculate the corresponding volume correction factor as $V_{i,corr} = V_i - V_{initial}$ and we plot them.

Step 2: Release the pressure and retract the pump to lower the level of mercury. Place cleaned and dried core plug of known pore volume, V_p, inside the pycnometer and advance the piston until the mercury level reaches the reproducible level in the top window of the pycnometer. Record the pump volume as $V_{initial.}$ Apply subsequently increasing pressures to the pycnometer (Not necessarily the same as in step 1). Each time the level of mercury will be dropped as a result of compaction and invasion in the core plug. Advance the piston until the mercury reaches the reproducible level in the top window and record the pump volume before applying new pressure. Each time calculate the total volume of injected mercury in the core plug as: $V_{inj} = V_n - V_{initial} - V_{corr.}$ Where V_n is the pump volume at each new pressure and V_{corr} is the volume correction factor for that pressure. Also calculate the gas saturation inside the core sample for each step as follows:

$$S_g = \left(1 - \frac{V_{inj}}{V_p}\right) \times 100\ \% \qquad (15)$$

Step 3: In order to obtain the drainage capillary pressure curve for air-mercury system, plot the applied pressures as the values of capillary pressure, P_c in psia, versus gas saturations, S_g in percentage.

3.4 **Core Samples**

Conventional core samples from Umiat well #11 were collected by Grant Shimer (G. Shimer, personal communication). After approval of his sample request form by Kenneth Papp, the director of GMC in Eagle River, Grant selected the sample sites that were not previously sampled. Having an intention to find samples from high quality reservoir sands, core samples with potentially high porosity and permeability were selected based only on visual observations of grain size and sorting due to the absence of engineering tools on site. Overall eight core samples were selected representing Ninuluk, Chandler, Upper Grandstand and Lower Grandstand formations present in Umiat well #11. Figure 15 shows the lithology log of the well #11 and the core samples taken from each formation.

Four samples were slabbed and the rest were cylindrical in shape. Some of them had visually observable fractures. All cores had the diameter equal to 7.78 cm and their lengths were in the range of 8.18-13.49 cm. Depth of the samples ranges between 2124 and 2993 feet. Based on the data presented in table 1, we can conclude that none of these samples are cut from the permafrost, because the depth to the permafrost base in well #11 is 770 feet.

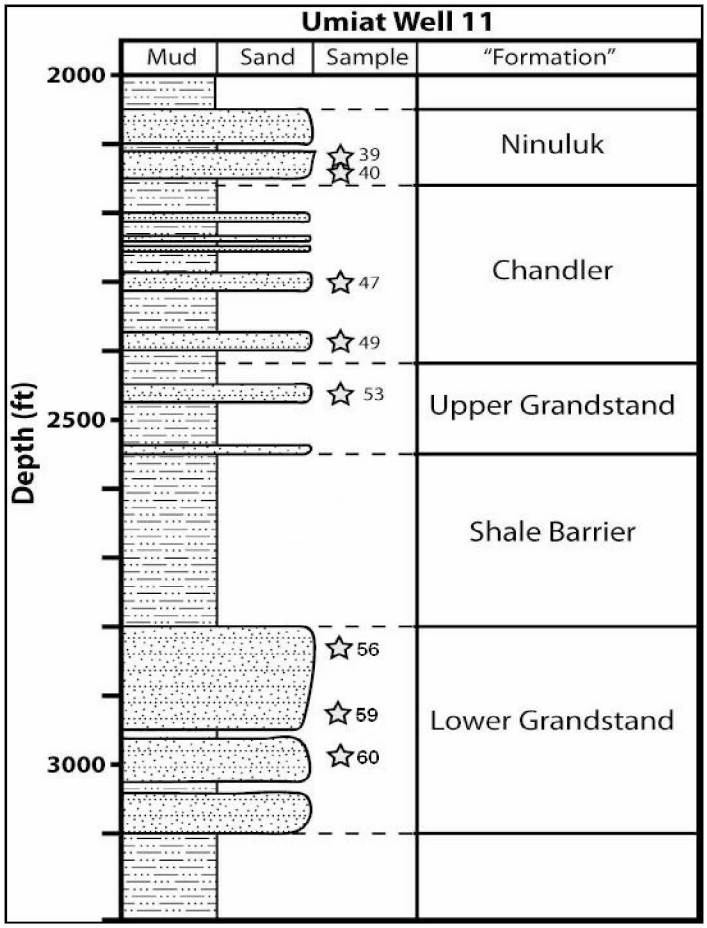

Figure 15: Lithology Log of the Umiat Well 11 (G. Shimer, personal communication)

The following steps were performed in order to prepare core plugs for flooding experiments:

Step 1: Log sheet was prepared for all conventional core samples, see Table 4.

Step 2: Horizontal and vertical air permeability measurements were made for all the samples using the probe permeameter. Figure 16 shows the probe permeameter in the process of permeability measurements. The device does not measure Klinkenberg corrected permeabilities but the manufacturer claims that the Klinkenberg effect is minimized by keeping the test pressure at a low level (UPP-200^{TM} probe permeameter operating manual). Results are presented in Table 4.

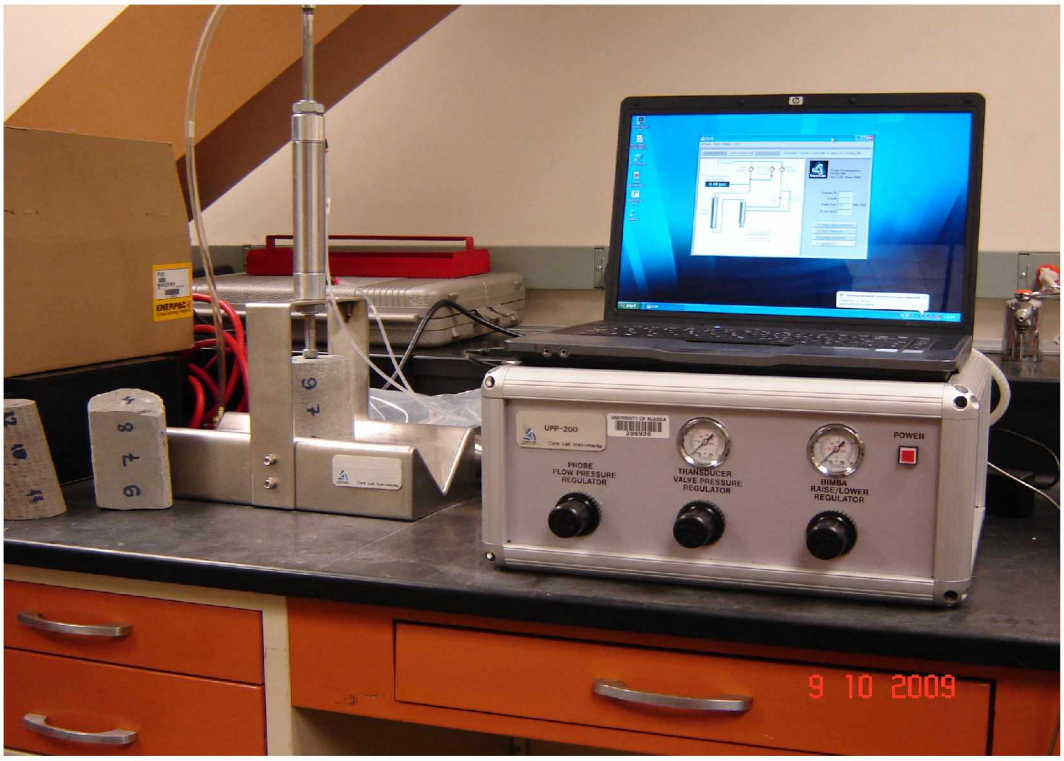

Figure 16: Picture of Probe Permeameter

The first six permeability measurements in Table 4, K1-K6, express the vertical permeability and the last nine measurements, K7-K15, describe the horizontal permeability. For the slabbed samples, the angle between the horizontal measurements is 180^0. Otherwise the angle is equal to 120^0. Figure 17 shows the schematic of a core sample and all the spots from which the permeability measurements were taken. It was practically impossible to take the measurements from some spots of the cores because of their shape and length. This explains some of the omitted values in Table 4.

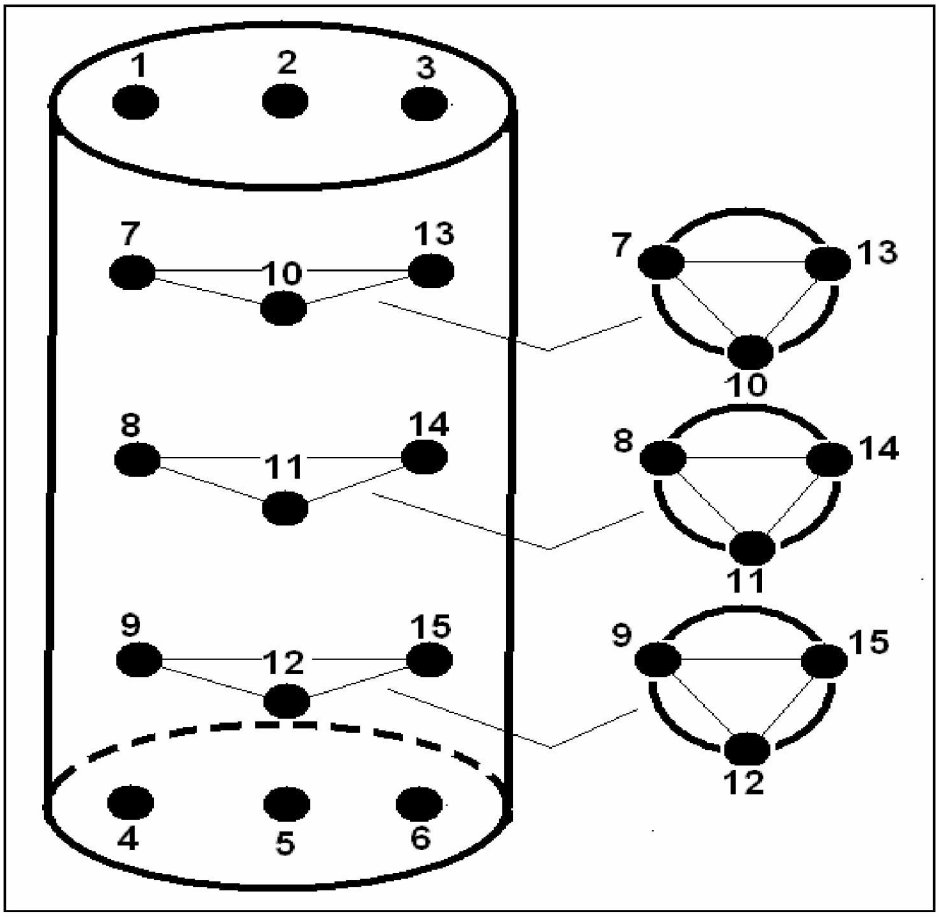

Figure 17: Schematic of a Core Sample and Reference Points for Permeability Measurements

Step 3: Six core plugs with 1.5 inch diameters were cut from conventional core samples 40, 49, 53, 39, 47 and 60. Side labels 1, 2, 3, 5, 6 and 8 were made to the corresponding core plugs. Core 59 was collapsed during the drilling process and core 56 was useless for drilling because of high fracture density. After being used for relative permeability experiments, the cores 53, 47 and 60 were also used for capillary pressure measurements. Figure 18 and Figure 19 show the drill bit and the core plugs respectively.

Table 4: Log Sheet for Conventional Core Samples from Umiat Well 11

Side label #	1	2	3		5	6		8
Core #	40	49	53	59	39	47	56	60
Length (cm)	9.86	10.89	13.49	10.23	9.34	11.41	8.18	9.86
Depth (ft)	2133	2381	2455	2933	2124	2299	2819	2993
Appearance	C,F	S	S	C	C	C	F,S	S
$K1_{air}$(md)	77	97		69	195		134	73
$K2_{air}$(md)	62			68	238		245	66
$K3_{air}$(md)	65			69	188		130	99
$K4_{air}$(md)	68	98		70	93		140	72
$K5_{air}$(md)	94			71	123		145	
$K6_{air}$(md)	69			72	85			
$K7_{air}$(md)	73	111	131	84	83	142	147	80
$K8_{air}$(md)	83	134	107	85	86	151	886	92
$K9_{air}$(md)	284	118	110	98	90	122	151	93
$K10_{air}$(md)	85	90	115	83	88	130	139	87
$K11_{air}$(md)	92	105	105	82	84	144	127	86
$K12_{air}$(md)	102	102	112	96	84	118	114	87
$K13_{air}$(md)	79			86	86	118		
$K14_{air}$(md)	92			80	85	112		
$K15_{air}$(md)	84			88	86	140		

F=Fractured, S=Slabbed, C=Cylindrical.

Figure 18: Picture of Drill Bit Used in Drilling Core Plugs

Figure 19: Picture of Core Plugs

3.5 **Test Fluids**

Three different formation water samples were prepared according to the water composition data from Umiat well #11 which are presented in Table 5.

Table 5: Water Analyses from Umiat Well 11 (Collins, F.R., 1958)

Water compositions (ppm)	Test 8 2375-2411 feet	Test 9 2447-2461 feet	Test 11 2832-2850 feet
Barium	**-**	**1**	**-**
Calcium	**30**	**8**	**14**
Magnesium	**9**	**3**	**4**
Sodium	**2190**	**2030**	**2190**
Carbonate	**96**	**390**	**126**
Bicarbonate	**2960**	**3120**	**2240**
Sulfate	**21**	**28**	**19**
Chloride	**1600**	**865**	**1950**
Total solids	**6906**	**6434**	**6543**
Specific gravity at 60^0F	**1.004**	**1.003**	**1.003**

Based on these data, water composition from Test 8 was used for the core plugs drilled from the cores 40, 49, 39, and 47, while the water compositions from Test 9 and Test 11 were used for core plugs cut from the cores 53 and 60 respectively. Upon preparation, water samples were filtered in order to avoid clogging of the core plugs while conducting the flow experiments on them.

Density and viscosity were measured for all the test fluids using an Anton-Paar densitometer (DMA-4500) and viscometer (AMVn). The measuring cell of the densitometer consists of a U-tube which is oscillated at its fundamental frequency. This

frequency is a function of the system mass and therefore it is a function of test fluid density. The density measurement procedure is very simple and it involves the following steps:

- Inject the test fluid into the cleaned and dried measuring cell through the injection port.
- Adjust the desired temperature on the densitometer and wait for the reading of density value measured at atmospheric pressure.

The Anton-Paar viscometer consists of an inclined cylindrical tube, within which is a solid sphere. The tube is filled with test fluid and the ball starts to roll under the influence of gravity. Assuming the density of the fluid is known, the travel time of the solid sphere is a function of fluid viscosity. The following steps need to be performed to measure the viscosity:

- Select the capillary tube based on the viscosity range it can measure.
- Fill the tube with test fluid and check the mobility of the solid sphere in it.
- Place the tube in the capillary block.
- Set the desired temperature, input density and wait for the reading of test fluid viscosity measured at atmospheric pressure.

Anton-Paar viscometer and densitometer are shown on Figure 20.

Figure 20: Anton-Paar Viscometer (left) and Densitometer (right)

Test fluids 8, 9 and 11 were prepared in amounts of 12, 6 and 6 liters respectively. Table 6 represents measured density and viscosity data together with all the applied salts for each water sample.

Table 6: Properties of Water Samples and Amount of Applied Salts

Used salts	**Test 8 g/12L**	**Test 9 g/6L**	**Test 11 g/6L**
Calcium chloride $CaCl_2$	0.66	0.11	0
Sodium sulfate Na_2SO_4	0.37	0.25	0.17
Sodium bicarbonate $NaHCO_3$	48.90	25.78	18.51
Sodium chloride NaCl	30.6	8.4	19.2
Magnesium chloride $MgCl_2$	0.41	0.07	0.06
Calcium carbonate $CaCO_3$	0.31	0.02	0.21
Sodium carbonate Na_2CO_3	1.7	4.11	1.08
Magnesium carbonate $MgCO_3$	0.01	0.003	0.024
Barium carbonate $BaCO_3$	0	0.009	0
Freezing point ^0C	-5	-4	-3
Density at 22^{0}C g/cm^3	1.003	1.002	1.002
Viscosity at 22^{0}C cp	1.157	1.15	1.15

Freezing point for each water sample was determined by placing it at 0^0C inside the chamber and subsequently reducing the temperature by 1^0C until the sample froze. Presented values are rough estimates with an accuracy of $\pm 1^0C$.

Given the fact that kerosene has very low freezing point, about -30^0C, it was used as an oil phase throughout the experiments. Density and viscosity for kerosene was measured using the same apparatus as for the water samples. Obtained values are presented in table 7.

Table 7: Properties of Kerosene

Density at 22^0C g/cm^3	0.78
Viscosity at 22^0C cp	1.15
Viscosity at -22^0C cp	1.78

3.6 Experimental Conditions

As discussed in previous chapters, one of the parameters affecting the unfrozen water content inside the core plug is the temperature of the core. Due to the relation between these two values, it is of great importance to control/monitor the temperature of the core while conducting the experiments in simulated permafrost conditions. Because of the operational principles of the freezing chamber, i.e., cycling above and below the set point, it is impossible to maintain a constant air temperature inside the airbath. In order to monitor the temperature fluctuation, thermocouples were placed inside the chamber and it was observed that after reaching the equilibrium state, the air temperature inside the freezer fluctuates with a value of $\pm 1.6^0$C around the desired -10^0C. It was thought that this would result in temperature variation of the core plug, which we wanted to ascertain. However, measuring the temperature of the core plug was impossible due to inaccessibility as the core sample is placed inside a core holder. Therefore, it was decided to at least monitor the core holder surface temperature. An infrared camera, FLIR Systems ThermaCAM^{TM} P40, was used for this purpose. The camera measures and images the infrared radiation emitted by an object. Figure 21 shows one of the images together with the associated temperature scale recorded while measuring the core holder surface temperature. The enclosed software, ThermaCAM^{TM} Researcher Basic Ver. 2.7, also provides the exact value of a surface temperature from any chosen reference point at the picture.

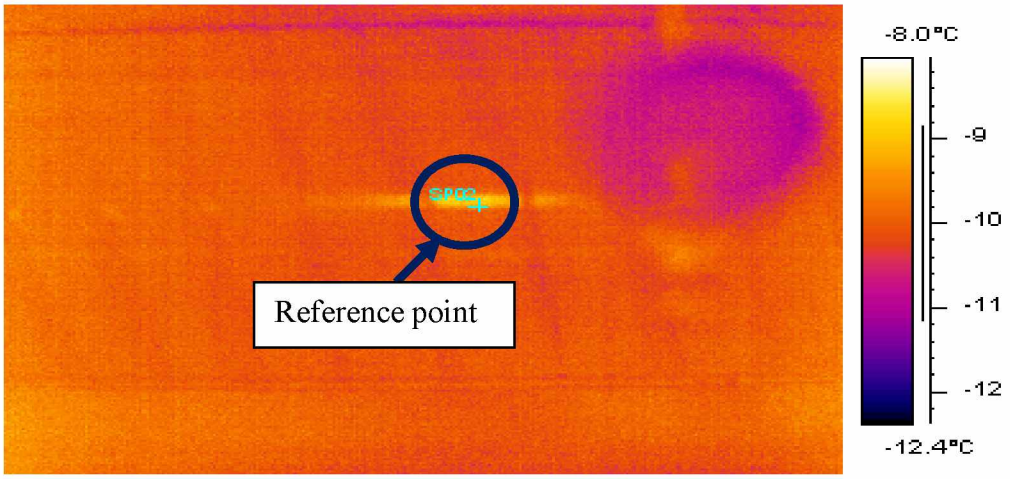

Figure 21: Image of the Infrared Radiation from the Surface of the Coreholder

Radiation is a function of object surface temperature, which makes it possible for the camera to calculate this temperature (ThermaCAMTM Researcher User's manual, 2003). In order to reduce reflection and simulate ideal thermal radiation, consequently increasing the accuracy of obtained temperature data, the surface of the coreholder was covered with black duct tape. Figure 22 shows the coreholder surface temperature at the reference point versus time before and after the equilibrium state.

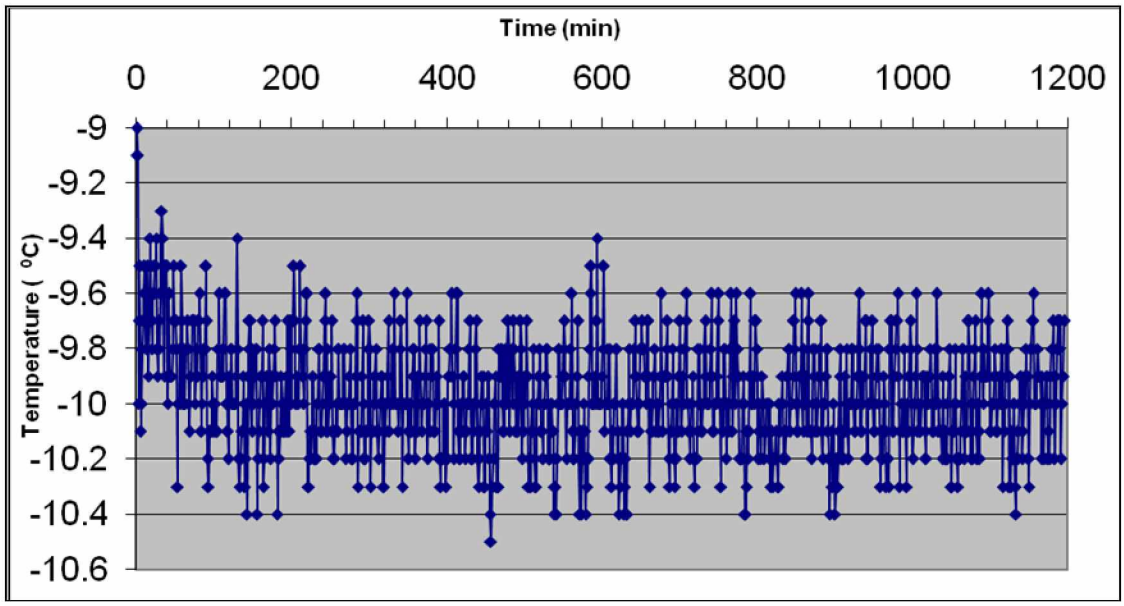

Figure 22: Coreholder Surface Temperature versus Time

Figure 22 indicates that the majority of the temperature fluctuation actually occurs between $\pm 0.2^0$C and $\pm 0.3^0$C, whereas only a handful of fluctuations occur within $\pm 0.4^0$C. Obviously, if the core holder surface temperature variation is between $\pm 0.2^0$C and $\pm 0.3^0$C then the actual core temperature fluctuation could be even less than that, which gives the confidence of an almost constant temperature throughout the low-temperature flow experiments.

Chapter 4 Results and Discussion

This chapter presents the relative permeability determination results for six Umiat core plugs as well as for the Berea sandstone that also was used as a test case in order to test the experimental set-up prior to analyzing the actual Umiat cores. The experiments on Berea SS were carried out at 22^0C and -7^0C.

4.1 Routine and Special Core Analysis and Subsequent Results

This section presents the results obtained in this study on routine (porosity, absolute permeability, irreducible water saturation) and special (relative permeability, capillary pressure) core analysis of the tested Umiat and a Berea SS cores. These results are discussed in the subsequent section 4.2.

Procedure:

Porosities of all the core samples were obtained by the vacuum saturation method, which is followed by single phase flow of brine from which the absolute permeability is determined using Darcy equation. The flow continues until the pressure differential across the core plug gets stabilized and the stabilized ΔP is used in absolute permeability calculations. Following the absolute permeability determination the core is flooded with kerosene until irreducible water saturation is achieved. Again, the stabilized pressure differential is used for calculation of effective permeability to oil at S_{wi} and the information on pore volume and cumulative water produced is used for determination of S_{wi}. A mass balance method is also applied to determine S_{wi} as per the procedures described in previous chapter.

In the subsequent step gas injection is commenced and data on pore volume of oil produced is collected. Figure 23 and 24 shows pore volume of oil produced vs. time for core 40 at 22^0C and -10^0C respectively.

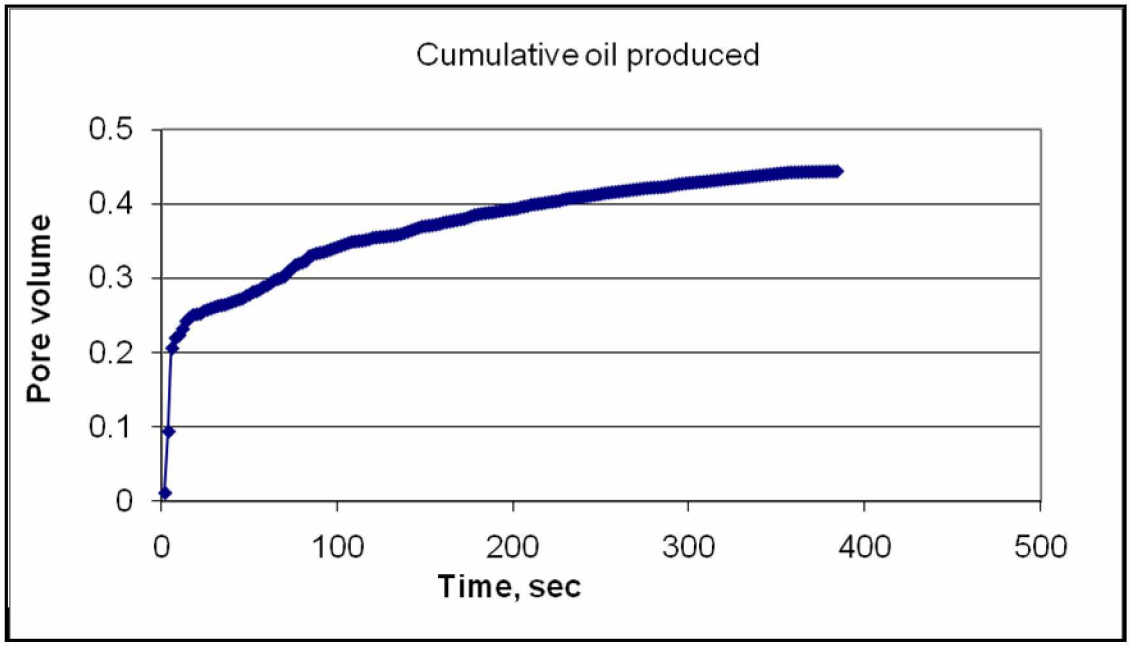

Figure 23: Cumulative Oil Produced for Core 40 versus Time at 22^{0}C

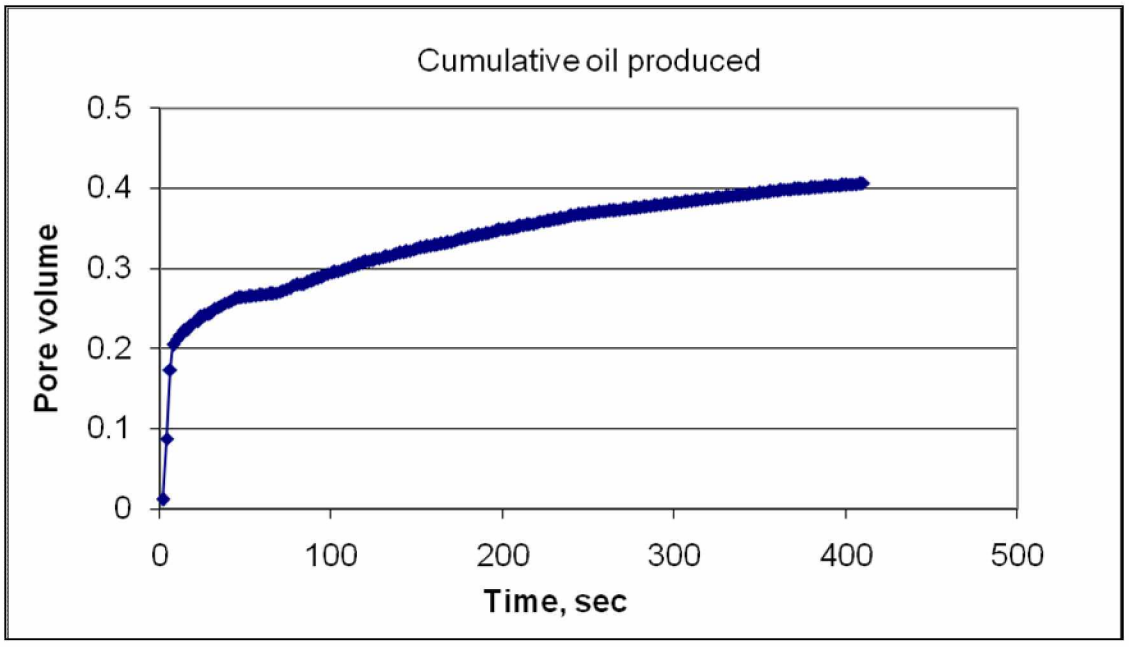

Figure 24: Cumulative Oil Produced for Core 40 versus Time at -10^{0}C

For each core sample an Excel spreadsheet was prepared in order to process the data obtained in step 8 of core flooding experimental procedures (section 3.2) according to JBN method (see Figure 25.) During the gas injection process all the recorded data for each time step, such as cumulative oil production, cumulative gas injected and pressure drop across the sample, are input for columns "A" through "I". Columns "J" through "T" represent the JBN method applied to data given in preceding columns. All the derivatives required to calculate the relative gas and oil permeabilities as well as gas saturation (see formulae A37, A38 and A44) are calculated using the numerical forward differentiation formulae. The final values of oil and gas relative permeabilities are calculated in columns "R" and "S" respectively. These values are determined at different total liquid saturations, column "T", which is the sum of irreducible water and oil saturations. An example of relative permeability calculation is presented in Appendix C.

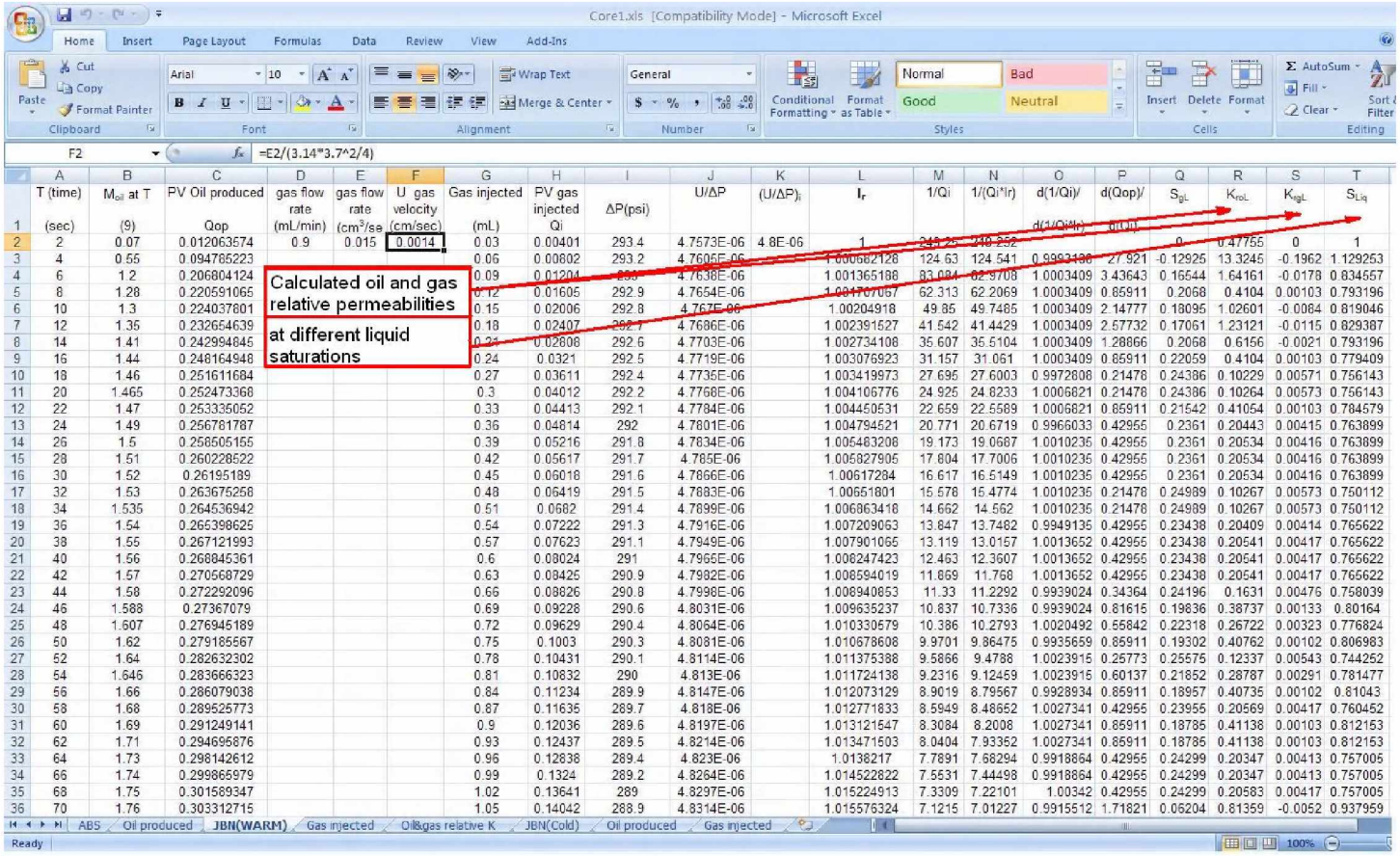

Figure 25: Relative Permeability Calculations in Excel Spreadsheet

Results:

The results from routine core analysis are presented in Table 8 which compares the data obtained in this work with the one reported by Baptist (1960) for Well 11. As we see the table shows fairly good match.

Calculated gas-oil relative permeabilities for core 40 are given in Table 9 at both room temperature (K_{ro} and K_{rg}) and freezing conditions (K_{ro}(ice) and K_{rg}(ice)). Depending on experimental conditions these values are given at different liquid saturations (S_{Liq}) because the total liquid saturation at any time step depends on gas injection flow rate as well as on phase status of irreducible water.

Oil and gas relative permeabilities at 22^0C and at -10^0C for core 40 are graphically presented in Figures 26 and 27. For the rest of the core samples the relative permeability data and the corresponding curves are given in Appendix B.

Table 8: Properties of Core Samples Used in Experiments

Core #		40	49	53	39	47	60	Berea SS
Depth (ft)		2133	2381	2455	2124	2299	2993	
Length of core plug (cm)		5.5	4.15	3.4	5.35	4.2	3.15	15.2
Depth range for Baptist data (ft)		2130-2140	2375-2385	No data	2120-2130	2295-2310	No data	
This work ϕ (%)		12.65	16.1	14.75	12.83	17.23	12.97	15.24
Baptist ϕ (%)		11.1-14.7	14.2-23.3	No data	12.4-14.7	13.6-19	No data	
This work K_{abs}(md)		0.932	4.005	0.664	0.451	27.7	0.408	46.85
Baptist K_{abs}(md)		<0.5-6.2	0-2.6	No data	2.6-6.2	<0.5-75	No data	
This work S_{wi}(%)	Mass balance	41.1	41.7	42.5	34.3	43.4	39.5	60.9
	Volumetric	39.8	37.3	38.8	32.2	42.1	36.2	49.2
Baptist S_{wi}(%)		No data	26-50	No data	? to32	15-49	No data	

Table 9: Oil and Gas Relative Permeabilities for Core 40

S_{Liq}(%)	K_{ro}	K_{ro}(ice)		S_{Liq}(%)	K_{rg}	K_{rg}(ice)
100.00	478×10^{-3}	290×10^{-3}		100.00	0	0
80.16	387×10^{-3}			80.16	133×10^{-5}	
78.97		234×10^{-3}		78.97		508×10^{-6}
78.15	288×10^{-3}			78.15	291×10^{-5}	
74.67	206×10^{-3}			74.67	418×10^{-5}	
73.98		117×10^{-3}		73.98		156×10^{-5}
72.03		939×10^{-4}		72.03		178×10^{-5}
70.10		705×10^{-4}		70.10		199×10^{-5}
69.32	101×10^{-3}			69.32	564×10^{-5}	
68.14		572×10^{-4}		68.14		204×10^{-5}
67.50	833×10^{-4}			67.50	613×10^{-5}	
66.46		457×10^{-4}		66.46		214×10^{-5}
62.53	402×10^{-4}			62.53	653×10^{-5}	
58.74	213×10^{-4}			58.74	725×10^{-5}	
57.17	100×10^{-4}			57.17	742×10^{-5}	

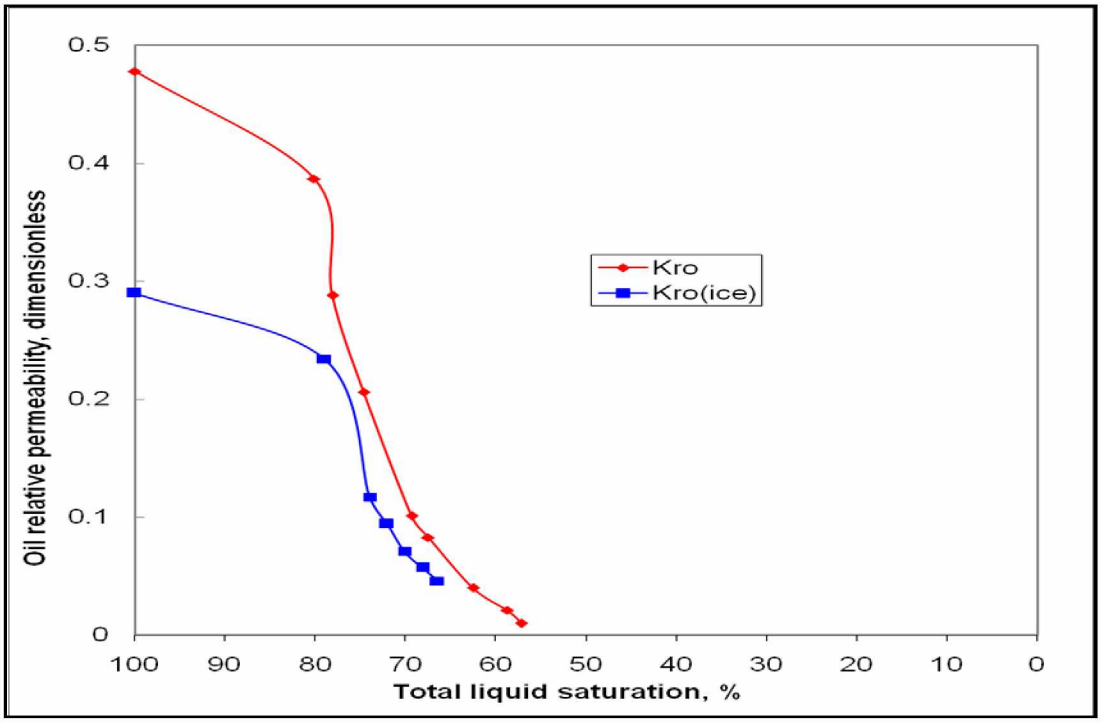

Figure 26 Oil Relative Permeabilities at 22^{0}C (red) and -10^{0}C (blue) for Umiat Core 40

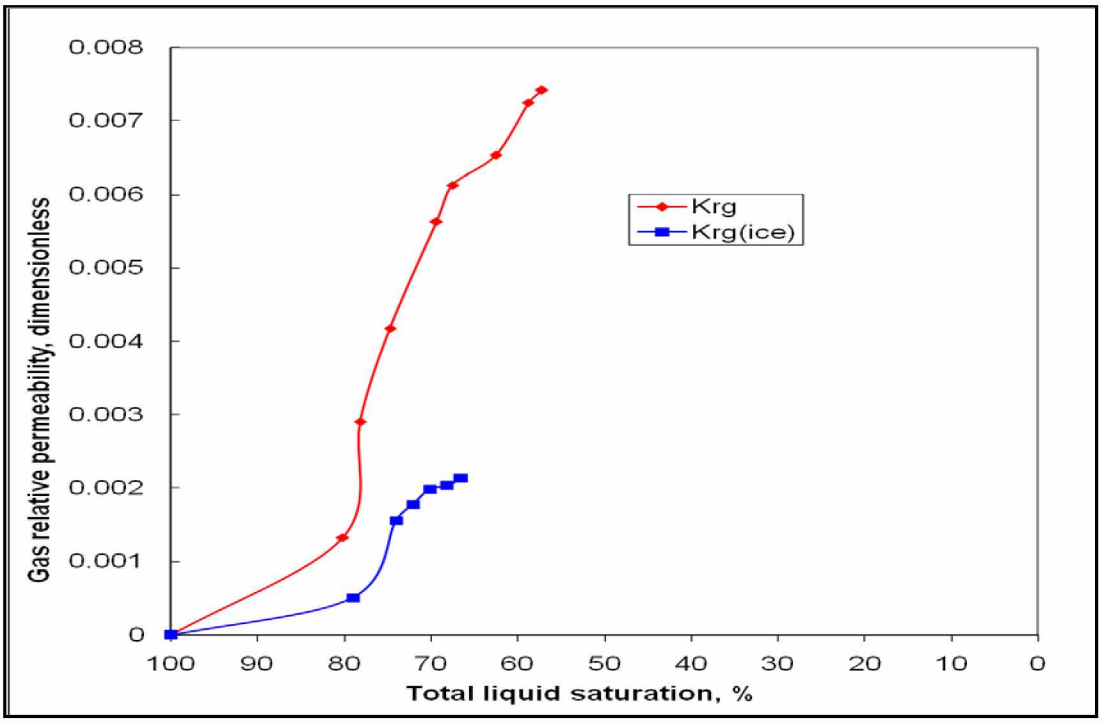

Figure 27 Gas Relative Permeabilities at 22^{0}C (red) and -10^{0}C (blue) for Umiat Core 40

4.2 **Potential Sources of Error**

While conducting the experiments, it was observed that the main measurement errors are encountered in step 8 of core flooding experimental procedures (section 3.2). For example it was observed that the mass of the glass accumulator, which measures the cumulative oil production, remained the same or even decreased for two successive time steps. Evidently this is an unrealistic situation because the JBN method implies the continuous production of oil and therefore the mass of the glass accumulator has to be strictly increasing as a function of time until there is no more oil production, which is the end point of the gas injection procedure. For all such values of cumulative oil production the average of preceding and succeeding values was taken in order to smooth the oil production data. There are at least two reasons that caused these types of problems, and unfortunately it was practically impossible to eliminate any of them. First of all, the devices used in this experiment, including the electronic scale, have their own readability errors, and secondly, the produced oil is detected by the scale only after the drop of produced oil falls into the glass accumulator and not while it is hanging at the end of the production tubing.

4.3 **Capillary Pressure Measurements and Results**

Procedure:

Following the relative permeability tests, three Umiat core plugs (53, 47 and 60) were selected for capillary pressure measurements. Prior to conducting mercury injection capillary pressure measurements, all cores were cleaned and dried. The procedure described in the previous chapter was followed to obtain the capillary pressure data.

Results:

All of the obtained capillary pressure data are represented in the Tables 10-12 and Figures 28-30, where S_g denotes the air saturation inside the core plug and P_{cwk}, P_{cam}, and P_{cka} stand for capillary pressure values for water-kerosene, air-mercury and kerosene-air systems, respectively. In an air-mercury system air represents the wetting phase; i.e. all the capillary pressure data is for drainage.

Table 10: Capillary Pressure Data for Umiat Core 53

S_g (%)	P_{cam} (psia)	P_{cwk} (psia)	P_{cka} (psia)
100.00	15	1.48	0.83
95.99	29	2.86	1.61
92.67	37	3.65	2.05
70.50	50	4.93	2.77
46.91	80	7.89	4.44
35.11	155	15.28	8.59
28.02	241	23.75	13.36
20.37	519	51.15	28.77
15.79	1110	109.40	61.54
13.43	1673	164.90	92.75

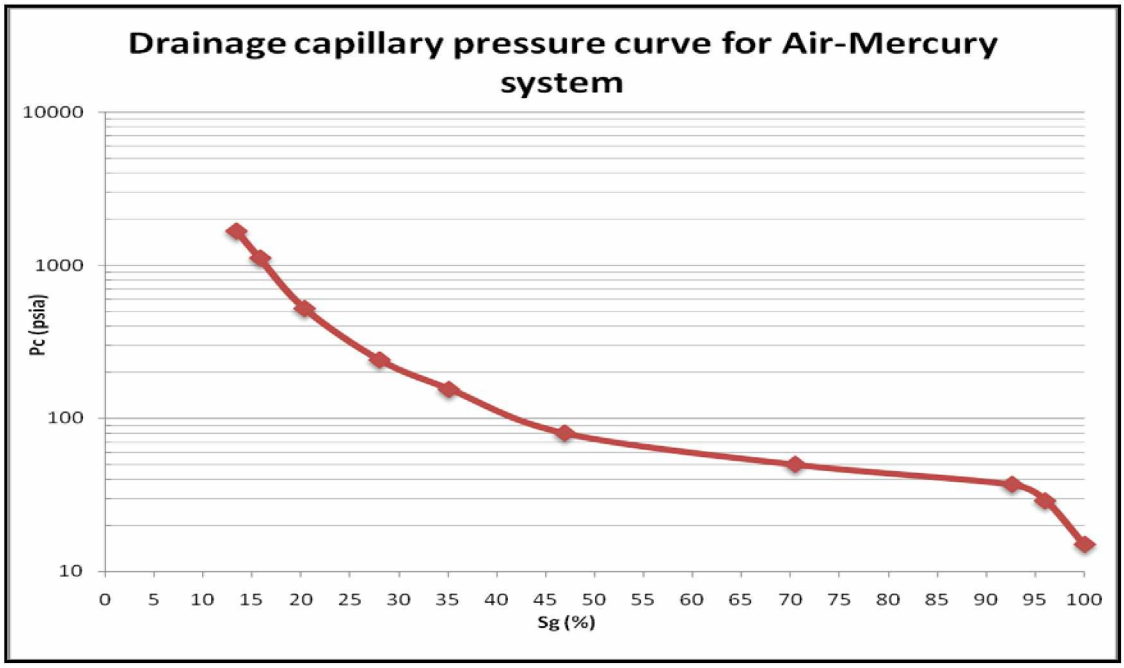

Figure 28: Drainage Capillary Pressure Curve for Air-Mercury System for Umiat Core 53

Table 11: Capillary Pressure Data for Umiat Core 47

S_g (%)	P_{cam} (psia)	P_{cwk} (psia)	P_{cka} (psia)
100	15	1.48	0.83
99.90	22	2.17	1.22
99.42	27	2.66	1.50
78.28	34	3.35	1.89
55.68	49	4.83	2.72
45.48	67	6.60	3.71
41.55	81	7.98	4.49
33.91	157	15.47	8.70
27.48	261	25.72	14.47
21.72	549	54.11	30.44
18.68	945	93.14	52.39
16.00	1516	149.42	84.05

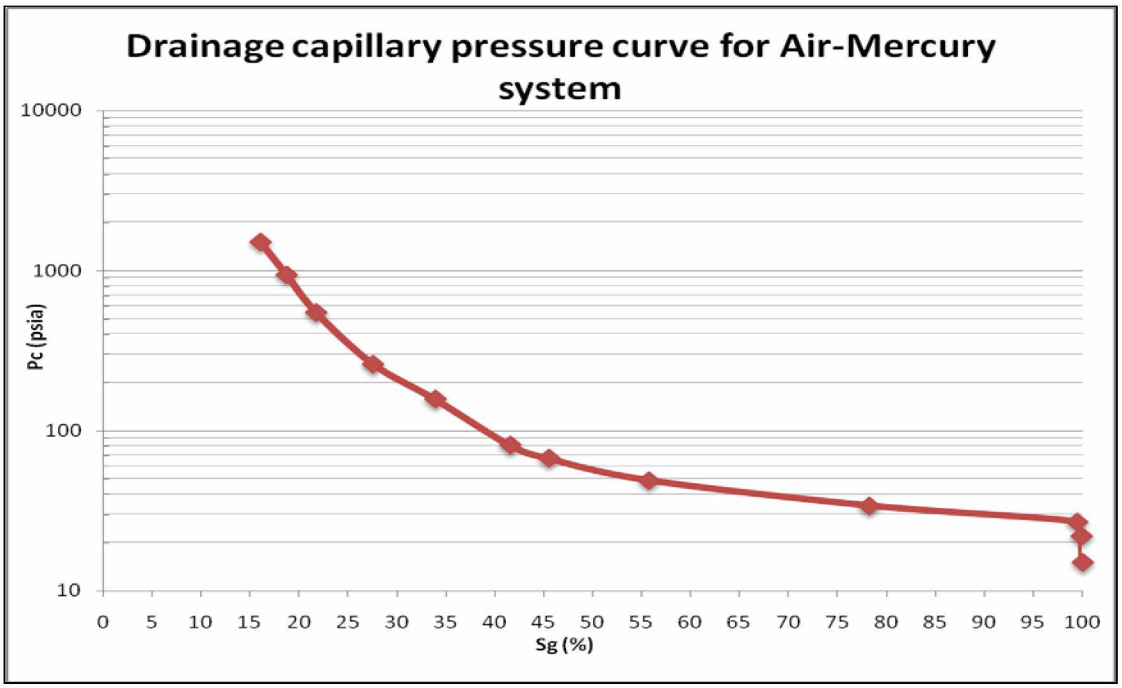

Figure 29: Drainage Capillary Pressure Curve for Air-Mercury System for Umiat Core 47

Table 12: Capillary Pressure Data for Umiat Core 60

S_g (%)	P_{cam} (psia)	P_{cwk} (psia)	P_{cka} (psia)
100	15	1.48	0.83
99.04	37	3.65	2.05
95.10	102	10.05	5.66
78.87	215	21.19	11.92
61.81	371	36.57	20.57
54.11	528	52.04	29.27
42.45	977	96.30	54.17
37.28	1410	138.97	78.17
34.68	1763	173.77	97.74

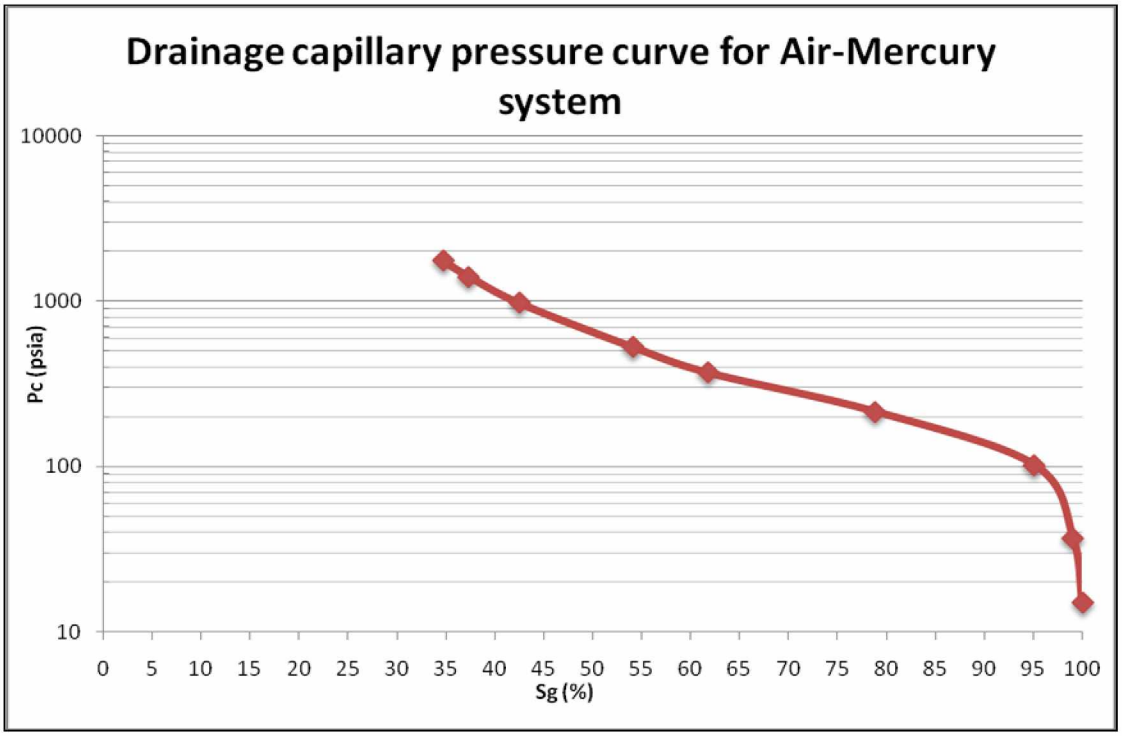

Figure 30: Drainage Capillary Pressure Curve for Air-Mercury System for Umiat Core 60

4.4 **Discussion**

The results of the core flooding experiments exhibit the reduction of oil relative permeability at irreducible water saturation (which is same as oil relative permeability at 100% total liquid saturation, see Figure 26) for all six Umiat core plugs as well as for the Berea sandstone caused by freezing of connate water. (See table 13). For Umiat cores this decrease varies in the range of 39.3%-91.5% with an average decline of 60.97%, which is significantly higher than the average 27% reduction obtained by the Federal Bureau of Mines. (Baptist, 1960) So the average decline of relative oil permeability at irreducible water saturation has increased more than two times by changing temperature from 26^0F (-3.3^0C) to -10^0C.

Table 13: Reduction in Oil Relative Permeability at S_{wi}

Core #	K_{ro}	K_{ro}(ice)	Reduction in K_{ro}, %
40	478×10^{-3}	290×10^{-3}	39.3
49	622×10^{-3}	128×10^{-3}	79.4 [1st run] 62.0 [2nd run]
53	453×10^{-3}	196×10^{-3}	56.7
39	714×10^{-3}	335×10^{-3}	53.1
47	568×10^{-3}	480×10^{-4}	91.5 [1st run] 83.8 [2nd run]
60	450×10^{-3}	244×10^{-3}	45.8
Berea SS	855×10^{-3}	534×10^{-3}	37.5

Figure 31 represents the relationship between the freezing temperature and oil relative permeability reduction based on the results obtained in this work and Baptist (1960).

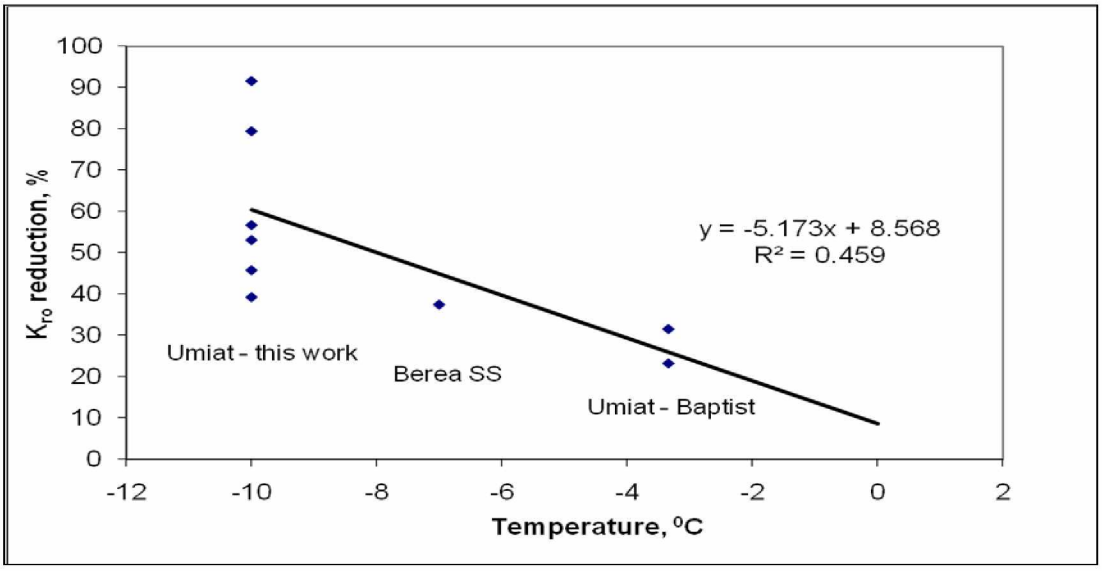

Figure 31: Relationship between the Freezing Temperature and Oil Relative Permeability Reduction

Figure 32 shows the relationship between the absolute permeability and oil relative permeability reduction for Umiat cores and Berea SS core studied in this work.

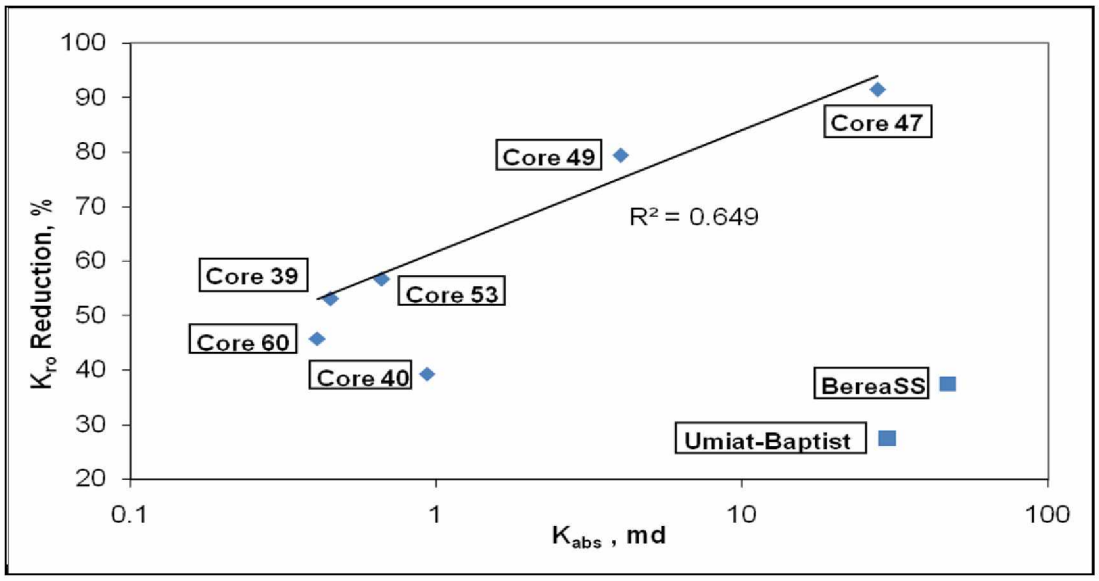

Figure 32: Relationship between the Absolute Permeability and Oil Relative Permeability Reduction

As seen in the plot, the data does show some scatter and indicates a weak correlation between reduction in K_{ro} and absolute permeability. However, excluding the data points on Berea SS, Baptist's core and core 40, the correlation is somewhat stronger and shows

increasing reduction in effective oil relative permeability with increasing absolute permeability. Hypothetically, the core plugs with higher permeabilities most likely have larger pores and pore-throats which results in smaller water-to-ice ratios (Smith and Low, 1996). Therefore, at the same temperature the core plug with higher permeability will have lower unfrozen water content and the reduction of oil relative permeability will be greater. However, this needs to be verified by core imaging techniques.

Figure 33 represents the relationship between the irreducible water saturation and oil relative permeability reduction.

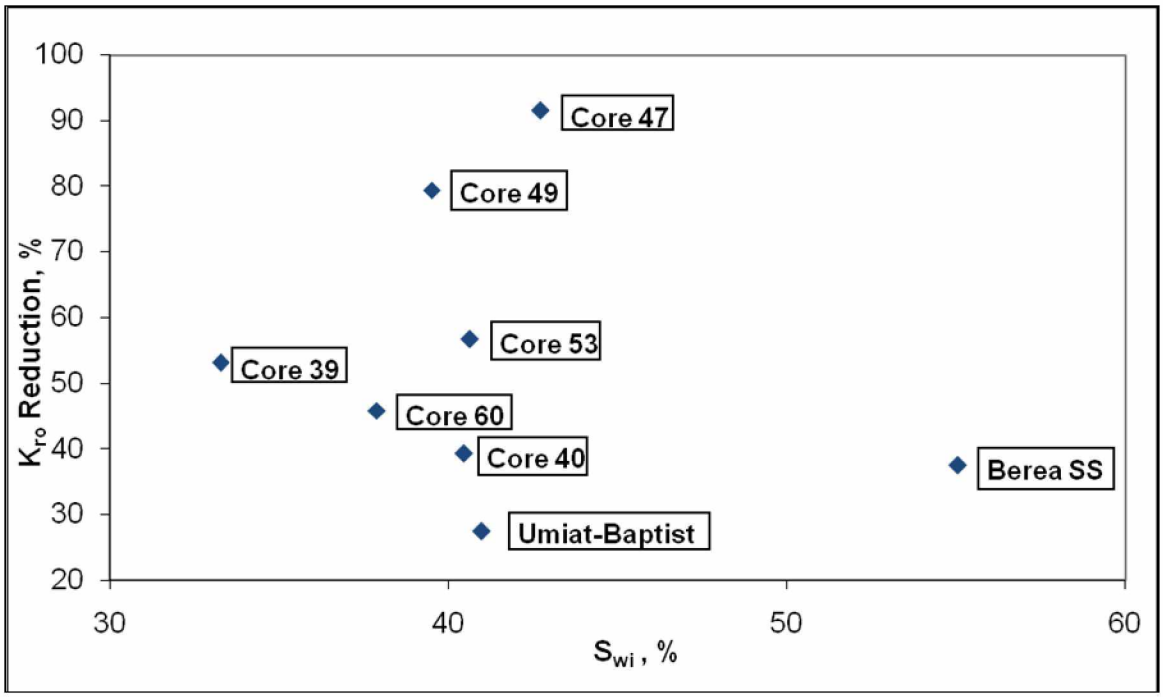

Figure 33: Relationship between the Irreducible Water Saturation and Oil Relative Permeability Reduction

As seen in the plot, the data shows significant scatter. As a matter of fact Baptist appropriately commented on this based on just two tested core samples, noting that freezing results in about 9% volume expansion thus correspondingly increasing the S_{wi}. This increased S_{wi} then results in additional constriction of connections between the pore spaces, in a way "cementing" them, which causes a dramatic reduction in K_{ro} (Baptist,

1960). However, the effect of S_{wi} on reduction in K_{ro} should not be considered in isolation but together with other key rock properties such as porosity and absolute permeability.

Commonly used analytical representations for individual phase relative permeabilities are expressed by the following functional forms: (Tarek, 2001).

$$K_{ro} = (K_{ro})_{S_{gc}} \times \left(\frac{S_{Liq} - S_{wi} - S_{or}}{1 - S_{gc} - S_{wi} - S_{or}} \right)^{N_o} \qquad (16)$$

$$K_{rg} = (K_{rg})_{S_{wi}} \times \left(\frac{1 - S_{Liq} - S_{gc}}{1 - S_{gc} - S_{wi} - S_{or}} \right)^{N_g} \qquad (17)$$

Where S_{gc} and S_{or} represent critical gas and oil residual saturations respectively. Using the experimentally obtained data from Table 9, Corey exponents N_o and N_g can be determined by means of plotting relative permeability data versus normalized saturations on a log-log scale and calculating the slope of the trend. Figure 34 and figure 35 show a plot of relative oil and gas permeabilities at freezing conditions versus normalized saturations for Umiat core 40.

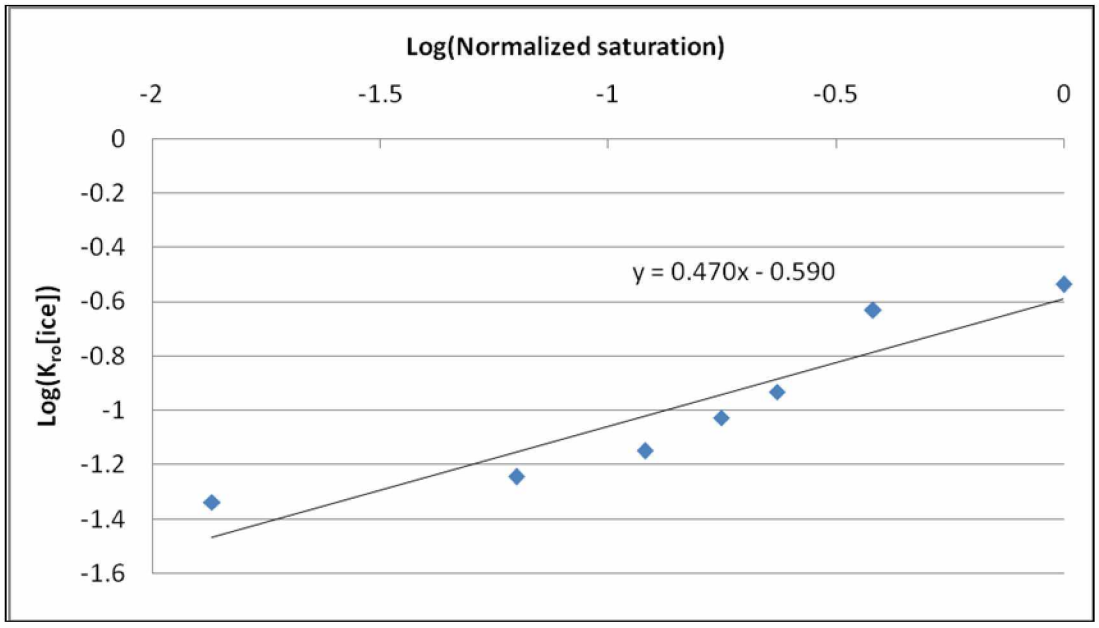

Figure 34: Relative Oil Permeability versus Normalized Saturation for Umiat Core 40

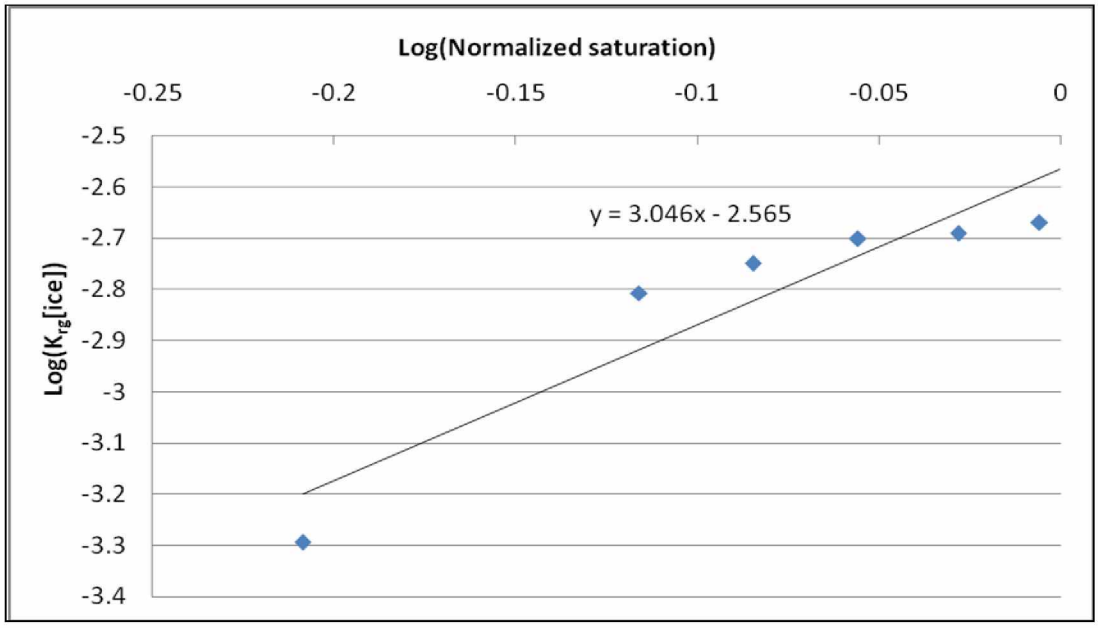

Figure 35: Relative Gas Permeability versus Normalized Saturation for Umiat Core 40

Figure 36 and figure 37 show experimentally-obtained oil and gas relative permeability data at -10^0C for core 40 as well as their analytical representations using the calculated Corey exponents of N_o=0.47 and N_g=3.05.

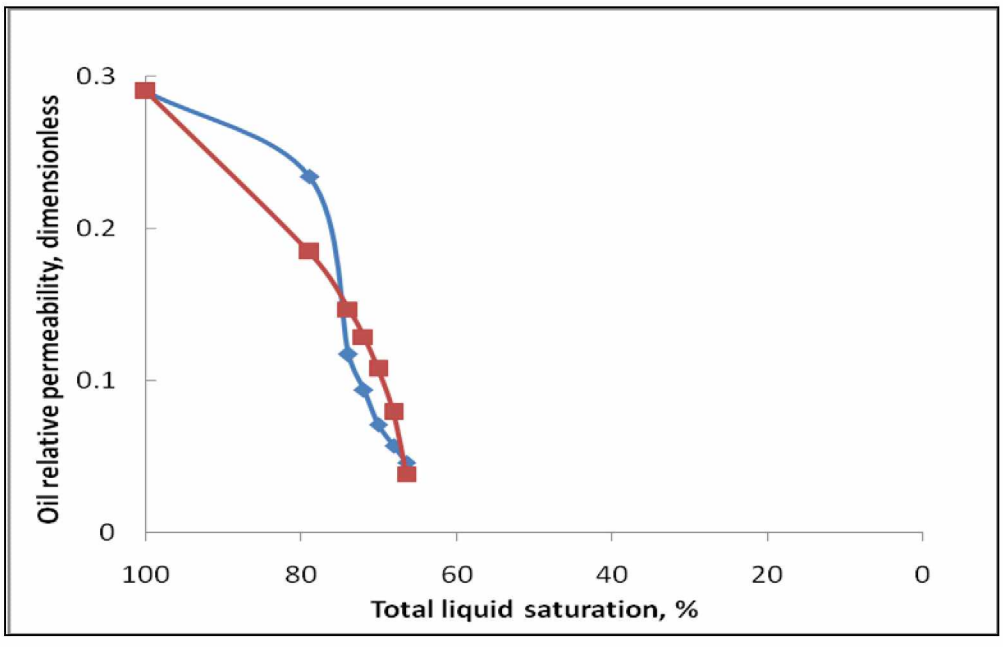

Figure 36: Experimentally-Obtained Oil Relative Permeability Data (blue) and its Analytical Representation (red) for Umiat Core 40

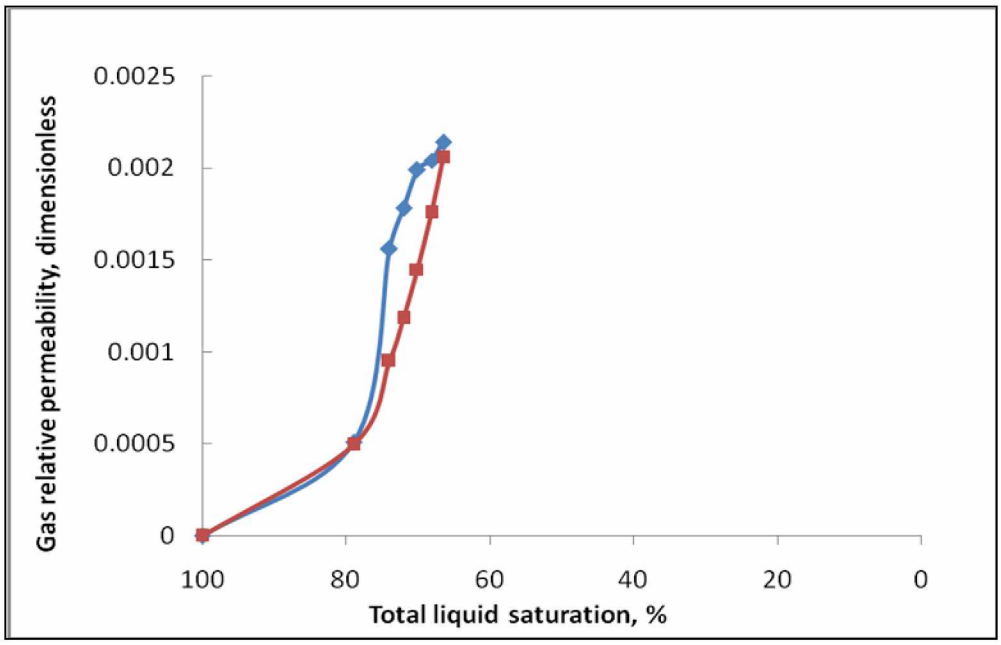

Figure 37: Experimentally-Obtained Gas Relative Permeability Data (blue) and its Analytical Representation (red) for Umiat Core 40

As seen from the Figures 36-37, experimentally-obtained data are fairly well approximated by the analytically derived data using Corey exponents. Table 14 presents the Corey exponents for all Umiat cores. Calculation of the exponents can be found in Appendix D.

Table 14: Corey Exponents for Umiat Cores

Core #	N_o	N_g
40	0.47	3.05
49	1.66	0.23
53	0.73	1.54
39	1.06	1.98
47	2.02	0.10
60	0.54	1.97

Pore size distribution in Umiat core plugs can be characterized based on the capillary pressure data that has been obtained. Conventionally, capillary pressure curves can be divided into three parts (Dandekar, 2006). The first part, which represents the capillary

pressure values for high saturation of wetting phase, corresponds to the relatively large pores. Initially, when we apply the small pressure, only these large pores are invaded by mercury. As the applied pressure is subsequently increased, mercury starts to encroach on the medium-size pores and the corresponding values of capillary pressures are represented by the middle segment of the capillary pressure curves. Further increase of applied pressure leads to intrusion in small pores by mercury and the third part of the capillary pressure curve corresponds to these lower values of wetting phase saturation.

Keeping in mind the fact that at every step when we increase the applied pressure the incremental volume of injected mercury is proportional to the number of pores with a radius of

$$r = \frac{2 \times \sigma_{am} \times \cos \vartheta_{am}}{P_{cam}} \quad (18)$$

where σ_{am} stands for the surface tension between air and mercury, P_{cam} is the applied pressure and ϑ_{am} =140^0 (Dandekar, 2006) is the contact angle between air and mercury, we can find the fraction (percentage) of total pore volume that consists of pores having that radius. These pore aperture radii versus fractional saturation distributions for all tested cores are shown in figures 38, 39, and 40.

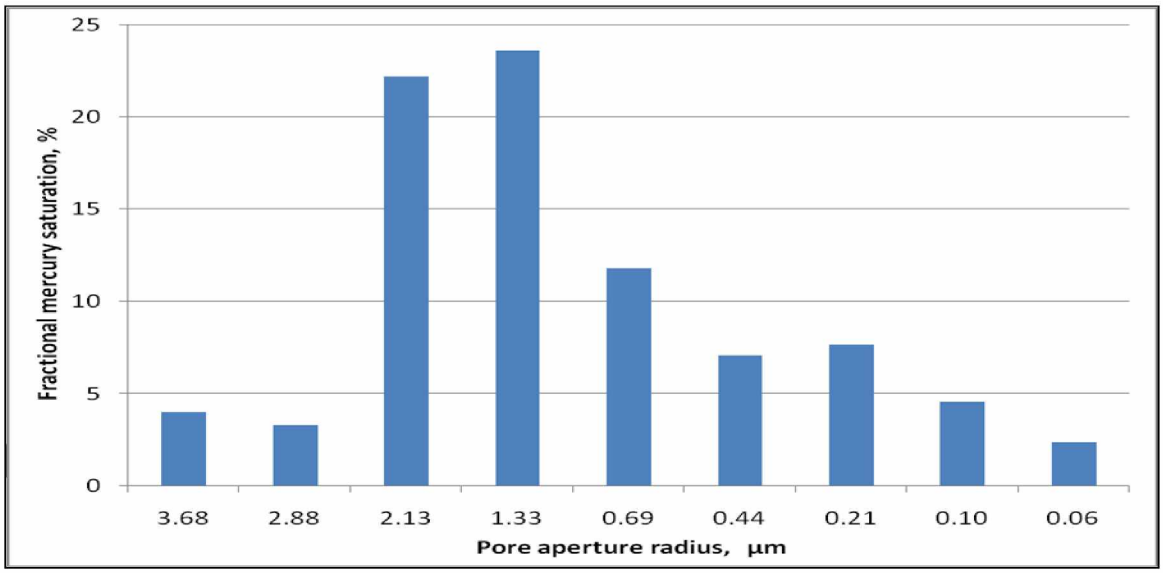

Figure 38: Pore Size Distribution for Umiat Core 53

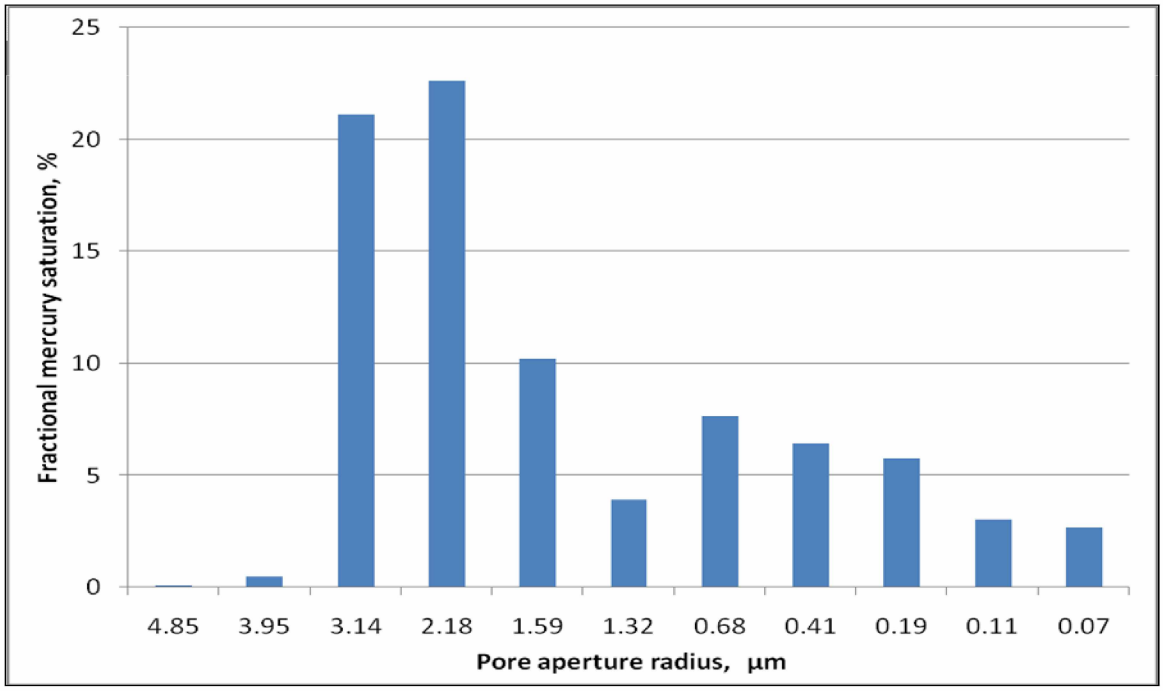

Figure 39: Pore Size Distribution for Umiat Core 47

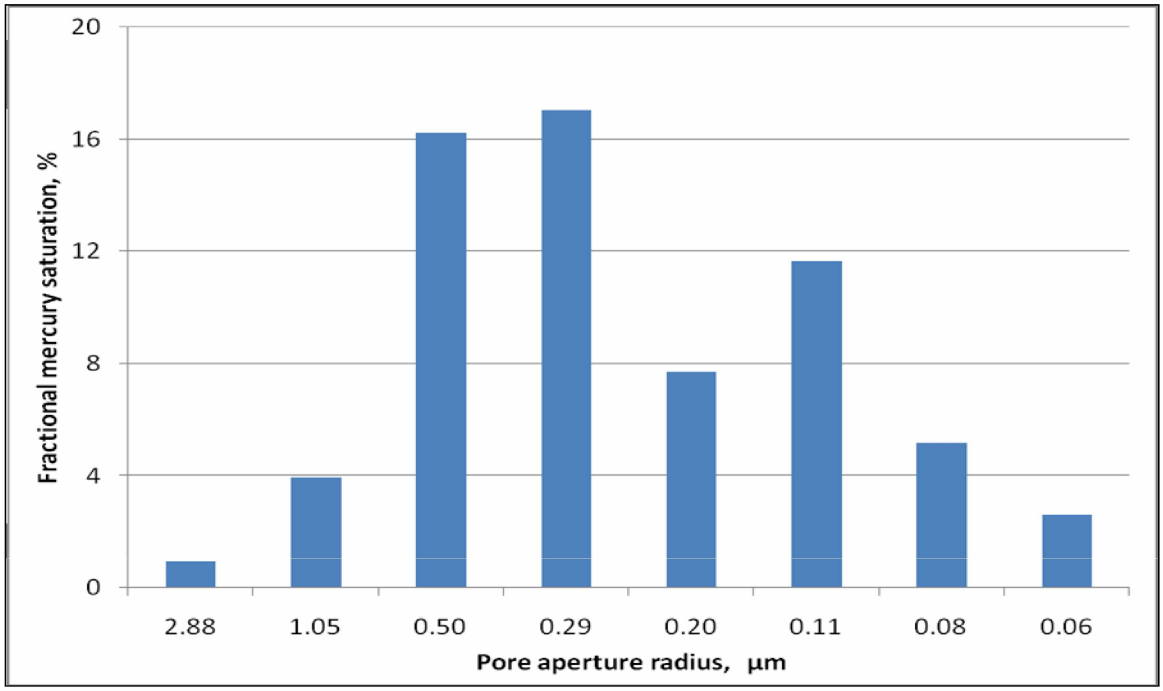

Figure 40: Pore Size Distribution for Umiat Core 60

As seen from these figures, in all three core plugs a significant portion of total pore volume consists of medium-size pores, about 58% for core 53 with radius range of 0.69-2.13μm, 54% for core 47 with radius range of 1.59-3.14μm and 40% for core 60 with radius range of 0.2-0.5 μm.

Pore throat sorting (PTS) coefficient can be used to determine whether the Umiat cores are well sorted or poorly sorted:

$$PTS = \sqrt{\frac{3rd\ Quartile\ pressure}{1st\ Quartile\ pressure}} \quad (19)$$

First and third quartile pressures represent the capillary pressures at 25% and 75% saturation of mercury, respectively. Generally, pore throat sorting coefficient ranges from 1.0 for well sorted porous media to 8.0 for poorly sorted pores.

Calculated PTS values for cores 53 and 47 are equal to 2.6 and 3.1, respectively. For core 60 PTS coefficient cannot be computed because the maximum mercury saturation achieved in this core is only 65%. Higher saturations could not be realized due to restrictions of pressure gauge on maximum applicable pressure, 2000psi.

Another approach to characterizing the pore size distribution involves using the pore size distribution index λ, proposed by Brooks and Corey (1964). Based on experimental data, they proposed the following relationship between the drainage capillary pressure and the wetting phase saturation:

$$P_c = P_{ce} \times (S_w^*)^{-1/\lambda} \quad (21)$$

Where P_{ce} is the capillary entry pressure (or in other words this is the minimum pressure required for mercury to invade the large pores) S_w^* is the normalized wetting phase saturation defined as

$$S_w^* = \frac{S_w - S_{wi}}{1 - S_{wi}} \quad (22)$$

Where S_{wi} denotes irreducible wetting phase saturation.

According to this approach a plot of Log (P_c) vs. Log (S_w^*) will be a straight line with -1/ λ slope. Based on the capillary pressure data obtained for Umiat core plugs, these plots have been constructed and the λ values for core 53, 47 and 60 were determined as 0.992, 0.902 and 1.277 respectively. Figure 41 represents the Log (P_{cam}) vs. Log (S_g^*) plot for Umiat core plug 53.

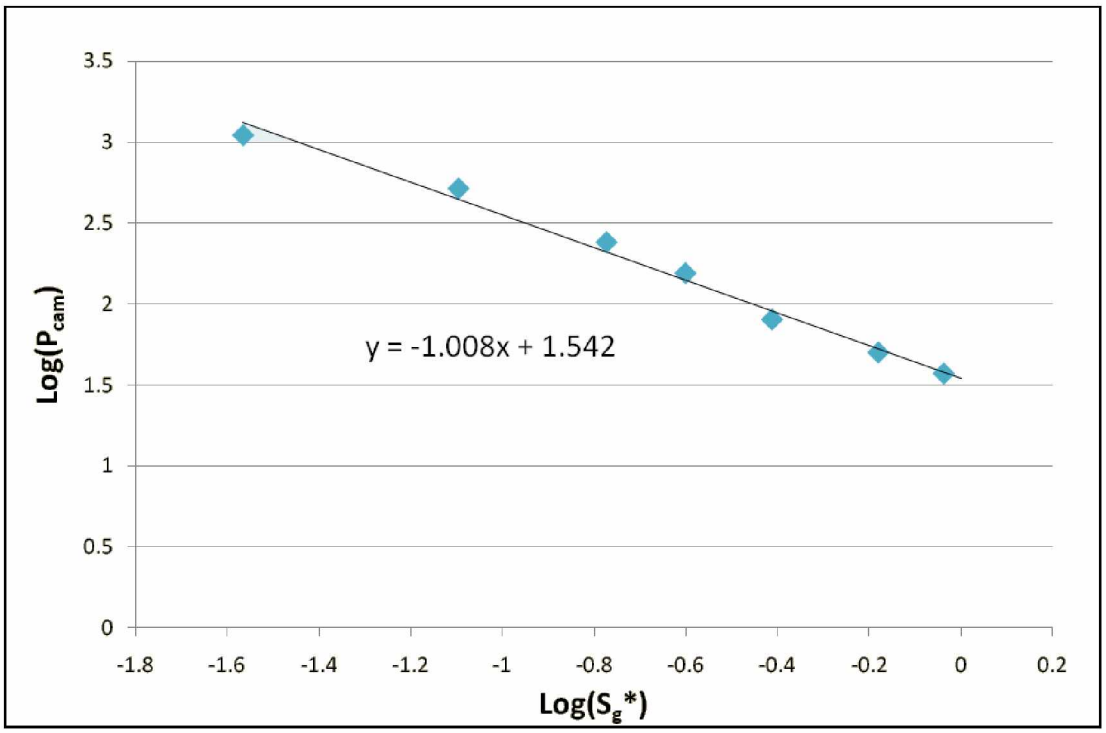

Figure 41: Log (P_{cam}) vs. Log (S_g^*) Plot for Umiat Core 53.

A small value for λ indicates a wide range of pore size, while a large value indicates a narrow range. In other words, a small value for λ indicates the rapid increase of capillary pressure in the third section of the capillary pressure curve, suggesting a significant decrease of pore size below the medium size of pores.

As far as the relation between pore size distribution and oil relative permeability reduction is concerned, obviously the average radius of medium-size pores is very important because, as we saw in all three Umiat core plugs, medium-size pores constitute a high portion of total pore volume, see Figures 38-40. As was discussed in section 1.2, in large pores, (and therefore in core 47 which has the biggest average radius of medium pores,) there is a lower unfrozen water content, which explains the fact that the highest reduction of oil relative permeability occurs in core 47, see Table 13. Using the same logic, the higher reduction of oil relative permeability in core 53 compared to core 60 was quite predictable.

Chapter 5 Conclusions and Recommendations

Experimental study was undertaken on six representative core plugs to investigate two-phase fluid flow properties both at room temperature and at simulated permafrost conditions for Umiat porous media. The experiments were successful in generating gas-oil relative permeability data and the following conclusions and recommendations can be made based on the findings of this work:

Conclusions:

- For all six Umiat core plugs, oil relative permeability declines on an average by 61% as a result of freezing irreducible water at -10^0C.
- The routine core analysis data obtained in this work compares favorably with the one reported by Baptist (Baptist, 1960) for similar Umiat cores.
- Comparison between Baptist's data and the outcomes of this work suggests that lowering the temperature of porous medium significantly below 0^0C results in further reduction of oil relative permeability.
- Data obtained from this experimental study gives insights about the influence of absolute permeability, irreducible water saturation, and pore size distribution on oil relative permeability reduction. Although these correlations are somewhat weak, it can be observed that reduction in oil relative permeability tends to be higher for the core plugs which have the higher absolute permeability, irreducible water saturation or average pore size radius. However, none of these factors should be considered separately; rather they should be considered in combination with others.
- Correy exponents obtained for Umiat cores reproduce the gas and oil relative permeabilities reasonably well.

Recommendations:

- Since the freezing point of used water samples primarily depends at their salinity, there is a need to conduct similar experiments using higher salinity brine and investigate its effect on relative permeability reduction.
- Comparing the obtained relative permeability data with Baptist's data, it was concluded that reduction in oil relative permeability depends on temperature. Hence, it would be reasonable to carry out the experiments at different temperatures recorded in Umiat wells.
- It is recommended NMR experiments be conducted on Umiat cores in order to examine the relationship between the pore size distribution and unfrozen water content at different temperatures.

References

Andersland, O.B. and Ladanyi, B., Frozen ground engineering: The American Society of Civil Engineers & John Wiley & Sons, Inc. [2004].

Anderson, D.M. and Tice, A.R., Predicting unfrozen water contents in frozen soils from surface area measurements: Highw. Res. Rec. 393, p.12-18, [1972].

Baptist, O.C., Oil recovery and formation damage in permafrost, Umiat field, Alaska: [Washington] U.S. Dept. of the Interior, Bureau of Mines [1960].

Baptist, O.C., Oil production from frozen reservoir rocks, Umiat, Alaska: Journal of Petroleum Technology, SPE 1219-G, p.85-88, [1959].

Bailey, A., Renaissance says field development will depend on sustained oil prices: Newspaper of Petroleum News, Vol. 14, No. 37, [2009].

Brooks, R.H. and Corey, A.T., Hydraulic properties of porous media: Hydrology paper 3, Colorado State University, Fort Collins, [1964].

Buckley, S.E. and Leverett, M.C., Mechanism of fluid flow in sands: Trans. AIME, 146, p.107-116, [1942].

Collins, F.R., Test Wells, Umiat area, Alaska: U.S .Geological Survey Professional Paper 305-B, p.71-206, [1958].

Core Laboratories Instruments, UPP-200^{TM} probe permeameter operating manual, [2002].

Dake, L.P., Fundamentals of Reservoir Engineering: Elsevier Science, [1983].

Dandekar, A.Y., Petroleum Reservoir Rock and Fluid Properties: CRC Press, Boca Raton, Florida, [2006].

Darcy, H., Les Fontaines Publiques de la Ville de Dyon: Victor Dalmont, [1856].

Free Encyclopedia, "Wikipedia" web link: http://en.wikipedia.org/wiki/Surface_tension

Gaffney, Cline & Associates, Umiat field, Alaska: Technical and commercial review; prepared for Renaissance Alaska, LLC. Houston, Texas, [2006].

Gates, G. L. and Caraway, W.H., Effect of completion fluids on well productivity in permafrost, Umiat field, Alaska: Journal of Petroleum Technology, SPE 201383-G, p.33-40, [1960-A].

Gates, G. L. and Caraway, W.H., Well productivity related to drilling muds: Umiat field, Naval Petroleum Reserve No.4, Alaska: [Washington] U.S. Dept. of the Interior, Bureau of Mines [1960-B].

Goodman M.A., Handbook of arctic well completions: World oil, [1978].

Handa, Y.P., Zakrzewski, M., Fairbridge, C., Effect of restricted geometries on the structure and thermodynamic properties of ice: J. Phys. Chem., Vol. 96, No.21, p.8584-8599, [1992].

International Permafrost Association web link: http://ipa.arcticportal.org/\

Jaiswal, N., Measurement of Gas-Water Relative Permeabilities in Hydrate Systems: M.S. thesis, University of Alaska Fairbanks, [2004].

Jennings, J.B., Capillary pressure techniques: application to exploration and development geology, AAPG Bull., 10, 1196, [1987].

Johnson, E.F., Bossler, D.P. and Naumann, V.O., Calculation of relative permeability from displacement experiments, Trans. AIME, 216, p.370-372, [1959].

Joshi Technologies International Inc, Umiat Field, Alaska: Development with Horizontal wells; prepared for Renaissance Alaska, LLC. Houston, Texas, [2008].

Klinkenberg, L.J., The permeability of porous media to liquids and gases: API drilling and production practice, p.200-213, [1941].

Kunio and Masaru, Amount of unfrozen water in frozen porous media saturated with solution: Cold Regions Science and Technology, Vol. 34, p.103-110, [2002].

Lappo, V.I., "Neftyanoye mestorozhdeniye Nordvik" [The Nordvik Oil Deposit]: "Nedra Arktiki" [Mineral Resources of the Arctic], Moscow-Leningrad, No. 1, p.74-129, [1946].

Leverett, M.C., Flow of oil water mixtures through unconsolidated sands: Trans. AIME, 132, p.381-401, [1939].

Muller, S.W., Permafrost or permanently frozen ground and related engineering problems: J.W. Edwards, Inc., [1947].

Osterkamp, T.E., Petersen J.K. and Collet T.S., Permafrost thicknesses in the Oliktok Point, Prudhoe Bay and Mikkelsen Bay areas of Alaska: Cold Regions Science and Technology, Vol.11, Issue 2, p.99-105, [1985].

Purcell, W.R., Capillary pressures-their measurement using mercury and the calculation of permeability therefrom: Trans. AIME, 186, 39, [1949].

Smith, D.W., Low, N., Cold regions utilities monograph: American Society of Civil Engineers, [1996].

Spaans, E.J.A., Baker, J.M., Examining the use of TDR for measuring liquid water content in frozen soils: Water Resources Research, Vol. 31, No.12, p.2917-2925, [1995].

Tao, T.M., Watson, A.T., Accuracy of JBN estimates of relative permeability: Journal of SPE 11589, p.209-214, [1984].

Tarek A., Reservoir engineering handbook, Gulf Professional Publishing, [2001].

ThermaCAM^{TM} Researcher User's manual, [2003].

Tice, A.R., Burrows, C.M., Anderson, D.M., Determination of unfrozen water in frozen soils by pulsed nuclear magnetic resonance: Proc. 3rd Int. Conf. Permafrost. National Research Council of Canada, Canada, p.149-155, [1978].

Tsytovich, N.A., The Mechanics of Frozen Ground: Scripta Book Co., Washington, D.C., [1975].

Williams, P.J., Unfrozen water content of frozen soils and soil moisture suction: Division of Building Research, Research paper No. 231, Ottawa, [1964].

APPENDIX A. Theory of immiscible displacement and JBN method

Buckley Leverett equation

Buckley and Leverett (1942) developed the theory to describe the immiscible displacement process based on the following assumptions:

1. The flow is one-dimensional and horizontal.
2. The fluid phases are incompressible.
3. Capillary and gravity forces are negligible.
4. Homogeneous rock, porosity (ϕ) and permeability (K) are constant.
5. Displacing fluid is injected at a constant rate.

Note: When the displacing phase is gas, essentially incompressible behavior can be obtained by maintaining a pressure level high enough that the expansion of the gas caused by the pressure drop across the system can be neglected. Due to restrictions of gas flow meter, maximum pressure of 500psi was used at the inlet of the coreholder in this work.

Using Darcy's law for one-dimensional horizontal flow through the homogeneous medium, we have,

$$q_o = -\frac{K \cdot K_{ro} \cdot A}{\mu_o} \times \frac{\partial P_o}{\partial x} \quad (A.1)$$

$$q_w = -\frac{K \cdot K_{rw} \cdot A}{\mu_w} \times \frac{\partial P_w}{\partial x} \quad (A.2)$$

Where,

q_o, q_w = Oil and water flow, cm^3/sec

P_o, P_w = Oil and water differential pressure, atm

μ_o, μ_w = Oil and water viscosity, cp

K_{ro}, K_{rw} = Oil and water relative permeabilities, dimensionless

A = Cross sectional area, cm^2

Assuming that the capillary forces are negligible and therefore P_o=P_w, (A.1) and (A.2) reduce to,

$$\frac{-q_o \cdot \mu_o}{K \cdot K_{ro} \cdot A} = \frac{\partial P_o}{\partial x} \quad (A.3)$$

$$\frac{-q_w \cdot \mu_w}{K \cdot K_{rw} \cdot A} = \frac{\partial P_w}{\partial x} \quad (A.4)$$

Equating the left sides of (A.3) and (A.4) and taking into account that $q_o = q_t - q_w$ where q_t = total flow (cm^3/sec), we get,

$$\frac{q_w}{q_t} = \frac{\frac{\mu_o}{K_{ro}}}{\frac{\mu_o}{K_{ro}} + \frac{\mu_w}{K_{rw}}} \quad (A.5)$$

From (A.5) it follows that the ratio $\frac{q_w}{q_t}$, which is defined as the fractional flow to water (f_w), can be expressed as follows:

$$f_w = \frac{1}{1 + \frac{\mu_w}{\mu_o} \times \frac{K_{ro}}{K_{rw}}} \quad (A.6)$$

Conservation of mass of water flowing through the volume element $A \cdot \phi \cdot dx$, can be expressed as:

$$(q_w \rho_w)_x - (q_w \rho_w)_{x+dx} = A \cdot \phi \cdot dx \times \frac{\partial (\rho_w S_w)}{\partial t} \quad (A.7)$$

So,

$$\frac{\partial (q_w \rho_w)}{\partial x} = -A \cdot \phi \times \frac{\partial (\rho_w S_w)}{\partial t} \quad (A.8)$$

Taking into account the assumption that the fluids are incompressible, we have $\rho_w = const$ and therefore,

$$\frac{\partial q_w}{\partial x} = -A \cdot \phi \times \frac{\partial S_w}{\partial t} \quad (A.9)$$

Similarly we get,

$$\frac{\partial q_o}{\partial x} = -A \cdot \phi \times \frac{\partial S_o}{\partial t} = -A \cdot \phi \times \frac{\partial (1 - S_w)}{\partial t} = A \cdot \phi \times \frac{\partial S_w}{\partial t} \quad (A.10)$$

Where,

ρ_w = Water density, g/cm^3

S_o, S_w = Oil and water saturation, dimensionless

t = Time, sec

Using (A.9) and (A.10), it follows that,

$$\frac{\partial}{\partial x}(q_w + q_o) = \frac{\partial q_t}{\partial x} = 0 \quad (A.11)$$

On the other hand, the assumption that the injection rate is constant implies that,

$$\frac{\partial q_t}{\partial t} = 0 \quad (A.12)$$

Combining (A.11) and (A.12) we get the following result:

$$q_t(x,t) = q_w(x,t) + q_o(x,t) = const \quad \text{(A.13)}$$

This means that the total flow rate at any location is constant throughout the displacement process.

Now define a coordinate function of a surface with $\bar{S}_w$ water saturation, $x_{\bar{S}_w} = x_{\bar{S}_w}(t)$. By the definition of this function, it follows that for all values of time (t) we have:

$$S_w(x_{\bar{S}_w}(t), t) = \bar{S}_w \quad \text{(A.14)}$$

Differentiating both sides of (A.14), we get,

$$0 = \frac{dS_w}{dt}(x_{\bar{S}_w}(t), t) = \frac{\partial S_w}{\partial x_{\bar{S}_w}}(x_{\bar{S}_w}(t), t) \times \frac{dx_{\bar{S}_w}}{dt}(t) + \frac{\partial S_w}{\partial t}(x_{\bar{S}_w}(t), t) \quad (A.15)$$

So,

$$\frac{\partial S_w}{\partial t}(x_{\bar{S}_w}(t), t) = -\frac{\partial S_w}{\partial x_{\bar{S}_w}}(x_{\bar{S}_w}(t), t) \times \frac{dx_{\bar{S}_w}}{dt}(t) \quad (A.16)$$

Substituting (A.16) in (A.10), we get,

$$\frac{\partial q_w}{\partial x_{\bar{S}_w}}(x_{\bar{S}_w}(t), t) = -A \cdot \phi \times \frac{\partial S_w}{\partial t}(x_{\bar{S}_w}(t), t) = A \cdot \phi \times \frac{\partial S_w}{\partial x_{\bar{S}_w}}(x_{\bar{S}_w}(t), t) \times \frac{dx_{\bar{S}_w}}{dt}(t) \quad (A.17)$$

On the other hand,

$$q_w(x_{\bar{S}_w}(t), t) = q_w(\bar{S}_w) = q_w(S_w(x_{\bar{S}_w}(t), t)) \quad (A.18)$$

From (A.18) it follows that,

$$\frac{\partial q_w}{\partial x_{\bar{S}_w}}(x_{\bar{S}_w}(t), t) = \frac{dq_w}{dS_w}(\bar{S}_w) \times \frac{\partial S_w}{\partial x_{\bar{S}_w}}(x_{\bar{S}_w}(t), t) \quad \text{(A.19)}$$

Equating the right sides of (A.17) and (A.19), it follows that the velocity of a plane with constant water saturation $\bar{S}_w$ can be expressed as:

$$\frac{dx_{\bar{S}_w}}{dt}(t) = \frac{1}{A \cdot \phi} \times \frac{dq_w}{dS_w}(\bar{S}_w) \quad (A.20)$$

We showed in (A.13) that $q_t = const$ and we also know that $q_w = q_t \times f_w$. Hence (A.20) can be written as:

$$\frac{dx_{\bar{S}_w}}{dt}(t) = \frac{q_t}{A \cdot \phi} \times \frac{df_w}{dS_w}(\bar{S}_w) \quad (A.21)$$

Equation (A.21) is called the Buckley-Leverett equation. Integrating this equation at the injection time interval $[0, T]$ we will get:

$$x_{\bar{S}_w}(T) = \frac{q_t \cdot T}{A \cdot \phi} \times \frac{df_w}{dS_w}(\bar{S}_w) = \frac{W_i}{A \cdot \phi} \times \frac{df_w}{dS_w}(\bar{S}_w) \quad (A.22)$$

Where $W_i = q_t \cdot T$ is cumulative water injected for the injection time interval $[0, T]$.

Dividing both sides of (A.22) by the length of core L (cm), we get:

$$\frac{x_{\bar{S}_w}(T)}{L} = \frac{W_i}{L \cdot A \cdot \phi} \times \frac{df_w}{dS_w}(\bar{S}_w) = Q_{wi} \times \frac{df_w}{dS_w}(\bar{S}_w) \quad (A.23)$$

Where,

W_i = Cumulative water injected, cm^3

Q_{wi} = Pore volumes of water injected, dimensionless

Welge's extension solution

Figure A.1 shows water saturation distribution as a function of distance from the injector for a fixed time prior to breakthrough. In this example, the maximum water saturation $1\text{-}S_{or}$ has moved at distance x_1 (cm), while the flood front saturation S_{wf} is located at x_2 (cm).

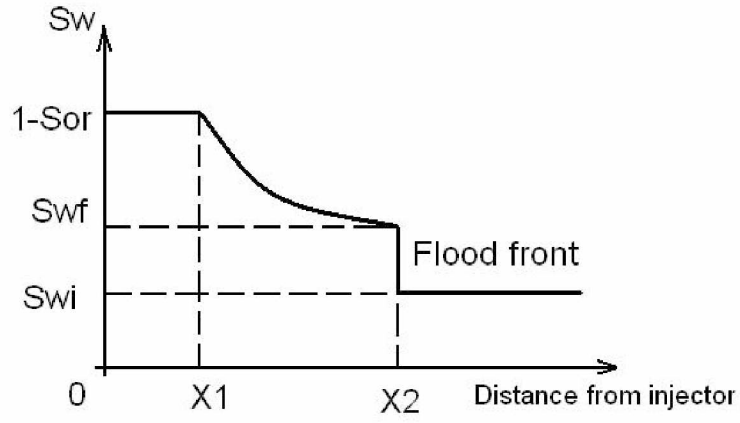

Figure A.1: Water Saturation Distribution vs. Distance from Injector for a Fixed Time

(Modified from Dake, 1983)

S_{or} = Residual oil saturation, dimensionless

S_{wf} = Flood front saturation, dimensionless

For this fixed time t, we can write the material balance as follows:

$$W_i = A \cdot \phi \cdot x_2 \cdot (S_{av} - S_{wi}) \quad (A.24)$$

Where W_i is the cumulative water injected at fixed time t, which is less than the breakthrough time and S_{av} is the average water saturation behind the flood front. From (A.22) it follows that:

$$x_2 = x_{S_{wf}}(t) = \frac{W_i}{A \cdot \phi} \times \frac{df_w}{dS_w}(S_{wf}) \quad (A.25)$$

Substituting (A.25) in (A.24), we get,

$$W_i = A \cdot \phi \times \frac{W_i}{A \cdot \phi} \times \frac{df_w}{dS_w}(S_{wf}) \times (S_{av} - S_{wi}) \quad (A.26)$$

So,

$$\frac{1}{S_{av} - S_{wi}} = \frac{df_w}{dS_w}(S_{wf}) \quad (A.27)$$

The average water saturation behind the shock front can be determined by integrating the saturation profile from the injector to the front location x_2:

$$S_{av} = \frac{\int_0^{x_2} S_w dx}{x_2} = \frac{S_w \cdot x\big|_0^{x_2} - \int_{S_{wf}}^{1-S_{or}} x dS_w}{x_2} = \frac{S_{wf} \cdot x_2 + \int_{S_{wf}}^{1-S_{or}} x dS_w}{x_2} = S_{wf} + \frac{1}{x_2} \times \int_{S_{wf}}^{1-S_{or}} x dS_w = S_{wf} +$$

$$+ \frac{\frac{W_i}{A \cdot \phi} \times \int_{S_{wf}}^{1-S_{or}} \frac{df_w}{dS_w}(S_w) dS_w}{\frac{W_i}{A \cdot \phi} \times \frac{df_w}{dS_w}(S_{wf})} = S_{wf} + \frac{f_w\big|_{S_{wf}}^{1-S_{or}}}{\frac{df_w}{dS_w}(S_{wf})} = S_{wf} + \frac{1 - f_{wf}}{\frac{df_w}{dS_w}(S_{wf})} \quad (A.28)$$

Where f_{wf} is the fractional flow of water at the flood front. Note that $f_w(1 - S_{or}) = 1$ because at this water saturation only water is flowing. Combining (A.27) and (A.28), we get,

$$\frac{df_w}{dS_w}(S_{wf}) = \frac{1 - f_{wf}}{S_{av} - S_{wf}} = \frac{1}{S_{av} - S_{wi}} \quad (A.29)$$

When the shock front arrives at $x = L$, the equation (A.29) implies that,

$$S_{av} = S_{wL} + \frac{1 - f_{wL}}{\frac{df_w}{dS_w}(S_{wL})} \quad (A.30)$$

Where S_{wL} and f_{wL} are water saturation and fractional flow, respectively, at the outlet. If we take $\overline{S}_w = S_{wL}$ in the formula (A.23), then $x_{S_{wL}}(T) = L$ for time T, at which the shock front reaches the outlet. This gives us,

$$\frac{1}{\frac{df_w}{dS_w}(S_{wL})} = Q_{wi} \quad (A.31)$$

Substituting (A.31) in (A.30), we get,

$$S_{wL} = S_{av} - Q_{wi} \cdot f_{oL} \quad (A.32)$$

Welge derived the formula to calculate the fractional oil flow at the outlet f_{oL}:

$$f_{oL} = \frac{dQ_{op}}{dQ_{wi}} \quad (A.33)$$

Where Q_{op} is pore volumes of oil produced, dimensionless. So we can write (A.32) as:

$$S_{wL} = S_{av} - Q_{wi} \times \frac{dQ_{op}}{dQ_{wi}} \quad (A.34)$$

While conducting the experiments, the average water saturation is calculated as:

$$S_{av} = S_{wi} + Q_{op} \quad (A.35)$$

Substituting (A.35) in (A.34), we get,

$$S_{wL} = S_{wi} + Q_{op} - Q_{wi} \times \frac{dQ_{op}}{dQ_{wi}} \quad (A.36)$$

Note that in the case of a gas-oil system, we will have:

$$S_{gL} = Q_{op} - Q_{gi} \times \frac{dQ_{op}}{dQ_{gi}} \quad (A.37)$$

Where,

S_{gL} = Gas saturation at the outlet, dimensionless

Q_{gi} = Pore volumes of gas injected, dimensionless

Based on the formula (A.6), Welge's method also gives us the relationship between relative permeabilities at the outlet water saturations:

$$K_{rwL} = K_{roL} \times \frac{\mu_w}{\mu_o} \times \frac{1 - f_{oL}}{f_{oL}} = K_{roL} \times \frac{\mu_w}{\mu_o} \times \frac{1 - \frac{dQ_{op}}{dQ_{wi}}}{\frac{dQ_{op}}{dQ_{wi}}} \quad (A.38)$$

Johnson-Bossler-Naumann method

In order to determine the relative permeabilities separately, Johnson-Bossler-Naumann adopted Welge's approach and developed the following method.

The pressure gradient across the core sample can be expressed by Darcy's law as:

$$\frac{\partial P}{\partial x} = -\frac{q_o \cdot \mu_o}{K_{eo} \cdot A} = -\frac{q_t \cdot f_o \cdot \mu_o}{K \cdot K_{ro} \cdot A} = -\frac{u \cdot f_o \cdot \mu_o}{K \cdot K_{ro}} \quad (A.39)$$

Where $u = \frac{q_t}{A}$ is the average velocity of fluid flow. Using (A.23) and (A.31), we have

$$dx = dx_{S_w} = L \cdot Q_{wi} \cdot df_w' = L \times \frac{df_w'}{f_{wL}'} \quad (A.40)$$

So,

$$\Delta P = \int_0^L \frac{\partial P}{\partial x} dx = \int_0^L -\frac{u \cdot f_o \cdot \mu_o}{K \cdot K_{ro}} \times L \times \frac{df_w'}{f_{wL}'} = -\frac{u \cdot L \cdot \mu_o}{K \cdot f_{wL}'} \times \int_0^{f_{wL}'} \frac{f_o}{K_{ro}} df_w' \quad (A.41)$$

And hence,

$$\int_0^{f_{wL}'} \frac{f_o}{K_{ro}} df_w' = -\frac{K \cdot f_{wL}' \cdot \Delta P}{\mu_o \cdot u \cdot L} = -\frac{K \cdot K_{ro,\max} \cdot f_{wL}' \cdot \Delta P}{K_{ro,\max} \cdot \mu_o \cdot u \cdot L} = \frac{\left(\frac{u}{\Delta P}\right)_i \times f_{wL}' \cdot \Delta P}{K_{ro,\max} \cdot u} =$$

$$= \frac{\left(\frac{u}{\Delta P}\right)_i}{\left(\frac{u}{\Delta P}\right)} \times \frac{f_{wL}'}{K_{ro,\max}} = \frac{f_{wL}'}{I_r \times K_{ro,\max}} \quad (A.42)$$

Where,

$$I_r = \frac{\left(\frac{u}{\Delta P}\right)}{\left(\frac{u}{\Delta P}\right)_i} \quad (A.43)$$

is called relative injectivity. Relative injectivity is a dimensionless function of cumulative injection, describing the manner in which the intake capacity varies with cumulative injection. From a physical viewpoint, the relative injectivity may be defined as the ratio of the intake capacity at any given flood stage to the intake capacity of the system at the very initiation of the flood, at which moment practically only oil is flowing through the system.

Differentiating (A.42) and using (A.33) we get,

$$K_{roL} = \frac{dQ_{op}}{dQ_{wi}} \times \frac{K_{ro,\max} \cdot d\left(\frac{1}{Q_{wi}}\right)}{d\left(\frac{1}{Q_{wi} \cdot I_r}\right)} \quad (A.44)$$

Note: $K_{ro,\max} = 1$ or $K_{ro,\max} = \frac{K_{eo}\, at\,(S_{wi})}{K_{abs}}$

So using the formula (A.36), (A.38) and (A.44) we can calculate the water saturation at the outlet and the corresponding oil and water relative permeabilities. In case of a gas-oil system, formula (A.36) is replaced with (A.37) and in formula (A.38) and (A.44) the displacing phase is changed to gas.

APPENDIX B. Experimental Results

The following tables and figures contain the gas-oil relative permeability data for Umiat cores 49, 53, 39, 47, 60 and also for Berea sandstone. Flow experiments were repeated for cores 49 and 47 in order to confirm the repeatability of relative permeability determination. The tests were successful, and as seen the data obtained from the first and second runs satisfactorily match each other.

Table B.1: Oil and Gas Relative Permeabilities for Core 49

S_{Liq} (%)	K_{ro}	K_{ro}(ice)		S_{Liq} (%)	K_{rg}	K_{rg}(ice)
100	622×10^{-3}	128×10^{-3}		100	0	0
99.64		714×10^{-4}		99.64		510×10^{-6}
98.92		626×10^{-4}		98.92		592×10^{-6}
98.34	854×10^{-4}			98.34	818×10^{-5}	
98.03		535×10^{-4}		98.03		670×10^{-6}
95.33		357×10^{-4}		95.33		831×10^{-6}
93.36		264×10^{-4}		93.36		899×10^{-6}
93	635×10^{-4}			93	844×10^{-5}	
90.49		179×10^{-4}		90.49		996×10^{-6}
86.9	315×10^{-4}			86.9	884×10^{-5}	
86.18		916×10^{-5}		86.18		110×10^{-5}
86		891×10^{-5}		81.6		113×10^{-5}
81.6		456×10^{-5}		80.28	914×10^{-5}	
80.4		351×10^{-5}		78.94		122×10^{-5}
78.73	796×10^{-5}			78.73	932×10^{-5}	
77.31		171×10^{-5}		74.9		132×10^{-5}
74.9		866×10^{-6}		74.24	942×10^{-5}	
74.24	400×10^{-5}			73.57		134×10^{-5}
73.57		521×10^{-6}		72.32	944×10^{-5}	
72.32	320×10^{-5}			71.64	945×10^{-5}	
71.64	240×10^{-5}			68	988×10^{-5}	
68	125×10^{-5}			64.4	995×10^{-5}	
64.4	801×10^{-6}					

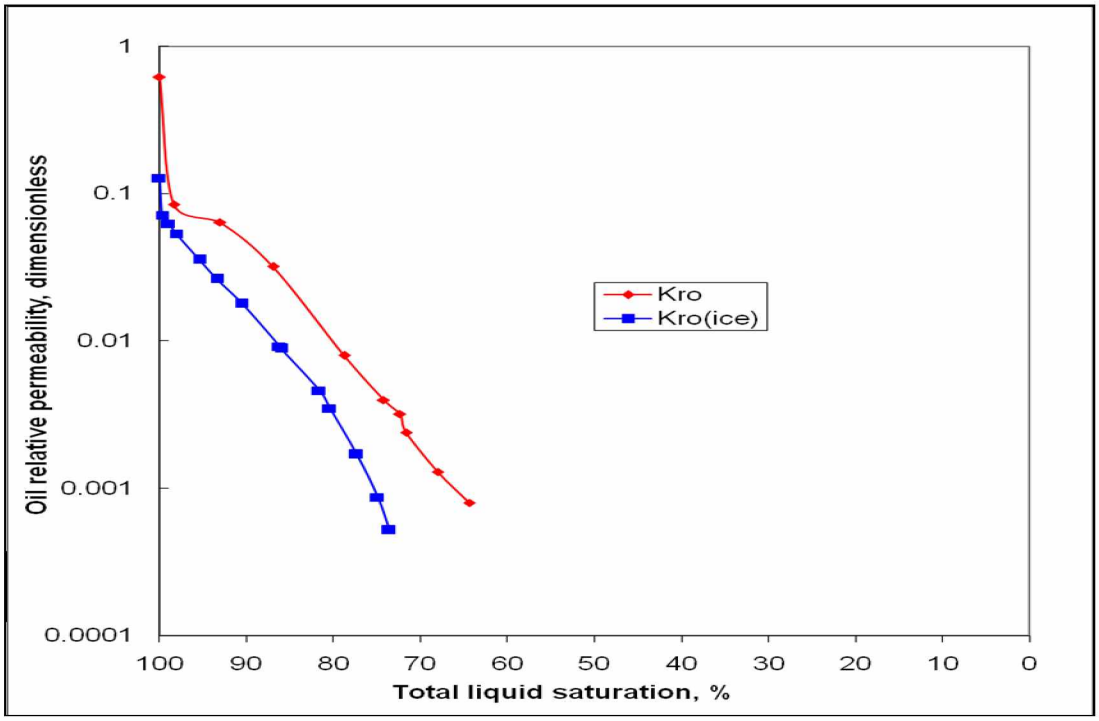

Figure B.1: Oil Relative Permeabilities at 22^{0}C (red) and -10^{0}C (blue) for Umiat Core 49

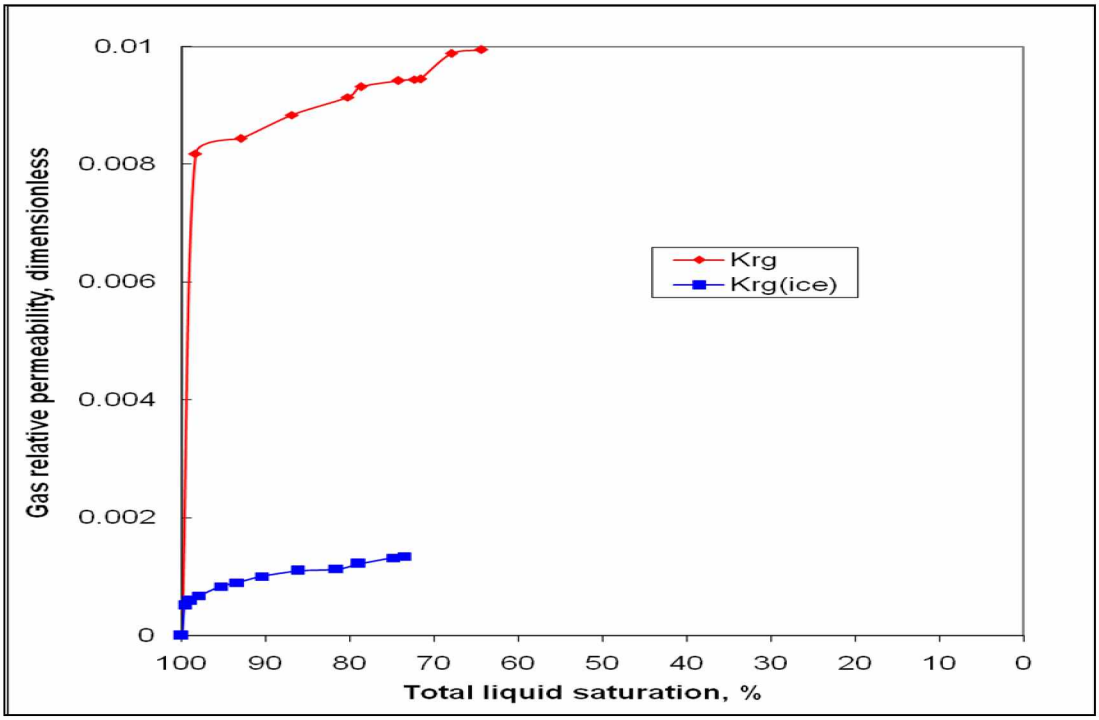

Figure B.2: Gas Relative Permeabilities at 22^{0}C (red) and -10^{0}C (blue) for Umiat Core 49

Table B.2: Oil and Gas Relative Permeabilities for Core 49 [second run]

S_{Liq} (%)	K_{ro}	K_{ro}(ice)		S_{Liq} (%)	K_{rg}	K_{rg}(ice)
100	582×10^{-3}	222×10^{-3}		100	0	0
98		920×10^{-4}		98		115×10^{-5}
97.27	747×10^{-4}			97.27	771×10^{-5}	
93.26		464×10^{-4}		93.26		158×10^{-5}
92.9	595×10^{-4}			92.9	790×10^{-5}	
87.07		154×10^{-4}		87.07		185×10^{-5}
83.34	149×10^{-4}			83.34	862×10^{-5}	
82.06		764×10^{-5}		82.07		190×10^{-5}
78.83		431×10^{-5}		77.31	884×10^{-5}	
77.31	376×10^{-5}			76.92		199×10^{-5}
76.92		312×10^{-5}		74.55		210×10^{-5}
73.19		904×10^{-6}		63.9	931×10^{-5}	
71.24	225×10^{-5}					
63.9	750×10^{-6}					

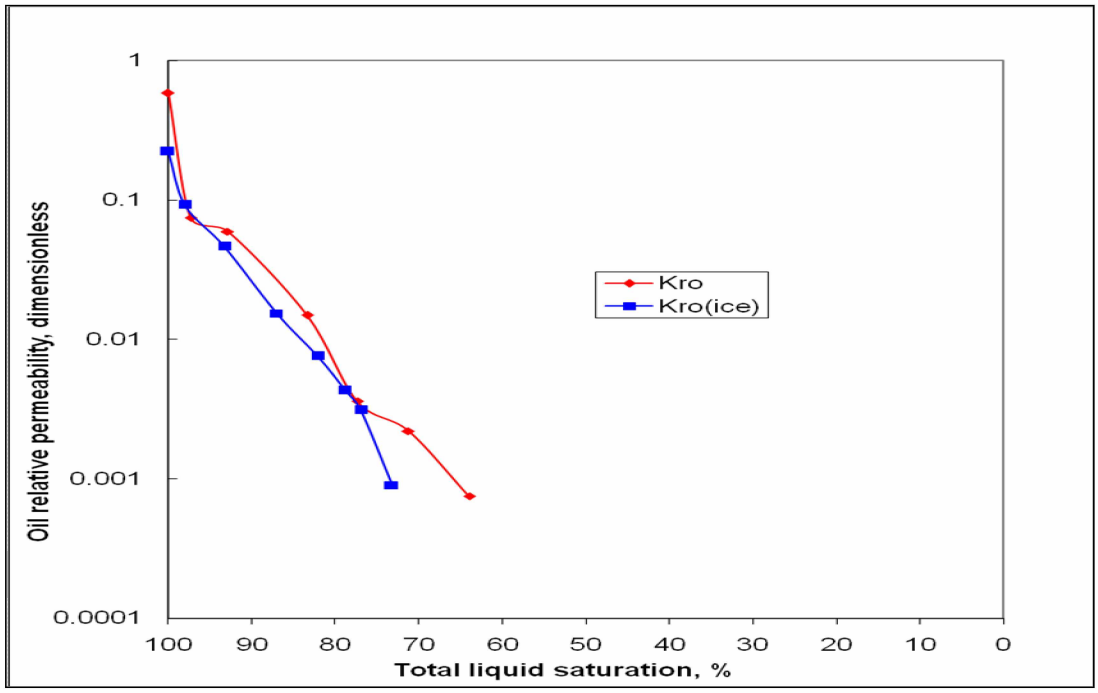

Figure B.3: Oil Relative Permeabilities at 22^{0}C (red) and -10^{0}C (blue) for Umiat Core 49 [second run]

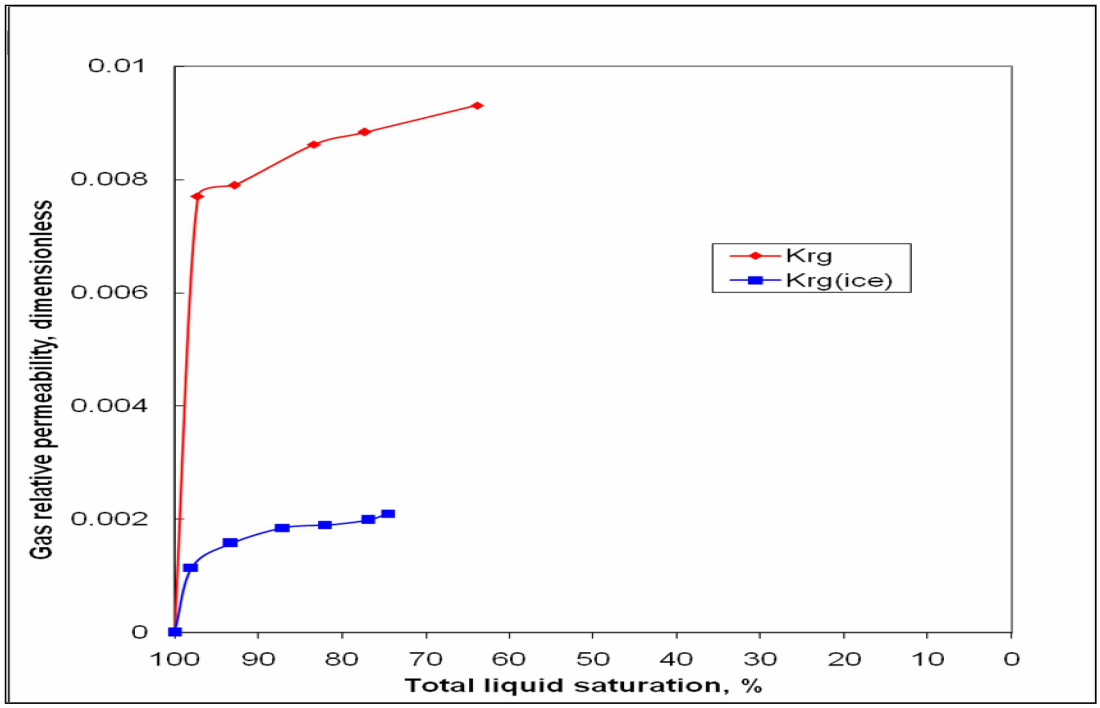

Figure B.4: Gas Relative Permeabilities at 22^{0}C (red) and -10^{0}C (blue) for Umiat Core 49 [second run]

Table B.3: Oil and Gas Relative Permeabilities for Core 53

S_{Liq} (%)	K_{ro}	K_{ro}(ice)		S_{Liq} (%)	K_{rg}	K_{rg}(ice)
100	453×10^{-3}	196×10^{-3}		100	0	0
80.54	396×10^{-3}			80.54	855×10^{-6}	
76.57	234×10^{-3}			76.57	336×10^{-5}	
73.65		113×10^{-3}		73.65		748×10^{-6}
71.78	116×10^{-3}			71.78	512×10^{-5}	
66.4		662×10^{-4}		66.4		116×10^{-5}
64.11		530×10^{-4}		64.11		128×10^{-5}
63.53	581×10^{-4}			63.53	600×10^{-5}	
62.1		397×10^{-4}		62.1		140×10^{-5}
58.9	445×10^{-4}			57.53		152×10^{-5}
57.53		265×10^{-4}		56.36	641×10^{-5}	
56.36	333×10^{-4}			53.28	661×10^{-5}	
53.28	235×10^{-4}			50.26	679×10^{-5}	
50.26	118×10^{-4}					

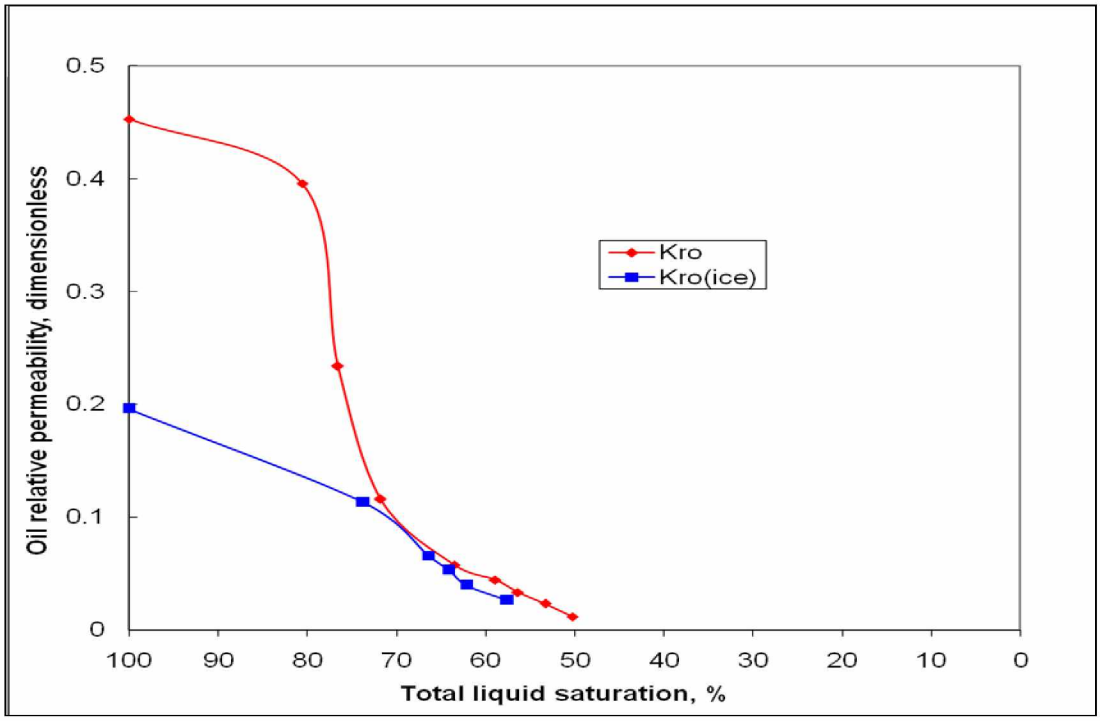

Figure B.5: Oil Relative Permeabilities at 22^{0}C (red) and -10^{0}C (blue) for Umiat Core 53

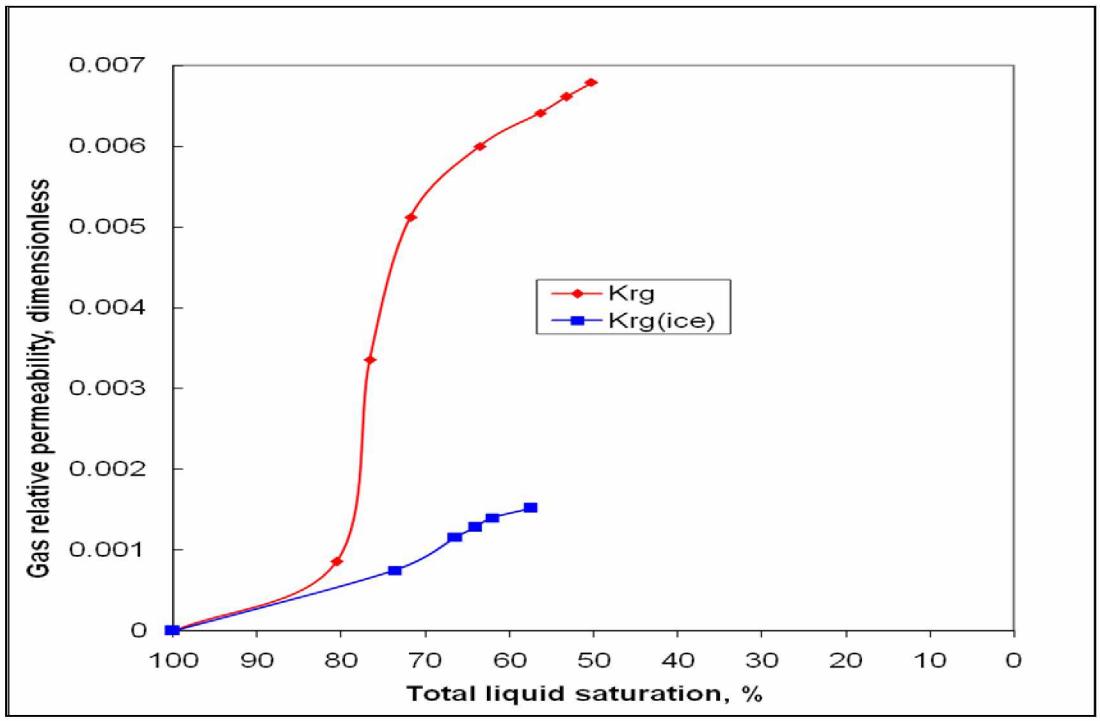

Figure B.6: Gas Relative Permeabilities at 22^{0}C (red) and -10^{0}C (blue) for Umiat Core 53

Table B.4: Oil and Gas Relative Permeabilities for Core 39

S_{Liq} (%)	K_{ro}	K_{ro}(ice)		S_{Liq} (%)	K_{rg}	K_{rg}(ice)
100	714×10^{-3}	335×10^{-3}		100	0	0
79.06	681×10^{-3}			77.47	247×10^{-5}	
77.47	552×10^{-3}			76.25		794×10^{-6}
76.25		247×10^{-3}		75.2	528×10^{-5}	
75.2	368×10^{-3}			72.4	809×10^{-5}	
72.4	184×10^{-3}			71		190×10^{-5}
71		123×10^{-3}		69.35	949×10^{-5}	
69.95	919×10^{-4}			68.11	977×10^{-5}	
68.11	736×10^{-4}			66.4	993×10^{-5}	
66.4	486×10^{-4}			65.15		246×10^{-5}
65.15		617×10^{-4}		64.23	104×10^{-4}	
64.23	368×10^{-4}			62.6		268×10^{-5}
62.6		370×10^{-4}		58.71		279×10^{-5}
58.71		247×10^{-4}		55.95		290×10^{-5}
55.95		123×10^{-4}				

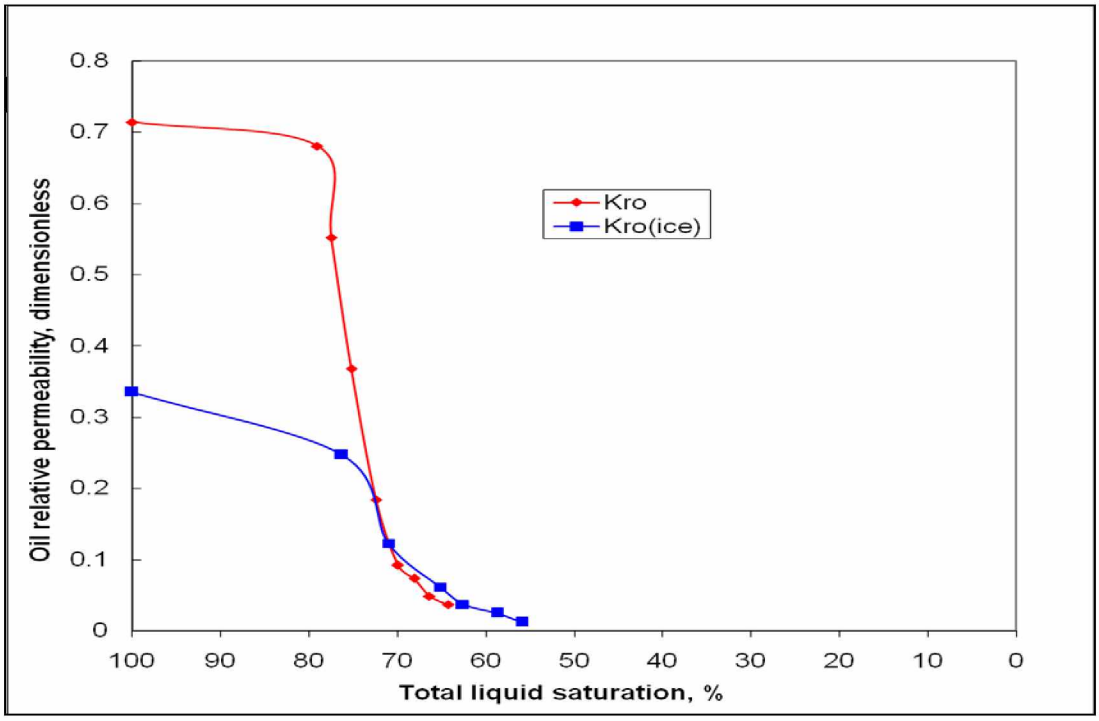

Figure B.7: Oil Relative Permeabilities at 22^{0}C (red) and -10^{0}C (blue) for Umiat Core 39

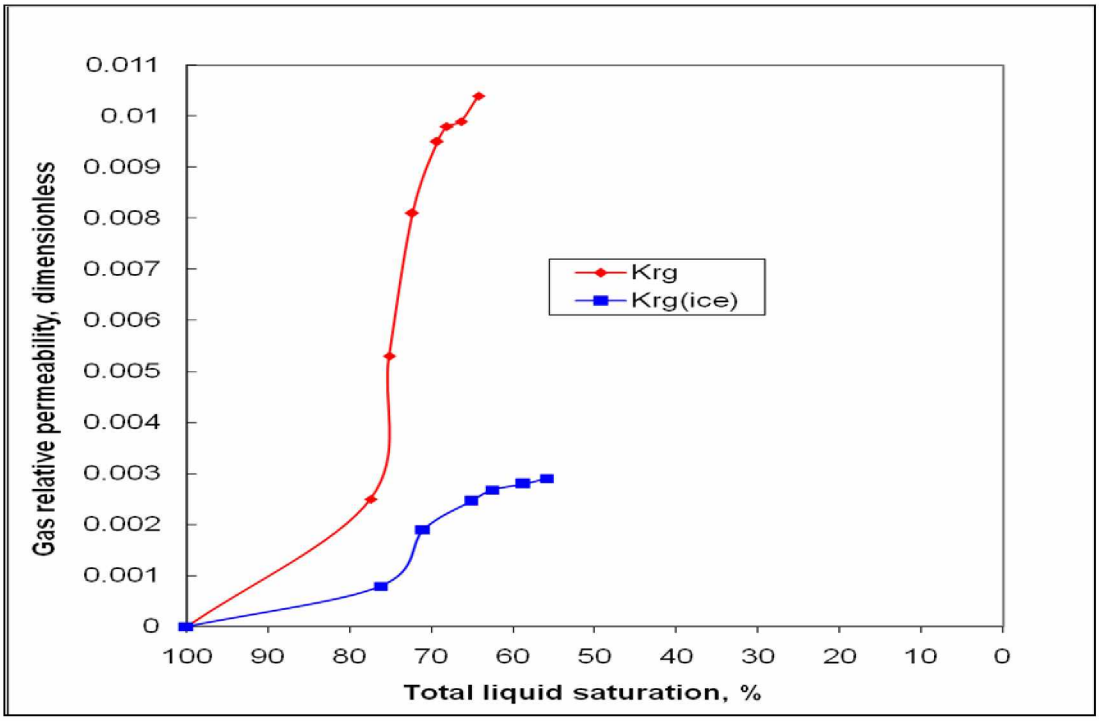

Figure B.8: Gas Relative Permeabilities at 22^{0}C (red) and -10^{0}C (blue) for Umiat Core 39

Table B.5: Oil and Gas Relative Permeabilities for Core 47

S_{Liq} (%)	K_{ro}	K_{ro}(ice)		S_{Liq} (%)	K_{rg}	K_{rg}(ice)
100	568×10^{-3}	480×10^{-4}		100	0	0
86.74		974×10^{-6}		80.1		437×10^{-6}
85.05	124×10^{-3}			78.17		444×10^{-6}
83.22		621×10^{-6}		71.8	750×10^{-5}	
82.3		547×10^{-6}		70.78		450×10^{-6}
79.77		344×10^{-6}		68.3	920×10^{-5}	
77.67		230×10^{-6}		65.72	964×10^{-5}	
73.98	290×10^{-4}			65.59		460×10^{-6}
72.76		112×10^{-6}		62.6		467×10^{-6}
71.8	187×10^{-4}			62.48	107×10^{-4}	
70.22	163×10^{-4}			61.32	112×10^{-4}	
68.3	141×10^{-4}			60.99	118×10^{-4}	
66.41		547×10^{-7}		59.35		472×10^{-6}
65.56	982×10^{-5}			55.04	167×10^{-4}	
64.15		434×10^{-7}		54.87	169×10^{-4}	
62.48		325×10^{-7}		53.6	170×10^{-4}	
61.32	519×10^{-5}			52.2	172×10^{-4}	
60.93		217×10^{-7}				
59.35		123×10^{-7}				
57.56		105×10^{-7}				
53.64	163×10^{-5}					
52.2	826×10^{-6}					

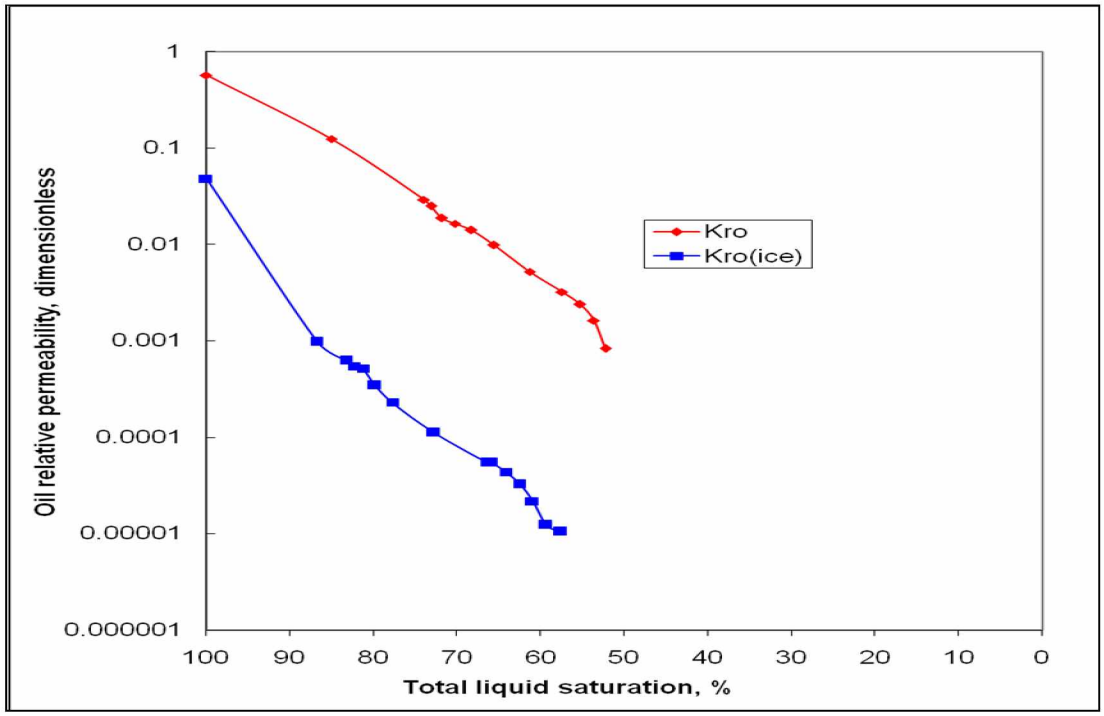

Figure B.9: Oil Relative Permeabilities at 22^{0}C (red) and -10^{0}C (blue) for Umiat Core 47

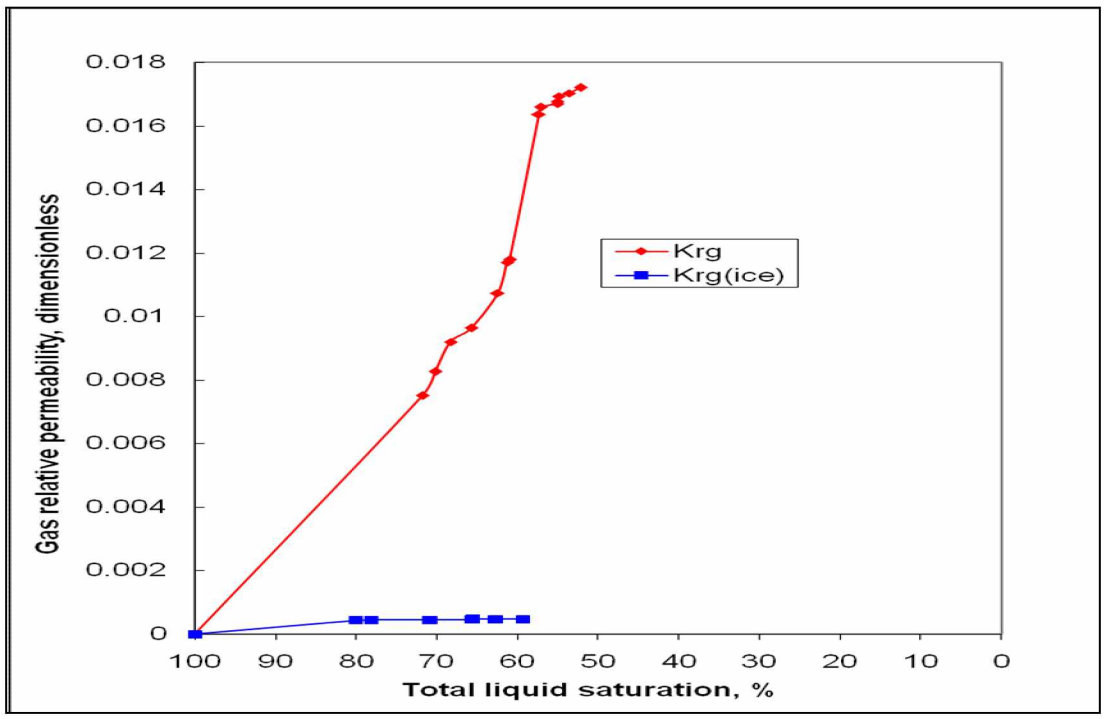

Figure B.10: Gas Relative Permeabilities at 22^{0}C (red) and -10^{0}C (blue) for Umiat Core 47

Table B.6: Oil and Gas Relative Permeabilities for Core 47 [second run]

S_{Liq} (%)	K_{ro}	K_{ro}(ice)		S_{Liq} (%)	K_{rg}	K_{rg}(ice)
100	565×10^{-3}	947×10^{-4}		100	0	0
88.87		237×10^{-5}		88.87		804×10^{-6}
85.24	123×10^{-3}			85.24	638×10^{-5}	
82.52		108×10^{-5}		82.52		819×10^{-6}
76.52		265×10^{-6}		74.31	815×10^{-5}	
74.31	288×10^{-4}			73.11		843×10^{-6}
72.94		227×10^{-6}		68.7	951×10^{-5}	
70.59	162×10^{-4}			68.48		874×10^{-6}
68.7	140×10^{-4}			66.26		894×10^{-6}
68.48		114×10^{-6}		63.07		923×10^{-6}
63.2		643×10^{-7}		62.95	107×10^{-4}	
62.95	516×10^{-5}			59.86		931×10^{-6}
58	238×10^{-5}			57.92	133×10^{-4}	
57.68		207×10^{-7}		55.8	165×10^{-4}	
54.22	120×10^{-5}			52.81	171×10^{-4}	
52.81	821×10^{-6}					

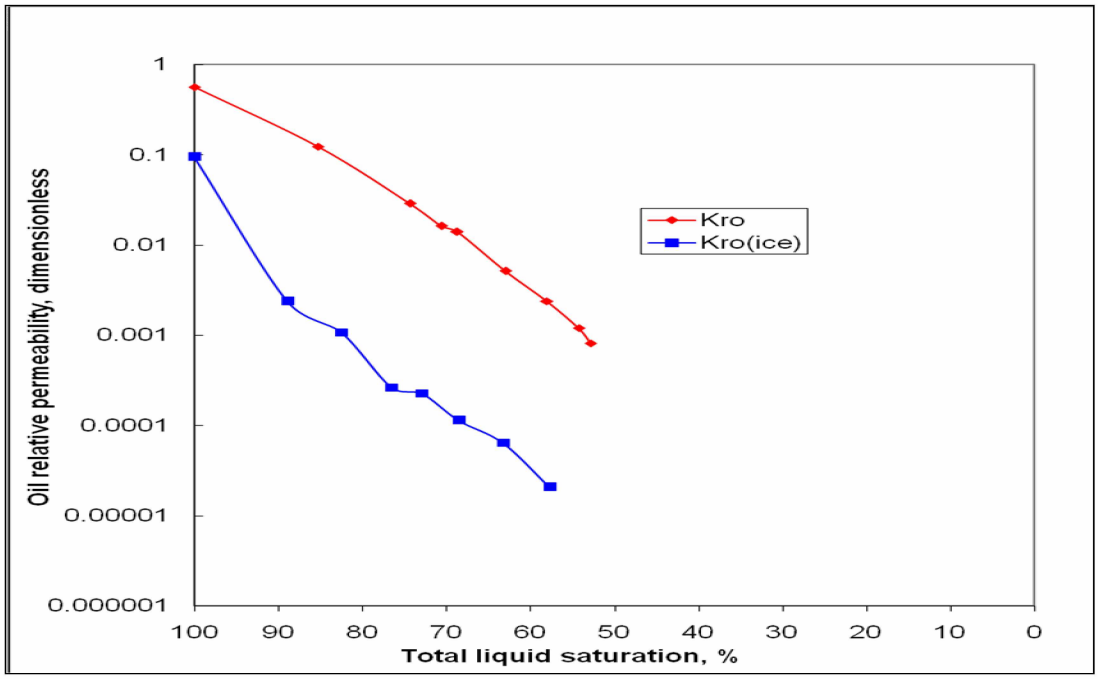

Figure B.11: Oil Relative Permeabilities at 22^{0}C (red) and -10^{0}C (blue) for Umiat Core 47 [second run]

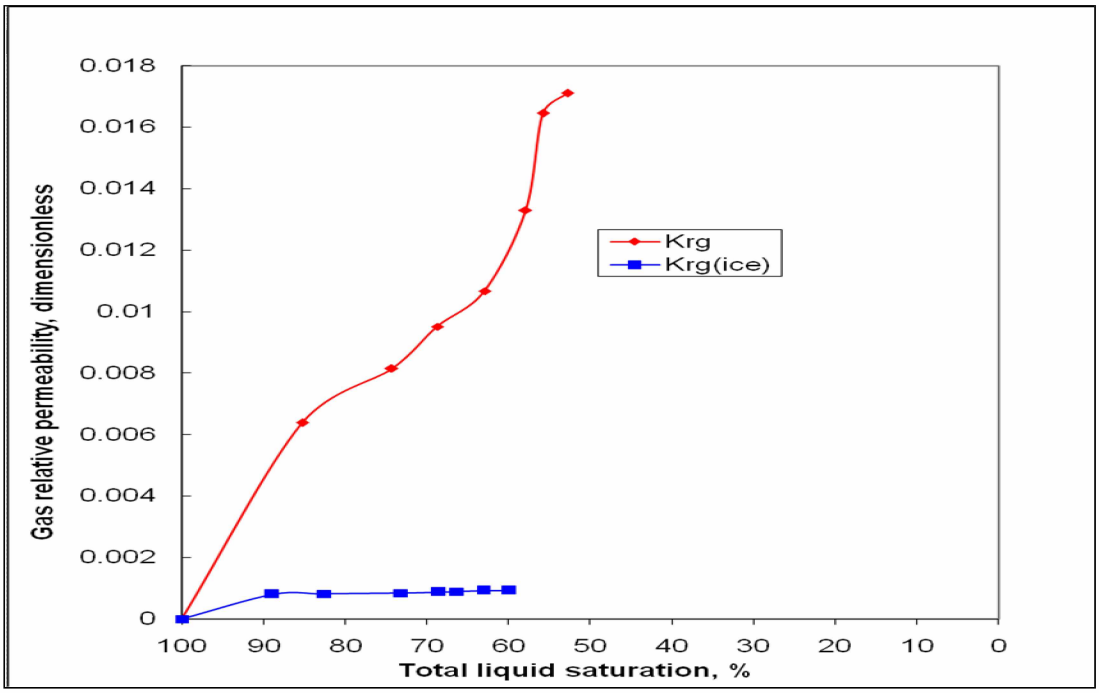

Figure B.12: Gas Relative Permeabilities at 22^{0}C (red) and -10^{0}C (blue) for Umiat Core 47 [second run]

Table B.7: Oil and Gas Relative Permeabilities for Core 60

S_{Liq} (%)	K_{ro}	K_{ro}(ice)		S_{Liq} (%)	K_{rg}	K_{rg}(ice)
100	450×10^{-3}	244×10^{-3}		100	0	0
92.5	430×10^{-3}			92.5	293×10^{-6}	
88	418×10^{-3}			88	416×10^{-6}	
85.97	391×10^{-3}			85.97	786×10^{-6}	
82.45	353×10^{-3}			82.45	142×10^{-5}	
81.72	335×10^{-3}			81.72	150×10^{-5}	
76.38	289×10^{-3}			76.38	244×10^{-5}	
72.41	241×10^{-3}			72.41	298×10^{-5}	
68.31	202×10^{-3}			68.31	362×10^{-5}	
67.72		157×10^{-3}		67.72		780×10^{-6}
61.79		944×10^{-4}		64.93		135×10^{-5}
59.8	123×10^{-3}			63.32		163×10^{-5}
52.75		315×10^{-4}		59.8	493×10^{-5}	
				52.75		192×10^{-5}

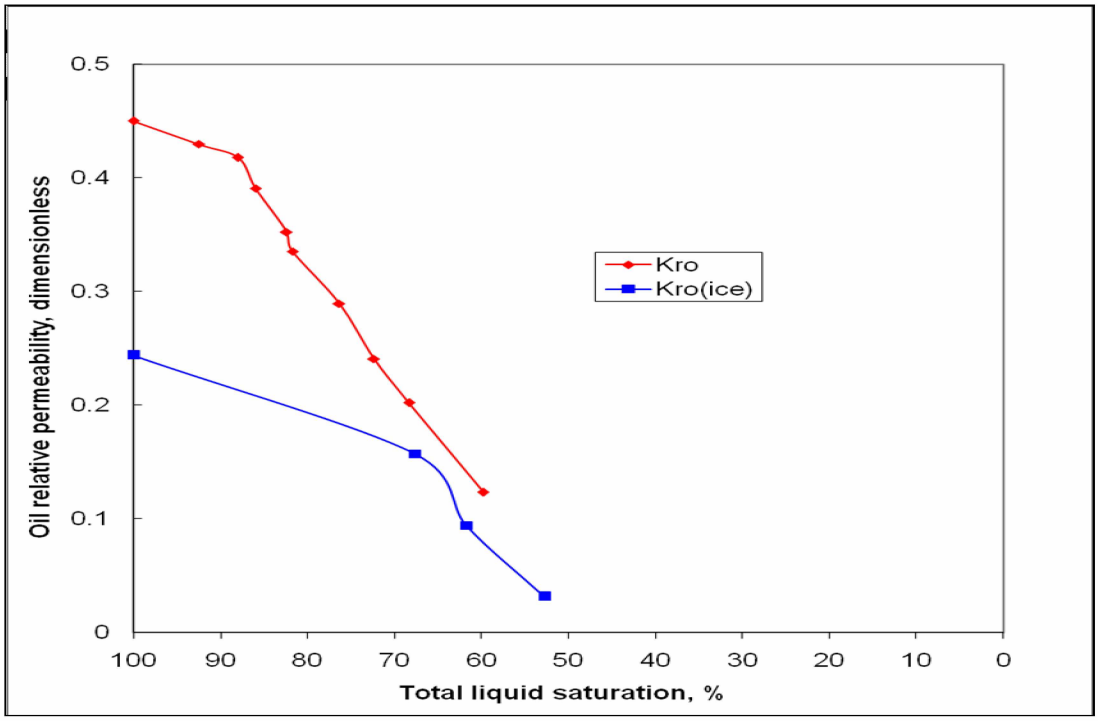

Figure B.13: Oil Relative Permeabilities at 22^{0}C (red) and -10^{0}C (blue) for Umiat Core 60

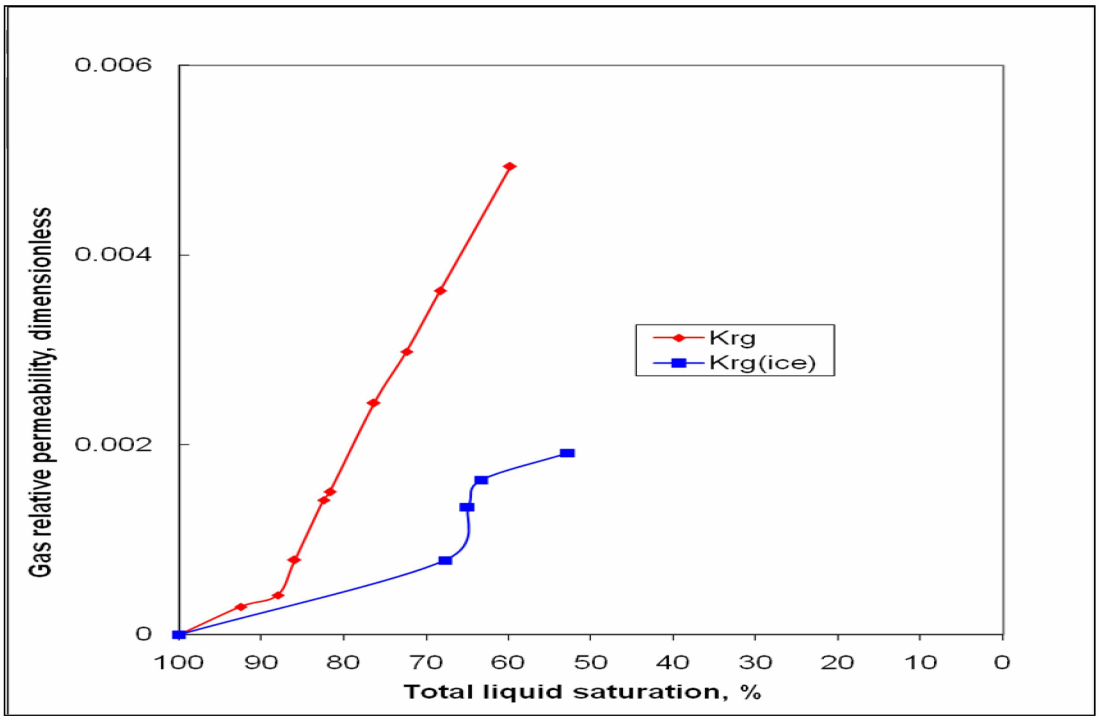

Figure B.14: Gas Relative Permeabilities at 22^{0}C (red) and -10^{0}C (blue) for Umiat Core 60

Table B.8: Oil and Gas Relative Permeabilities for Berea SS

S_{Liq} (%)	K_{ro}	K_{ro}(ice)		S_{Liq} (%)	K_{rg}	K_{rg}(ice)
100	855×10^{-3}	534×10^{-3}		100	0	0
91.14		427×10^{-3}		91.14		632×10^{-5}
89.26		265×10^{-3}		89.26		112×10^{-4}
88.44		224×10^{-3}		88.44		138×10^{-4}
87.55		173×10^{-3}		87.55		167×10^{-4}
86.9		143×10^{-3}		86.9		194×10^{-4}
85.43		115×10^{-3}		86.35		218×10^{-4}
85.04	589×10^{-3}			85.73		250×10^{-4}
84.23		731×10^{-4}		82.94		386×10^{-4}
83.44	406×10^{-3}			80.97	355×10^{-4}	
82.94		446×10^{-4}		79.93	518×10^{-4}	
82.17	349×10^{-3}			79.31	747×10^{-4}	
81.11		328×10^{-4}		77.93	142×10^{-3}	
80.97	281×10^{-3}			77.75	211×10^{-3}	
77	248×10^{-3}			76.9		778×10^{-4}
76.9		715×10^{-5}		75.52	288×10^{-3}	
76.48	198×10^{-3}			73.48	296×10^{-3}	
75.77	176×10^{-3}			71.82	314×10^{-3}	
75.52	102×10^{-3}			69.91	372×10^{-3}	
73.48	569×10^{-4}			69.66		248×10^{-3}
72.71	410×10^{-4}			68.23	481×10^{-3}	
71.82	318×10^{-4}					
70.91	151×10^{-4}					

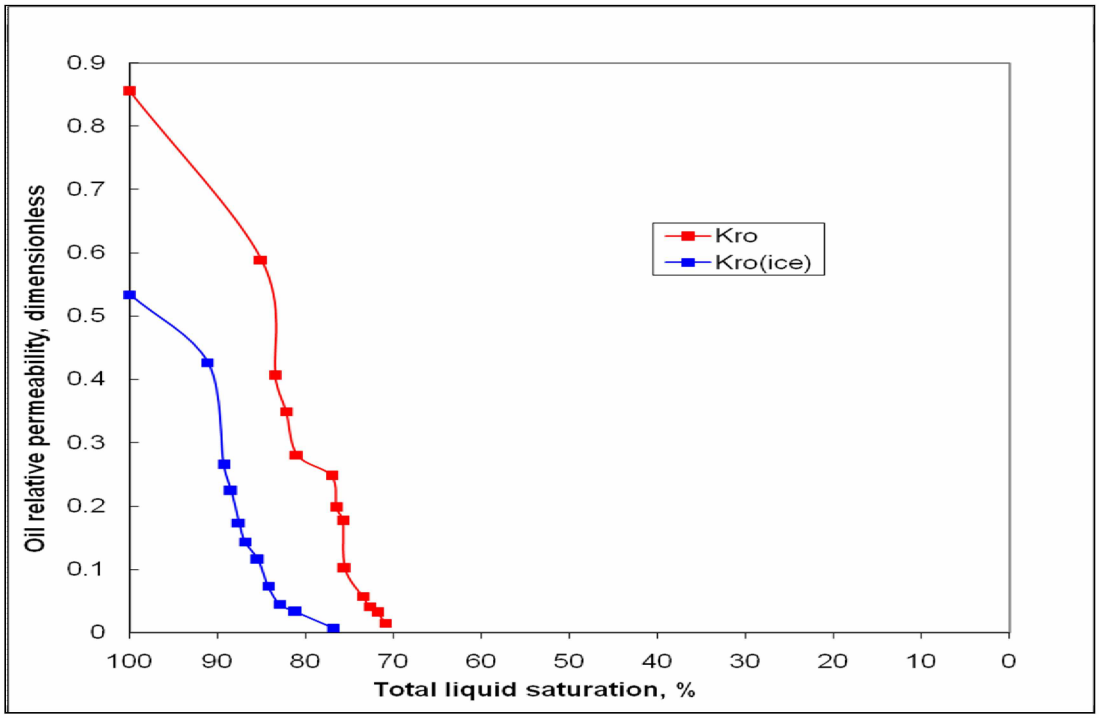

Figure B.15: Oil Relative Permeabilities at 22^{0}C (red) and -7^{0}C (blue) for Berea SS

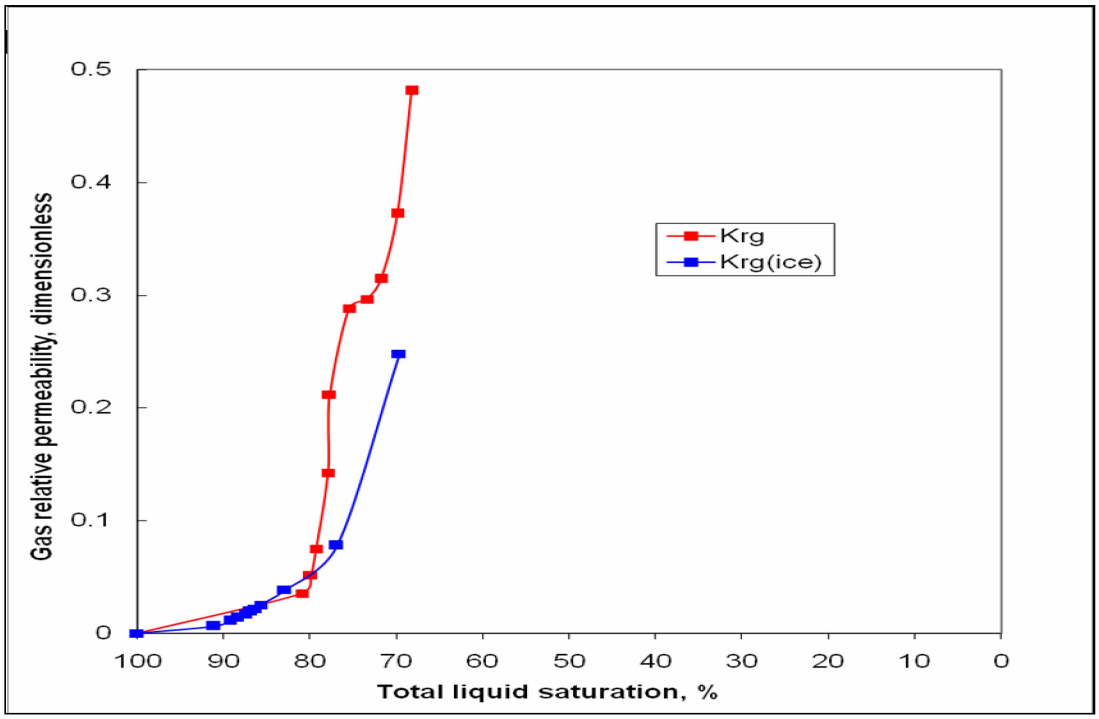

Figure B.16: Gas Relative Permeabilities at 22^{0}C (red) and -7^{0}C (blue) for Berea SS

APPENDIX C. Relative permeability sample calculations

Table C.1 represents the data recorded for core 40, while injecting gas, at two consecutive time steps, 46 and 48 seconds after gas injection has started at $\Delta P_{(initial)}$=293.4 psi pressure differential.

Table C.1: Data Recorded for Core 40 during Gas Injection

A	B	C	D	E	F	G	H	I
t (time) sec	M(t) g	Q_{op}	Flow rate cm^3/sec	Q_{gi}	ΔP psi	I_r	$1/Q_{gi}$	$1/(Q_{gi} \times I_r)$
46	1.588	0.274	0.015	0.092	290.6	1.0096	10.87	10.77
48	1.607	0.277		0.096	290.4	1.0103	10.42	10.31

J	K	L	M	N	O
$\frac{d(1/Q_{gi})}{d(1/Q_{gi} \times I_r)}$	$\frac{d(Q_{op})}{d(Q_{gi})}$	S_{gL}	K_{roL}	K_{rgL}	S_{Liq}
0.98	0.75	0.21	0.351	0.00178	0.79

A: Time passed since gas injection has started.

B: Mass of cumulative oil produced for corresponding time steps. The data is taken from electronic balance.

C: Cumulative oil produced in terms of pore volumes, $Q_{op}(t) = \frac{M(t)}{\rho_o \times PV}$.

$$Q_{op}(46) = \frac{1.558}{0.776 \times 7.478} = 0.274$$

$$Q_{op}(48) = \frac{1.607}{0.776 \times 7.478} = 0.277$$

Where $\rho_o = 0.776$ g/cm^3 is the density of kerosene and $PV = 7.478$ is the pore volume of core 40 which was determined prior to gas injection.

D: Gas injection flow rate which is constant throughout the experiment. The data is taken from gas flow meter device.

E: Cumulative gas injected in terms of pore volumes, $Q_{gi}(t) = \frac{Flow\ rate \times t}{PV}$.

$$Q_{gi}(46) = \frac{0.015 \times 46}{7.478} = 0.092$$

$$Q_{gi}(48) = \frac{0.015 \times 48}{7.478} = 0.096$$

F: Pressure differential across the core for corresponding time steps. The data is taken from pressure gauge.

G: Relative injectivity, $I_r(t) = \frac{\Delta P_{(initial)}}{\Delta P(t)}$.

$$I_r(46) = \frac{293.4}{290.6} = 1.0096$$

$$I_r(48) = \frac{293.4}{290.4} = 1.0103$$

H: The following ratio, $\frac{1}{Q_{gi}(t)}$, is calculated for corresponding time steps.

$$\frac{1}{Q_{gi}(46)} = \frac{1}{0.092} = 10.87$$

$$\frac{1}{Q_{gi}(48)} = \frac{1}{0.096} = 10.42$$

I: The following ratio, $\frac{1}{Q_{gi}(t) \times I_r(t)}$, is calculated for corresponding time steps.

$$\frac{1}{Q_{gi}(46)\times I_r(46)} = \frac{1}{0.092\times 1.0096} = 10.77$$

$$\frac{1}{Q_{gi}(48)\times I_r(48)} = \frac{1}{0.096\times 1.0103} = 10.31$$

J: The following derivative, $\frac{d(1/Q_{gi})}{d(1/Q_{gi}\times I_r)}$, is calculated numerically by the forward differentiation formula, $\frac{df}{dt}(t_i) = \frac{f(t_{i+1}) - f(t_i)}{t_{i+1} - t_i}$.

$$\frac{d(1/Q_{gi})}{d(1/Q_{gi}\times I_r)}(46) = \frac{\frac{1}{Q_{gi}}(48) - \frac{1}{Q_{gi}}(46)}{\frac{1}{Q_{gi}\times I_r}(48) - \frac{1}{Q_{gi}\times I_r}(46)} = \frac{10.42-10.87}{10.31-10.77} = 0.98$$

Calculation for time step t=48 sec is not presented because it requires the data from time step t=50 sec.

K: The following derivative, $\frac{d(Q_{op})}{d(Q_{gi})}$, is calculated similarly.

$$\frac{d(Q_{op})}{d(Q_{gi})}(46) = \frac{Q_{op}(48) - Q_{op}(46)}{Q_{gi}(48) - Q_{gi}(46)} = \frac{0.277-0.274}{0.096-0.092} = 0.75$$

L: Gas saturation is calculated by the (A.37) formula.

$$S_{gL}(46) = Q_{op}(46) - Q_{gi}(46)\times\frac{dQ_{op}}{dQ_{gi}}(46) = 0.274 - 0.092\times 0.75 = 0.21$$

M: Relative oil permeability is calculated by the (A.44) formula.

$$K_{roL}(46) = \frac{dQ_{op}}{dQ_{gi}}(46)\times K_{ro,\max}\times\frac{d(1/Q_{gi})}{d(1/Q_{gi}\times I_r)}(46) = 0.75\times 0.478\times 0.98 = 0.351$$

N: Relative gas permeability is calculated by the (A.38) formula.

$$K_{rgL}(46) = K_{roL}(46) \times \frac{\mu_g}{\mu_o} \times \frac{1 - \frac{dQ_{op}}{dQ_{gi}}(46)}{\frac{dQ_{op}}{dQ_{gi}}(46)} = 0.351 \times \frac{0.01756}{1.15} \times \frac{1 - 0.75}{0.75} = 0.00178$$

Where μ_g and μ_o are gas and oil viscosities respectively.

O: Total liquid saturation which is calculated as follows:

$$S_{Liq}(46) = 1 - S_{gL}(46) = 1 - 0.21 = 0.79$$

Obtained data, $S_{Liq} = 79\%$, $K_{roL} = 351 \times 10^{-3}$ and $K_{rgL} = 178 \times 10^{-5}$, with a bit of difference caused by rounding errors, is presented in the third row of table 8.

APPENDIX D. Corey exponents

A log-log plot of relative oil and gas permeabilities at freezing conditions versus normalized saturations for Umiat cores 49, 53, 39, 47 and 60 is shown in the following figures. Experimentally-obtained oil and gas relative permeability data at -10^0C for these Umiat cores as well as their analytical representations using calculated Corey exponents are presented in subsequent figures.

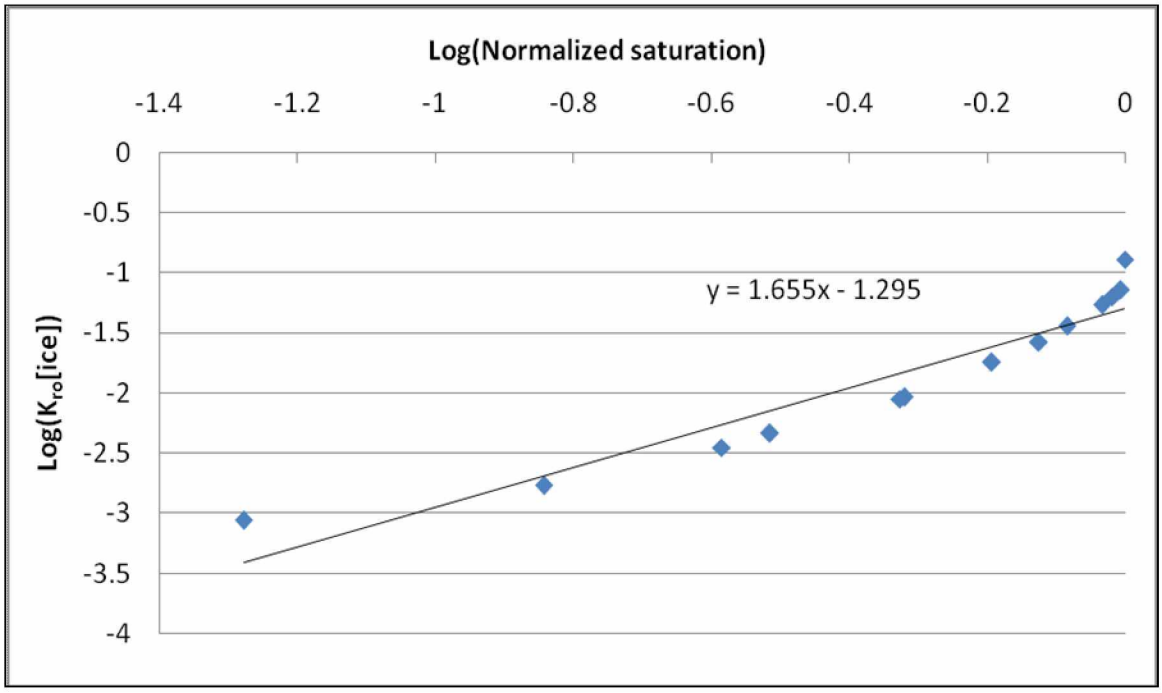

Figure D1: Relative Oil Permeability versus Normalized Saturation for Umiat Core 49

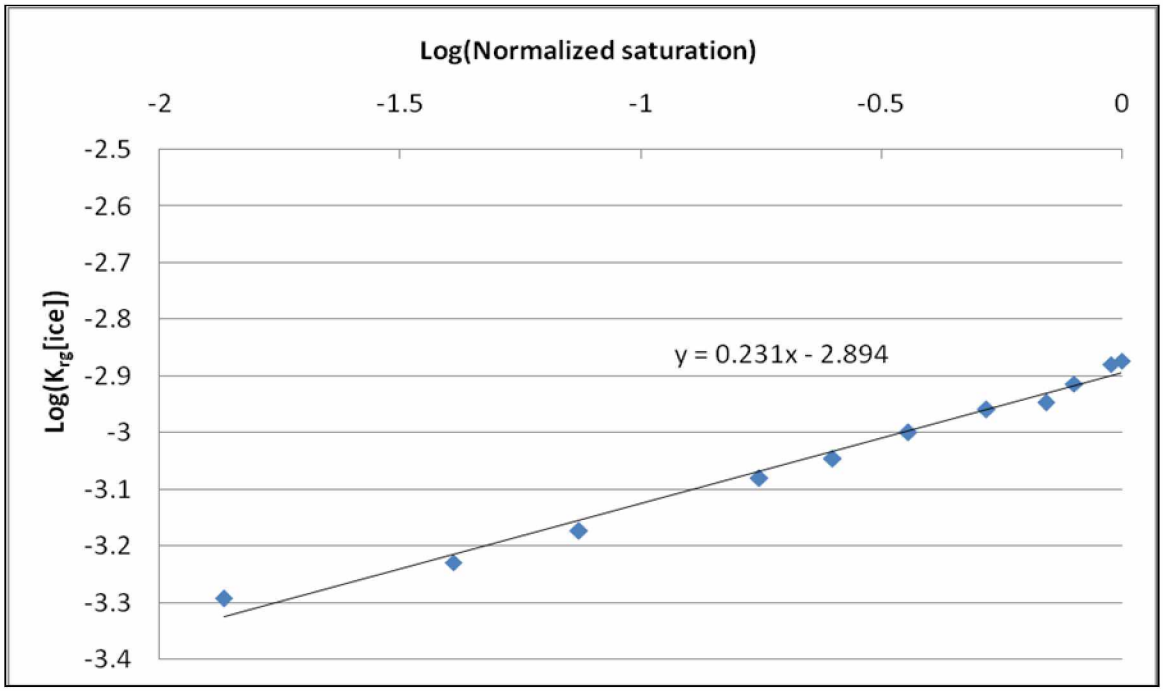

Figure D2: Relative Gas Permeability versus Normalized Saturation for Umiat Core 49

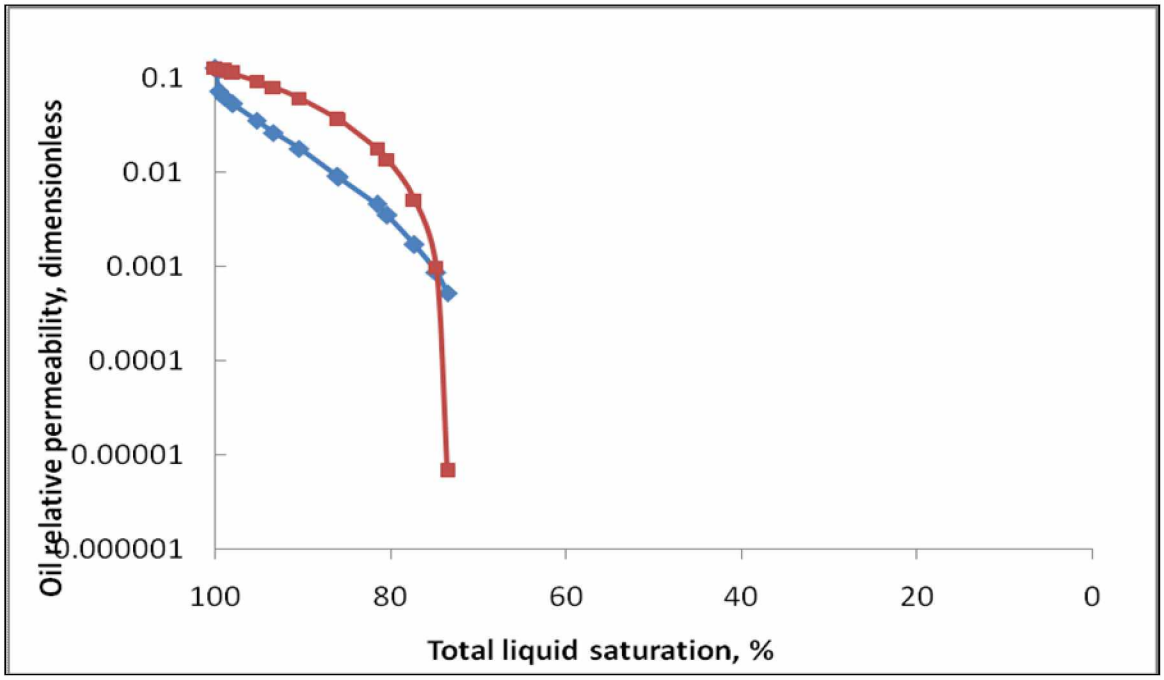

Figure D3: Experimentally-Obtained Oil Relative Permeability Data (blue) and its Analytical Representation (red) for Umiat Core 49

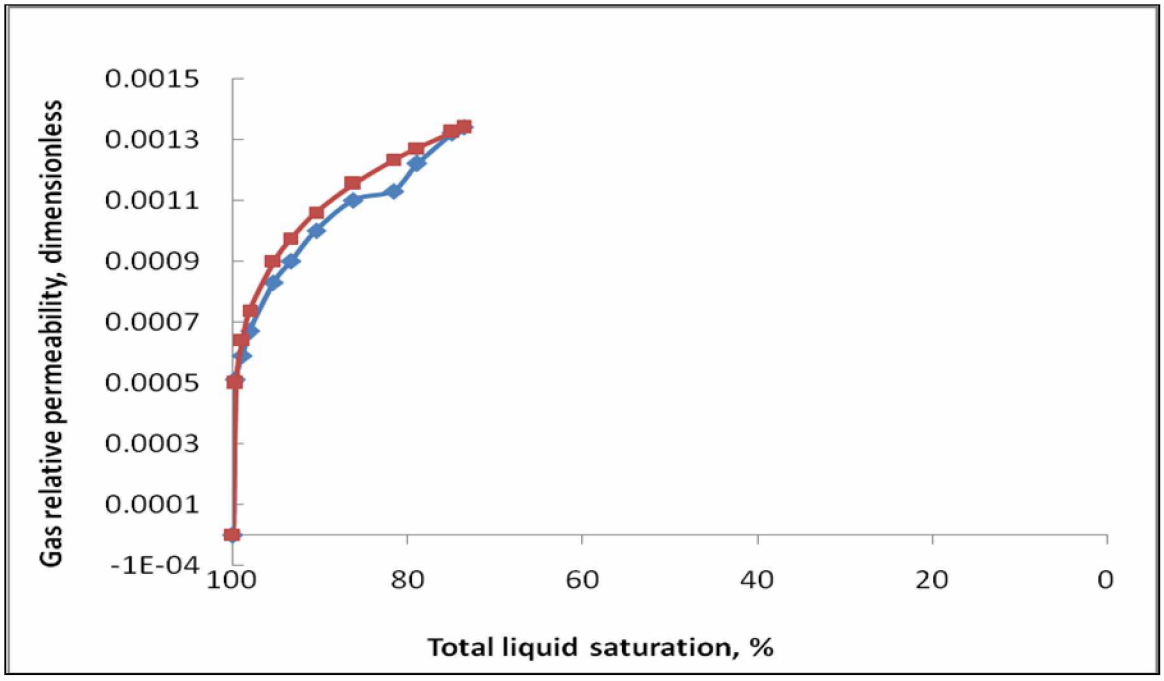

Figure D4: Experimentally-Obtained Gas Relative Permeability Data (blue) and its Analytical Representation (red) for Umiat Core 49

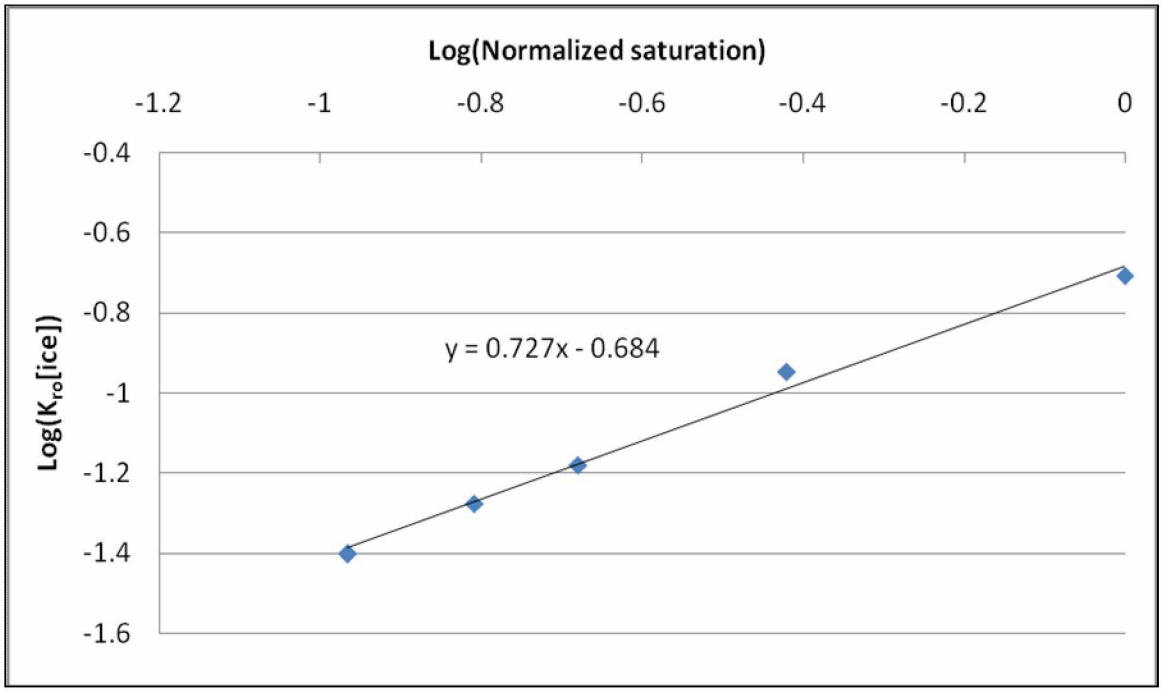

Figure D5: Relative Oil Permeability versus Normalized Saturation for Umiat Core 53

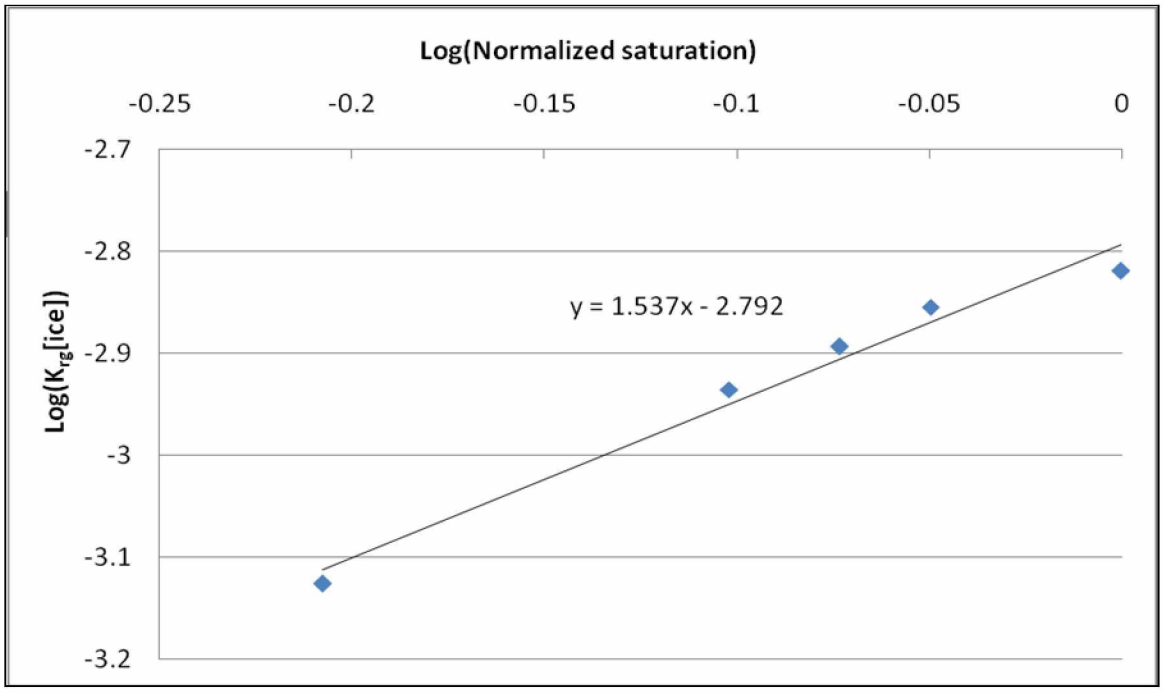

Figure D6: Relative Gas Permeability versus Normalized Saturation for Umiat Core 53

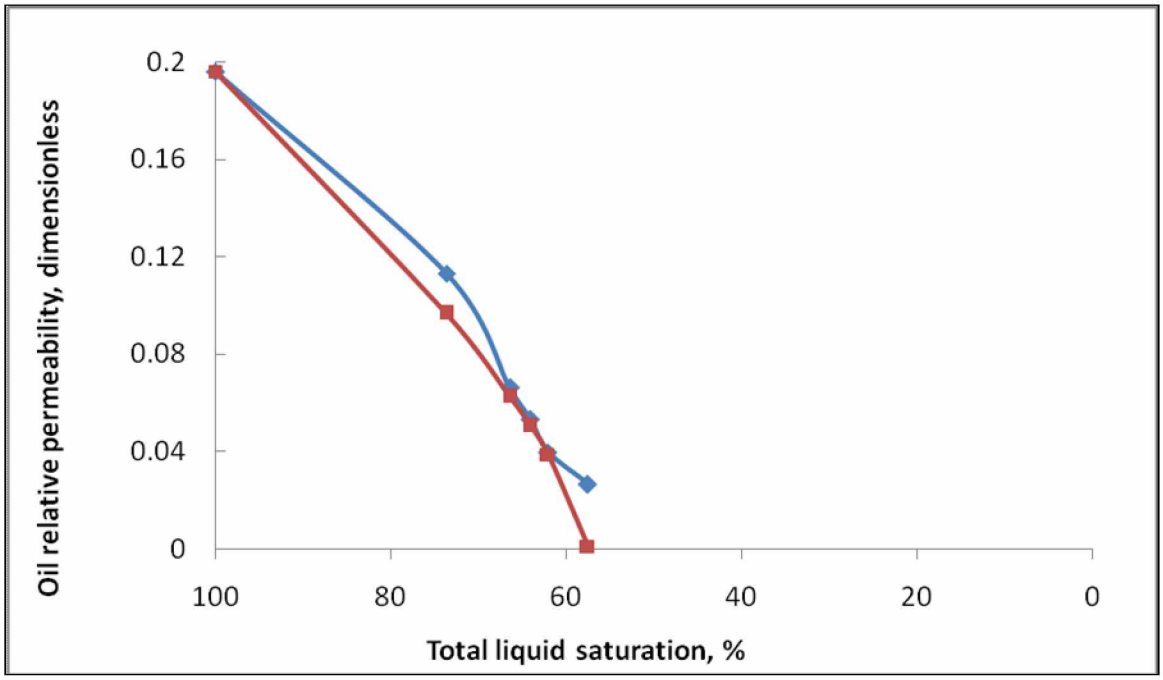

Figure D7: Experimentally-Obtained Oil Relative Permeability Data (blue) and its Analytical Representation (red) for Umiat Core 53

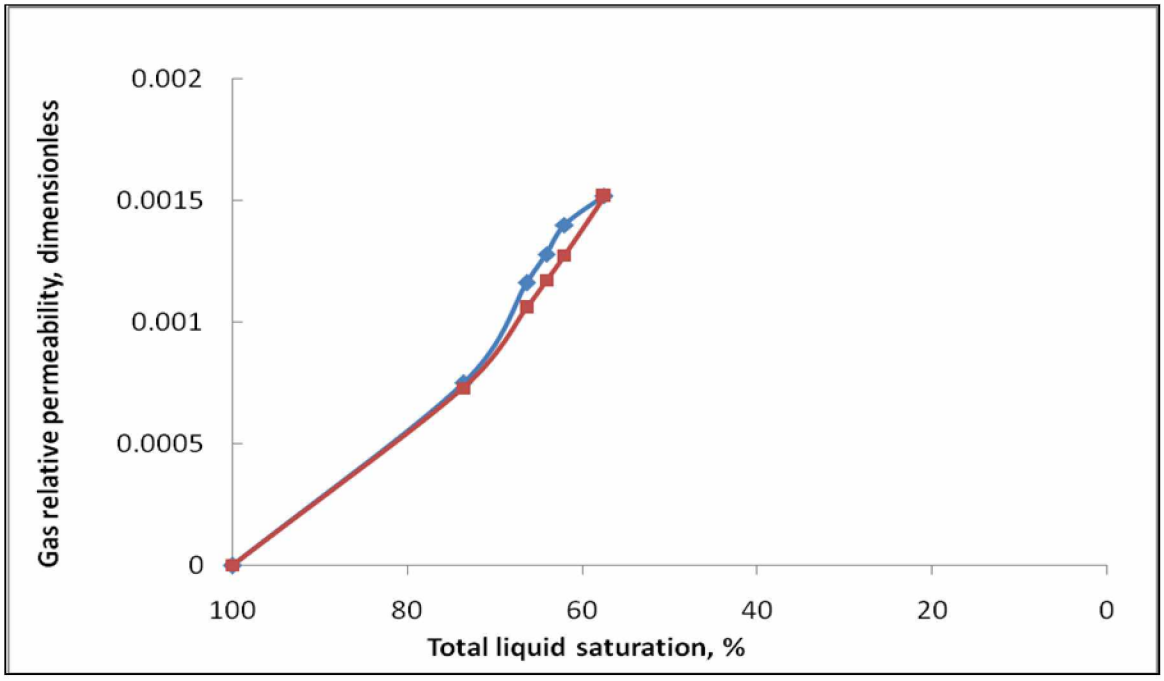

Figure D8: Experimentally-Obtained Gas Relative Permeability Data (blue) and its Analytical Representation (red) for Umiat Core 53

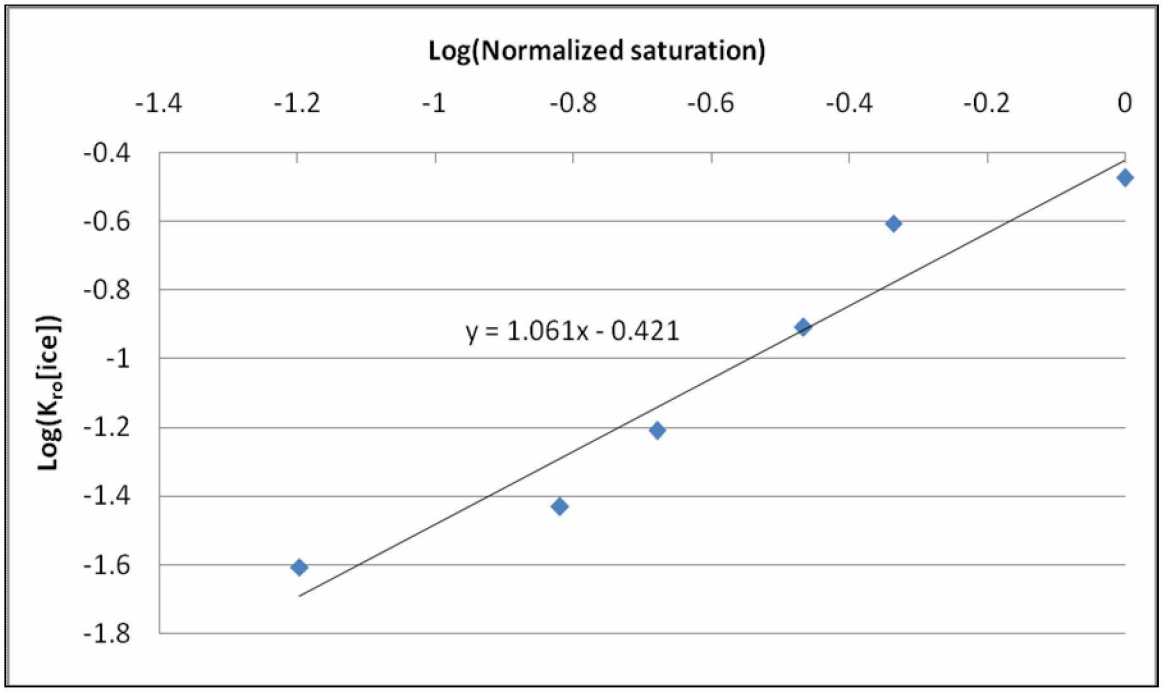

Figure D9: Relative Oil Permeability versus Normalized Saturation for Umiat Core 39

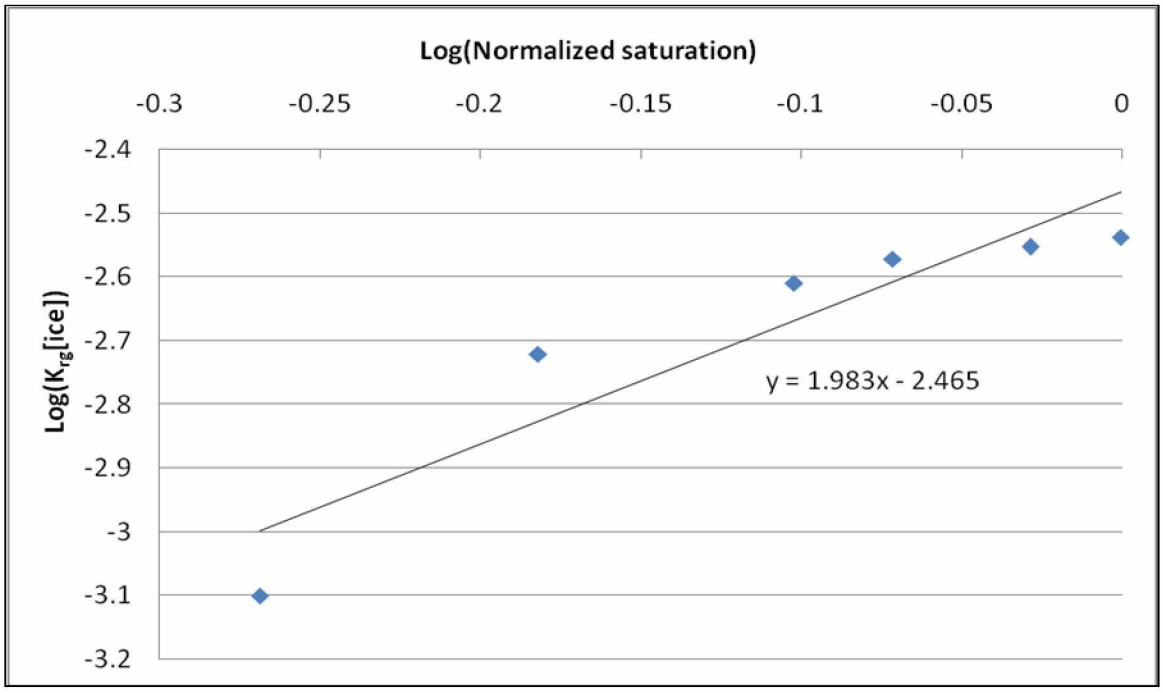

Figure D10: Relative Gas Permeability versus Normalized Saturation for Umiat Core 39

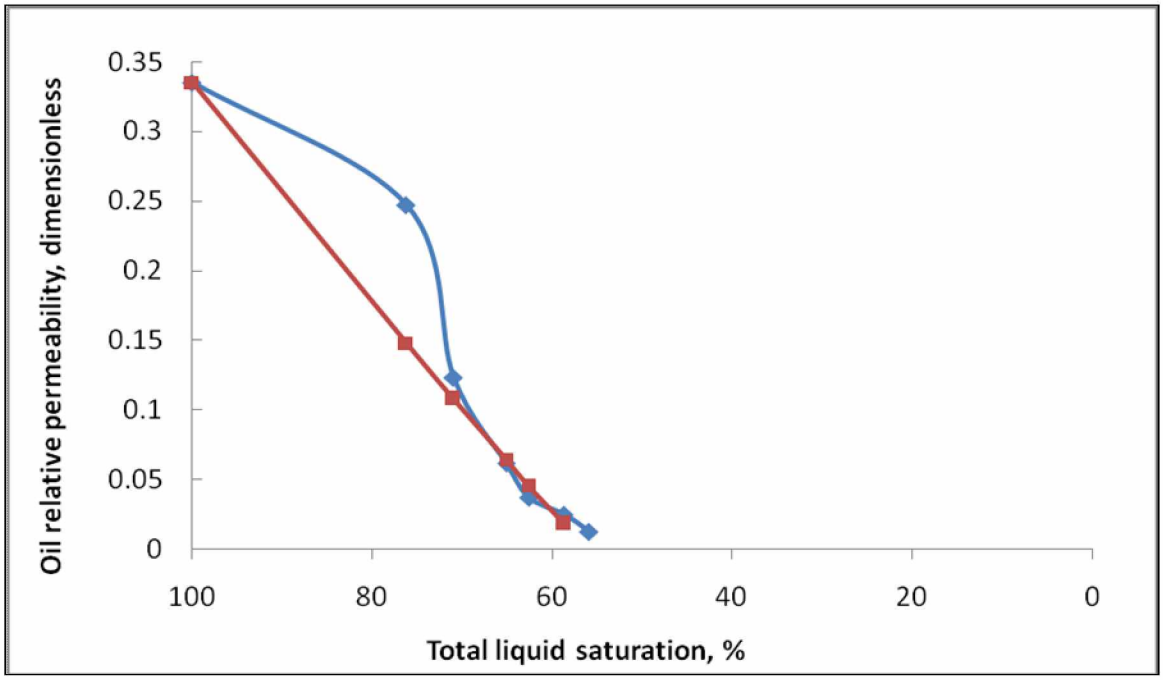

Figure D11: Experimentally-Obtained Oil Relative Permeability Data (blue) and its Analytical Representation (red) for Umiat Core 39

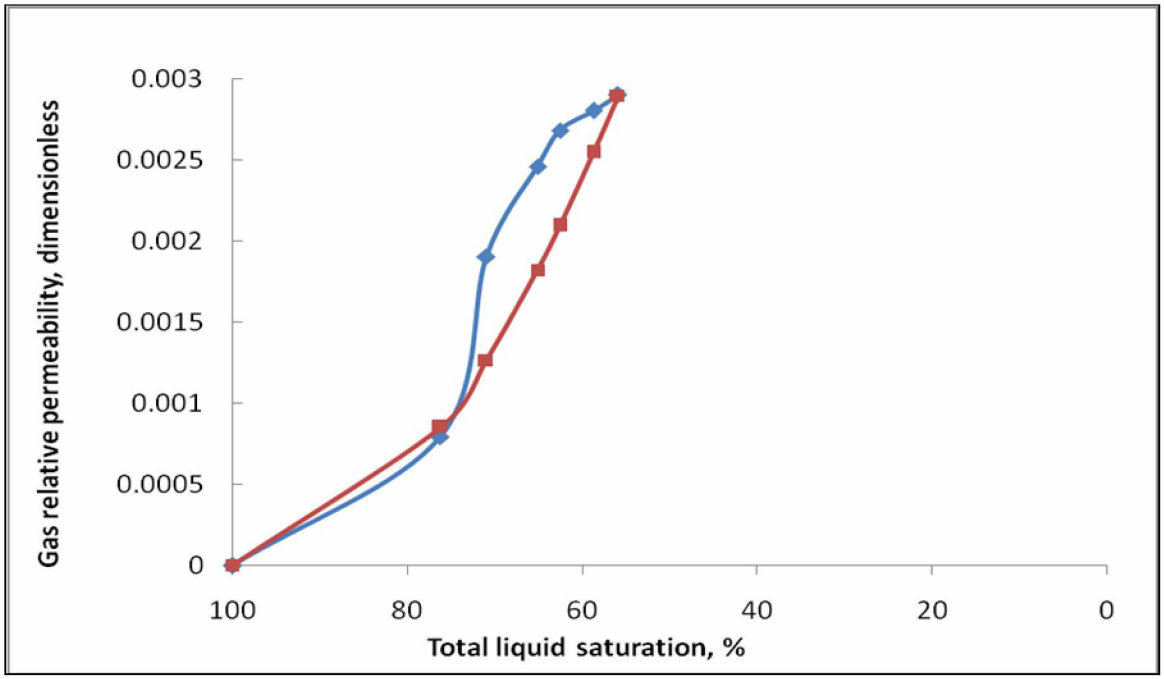

Figure D12: Experimentally-Obtained Gas Relative Permeability Data (blue) and its Analytical Representation (red) for Umiat Core 39

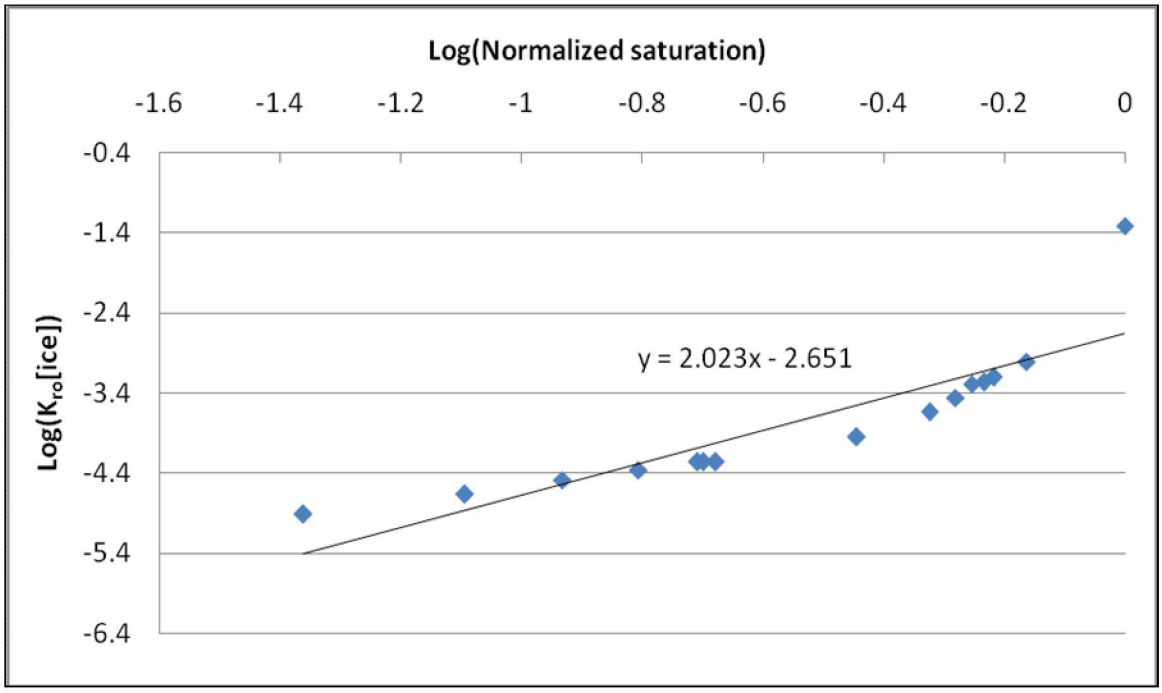

Figure D13: Relative Oil Permeability versus Normalized Saturation for Umiat Core 47

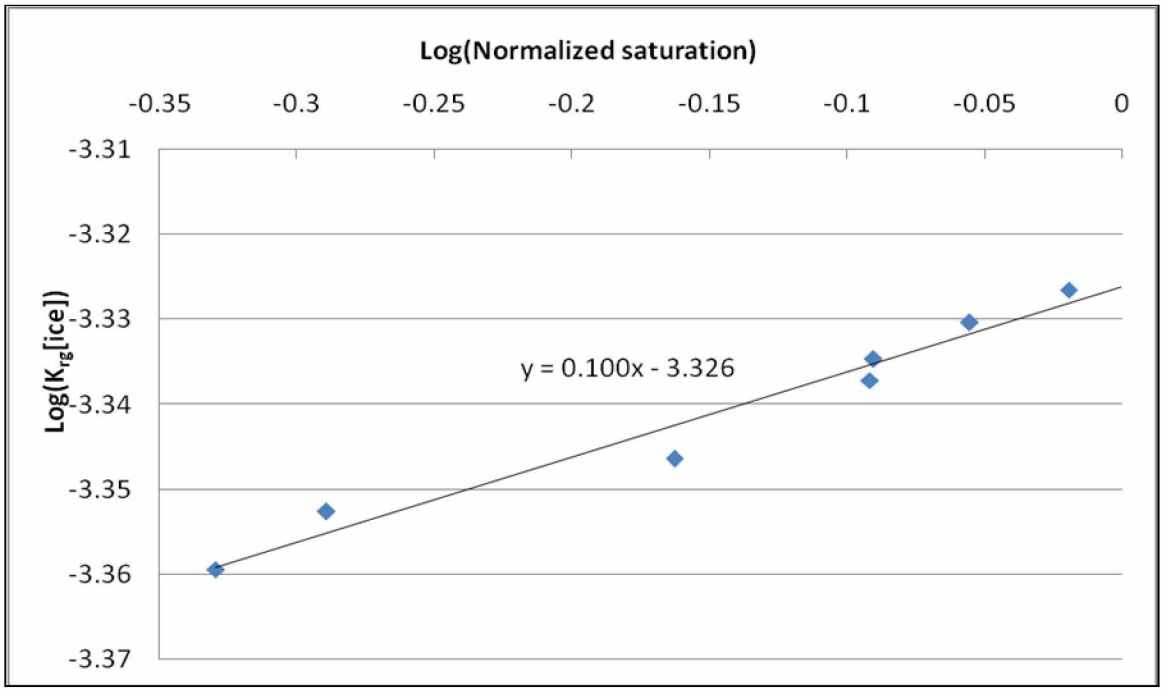

Figure D14: Relative Gas Permeability versus Normalized Saturation for Umiat Core 47

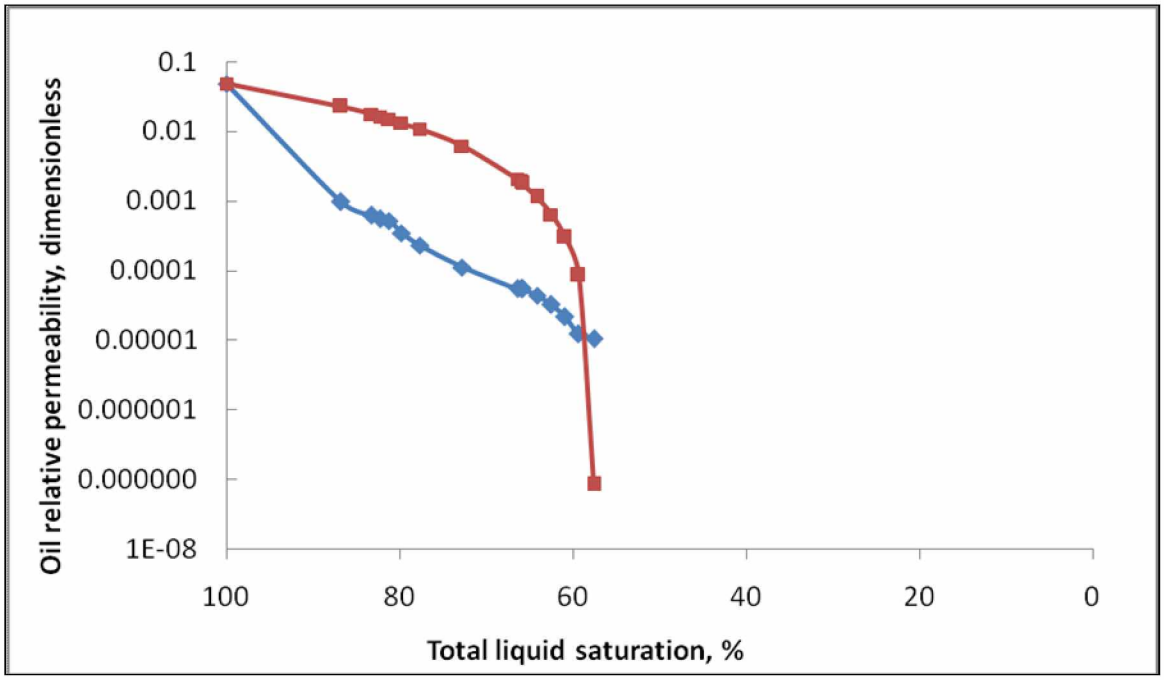

Figure D15: Experimentally-Obtained Oil Relative Permeability Data (blue) and its Analytical Representation (red) for Umiat Core 47

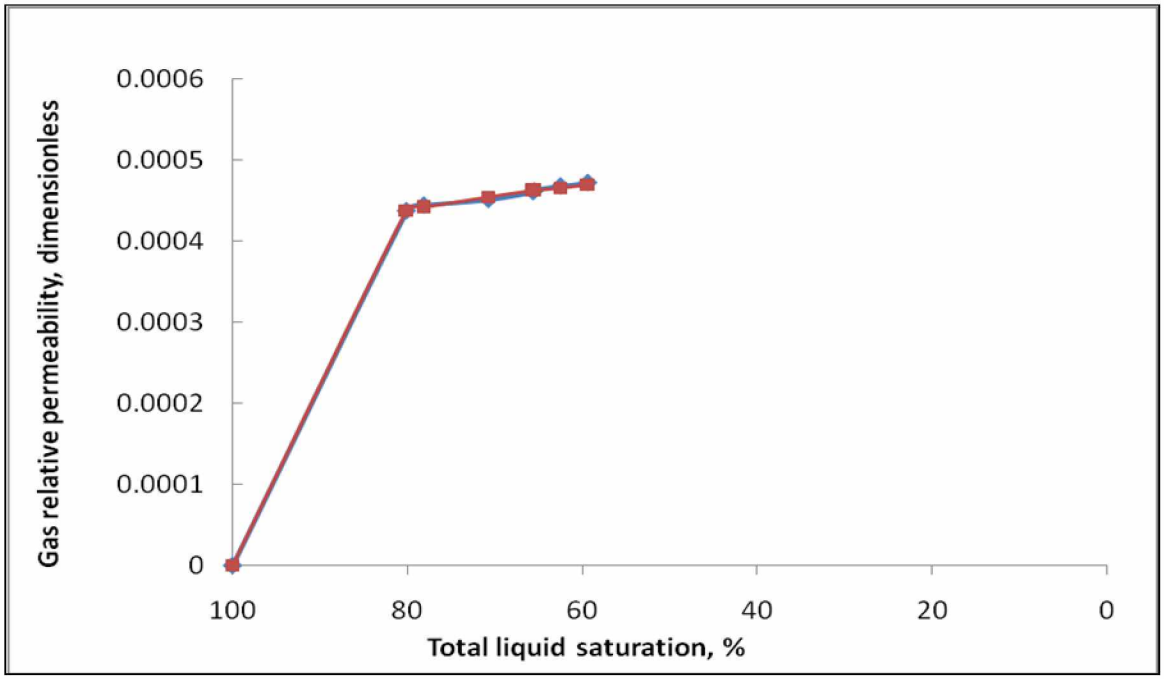

Figure D16: Experimentally-Obtained Gas Relative Permeability Data (blue) and its Analytical Representation (red) for Umiat Core 47

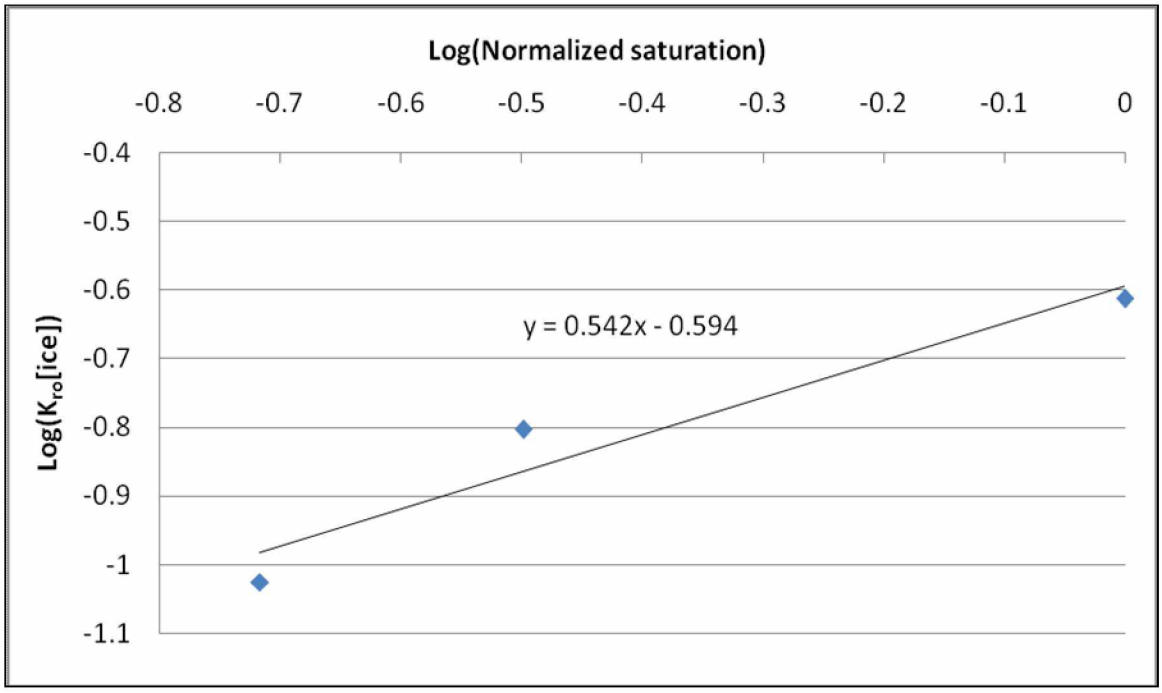

Figure D17: Relative Oil Permeability versus Normalized Saturation for Umiat Core 60

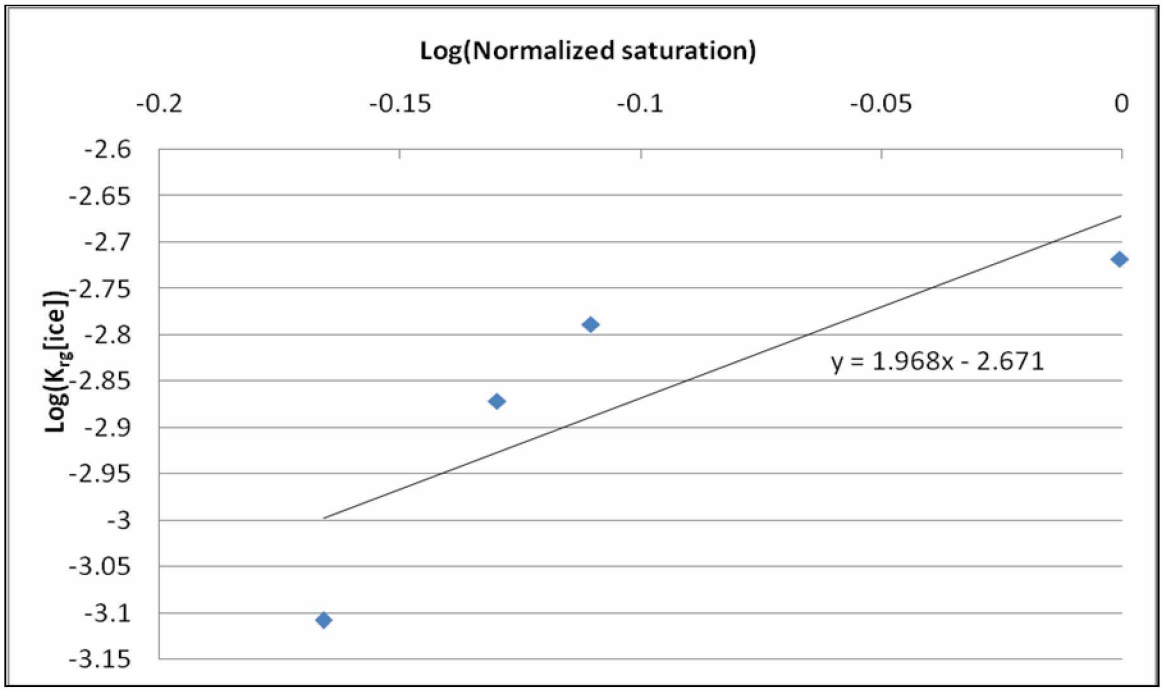

Figure D18: Relative Gas Permeability versus Normalized Saturation for Umiat Core 60

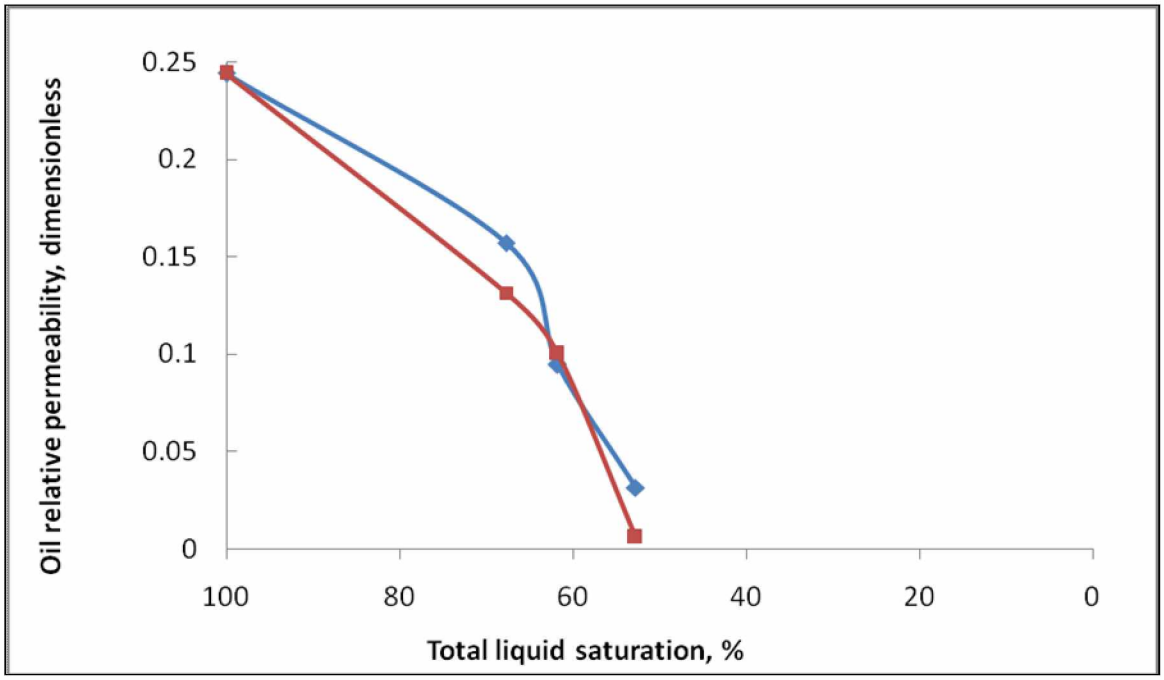

Figure D19: Experimentally-Obtained Oil Relative Permeability Data (blue) and its Analytical Representation (red) for Umiat Core 60

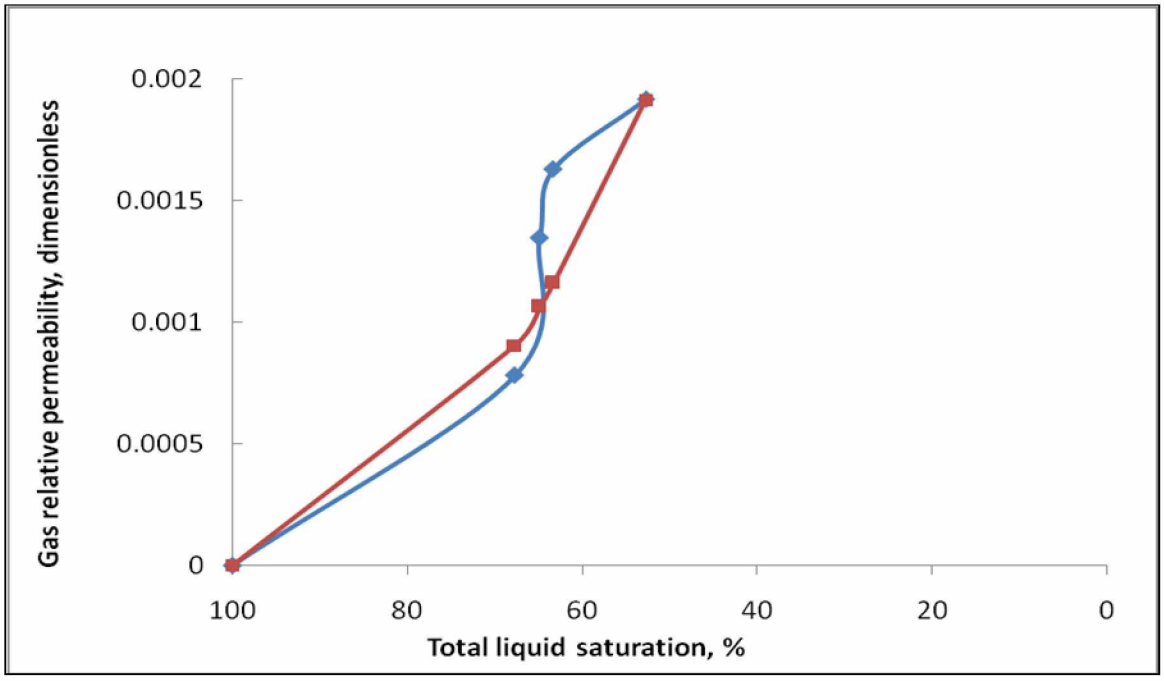

Figure D20: Experimentally-Obtained Gas Relative Permeability Data (blue) and its Analytical Representation (red) for Umiat Core 60